



Review

Integer and Fractional-Order Sliding Mode Control Schemes in Wind Energy Conversion Systems: Comprehensive Review, Comparison, and Technical Insight

Irfan Sami ¹, Shafaat Ullah ^{2,3}, Laiq Khan ⁴, Ahmed Al-Durra ⁵ and Jong-Suk Ro ^{1,6*}

- ¹ School of Electrical and Electronics Engineering, Chung-Ang University, Dongjak-gu, Seoul 06974, Korea
 - ² Department of Electrical and Computer Engineering, COMSATS University Islamabad, Abbottabad Campus, Abbottabad 22060, Pakistan
 - ³ Department of Electrical Engineering, University of Engineering and Technology Peshawar, Bannu Campus, Bannu 28100, Pakistan
 - ⁴ Department of Electrical and Computer Engineering, COMSTAS University Islamabad, Islamabad 45550, Pakistan
 - ⁵ Advanced Power and Energy Center, EECS Department, Khalifa University, Abu Dhabi P.O. Box 127788, United Arab Emirates
 - ⁶ Department of Intelligent Energy and Industry, Chung-Ang University, Dongjak-gu, Seoul 06974, Korea
- * Correspondence: jongsukro@gmail.com; Tel.: +82-2-820-5557

Abstract: The technological development in wind energy conversion systems (WECSs) places emphasis on the injection of wind power into the grid in a smoother and robust way. Sliding mode control (SMC) has proven to be a popular solution for the grid-connected WECS due to its robust nature. This paper reviews the enhancement trends in the integer-order SMC (IOSMC) and fractional-order SMC (FOSMC) schemes reported in reputed journals over the last two decades. This work starts with a mathematical description of the wind turbine, generators, grid, and SMC and its variants available in literature. A comprehensive literature review is tabulated that includes the proposed errors, sliding surfaces, typologies, and major outcomes. Moreover, a comparative analysis of the integer-order and fractional-order SMC and its variants is also presented in this paper. This paper will provide insight for the researcher working in the WECS and will serve them in the selection and exploration of the most appropriate control schemes for quality wind power extraction. The concise mathematical proofs of the IOSMC, FOSMC and their variants will also serve the researchers in selecting the relevant sliding surfaces control laws for their research tasks. This paper also provides a comparative analysis of IOSMC, FOSMC, and fuzzy-FOSMC in terms of chattering reduction, robustness, and computational complexities using mathematical theories, simulation carried out in Matlab/Simulink, and a processor in the loop (PIL)-based experimental environment.

Keywords: sliding mode control; wind energy; review; super-twisting; fractional-order control schemes



Citation: Sami, I.; Ullah, S.; Khan, L.; Al-Durra, A.; Ro, J.-S. Integer and Fractional Order Sliding Mode Control Schemes in Wind Energy Conversion Systems: Comprehensive Review, Comparison, and Technical Insight. *Fractal Fract.* **2022**, *6*, 447. <https://doi.org/10.3390/fractalfract6080447>

Academic Editor: David Kubanek

Received: 13 June 2022

Accepted: 12 August 2022

Published: 17 August 2022

Publisher's Note: MDPI stays neutral with regard to jurisdictional claims in published maps and institutional affiliations.



Copyright: © 2022 by the authors. Licensee MDPI, Basel, Switzerland. This article is an open access article distributed under the terms and conditions of the Creative Commons Attribution (CC BY) license (<https://creativecommons.org/licenses/by/4.0/>).

1. Introduction

The trend in the consumption of fossil fuels for power generation is declining with the advent of renewable-energy-generating systems. This is evident from the declining trend of fossil fuels from 86% in 1973 to 81% in 2016 [1]. Wind energy is sharing a substantial part in the overall renewable energy generation all over the world. The wind energy is utilized through a wind energy conversion system (WECS) that consists of three major components, including a wind turbine, gear, and electrical generator. The WECS converts the wind energy into electricity, and then power electronics come into play to integrate the electric power to the grid [2]. There is rapid growth in the wind turbine rotor size; thus, the WECS power-generating capacity is also progressing. The increasing trend of the rated energy output of wind turbines with the increase in rotor diameter with time is elaborated in [3]. The WECS is becoming smaller in size and less costly due to the

rapid development in the power converters [4–7]. The WECS is complex and depends on external meteorological conditions, such as wind speed, and internal nonlinear dynamics, parametric uncertainties, and unknown disturbances. Thus, a control system is essential in order to transfer wind energy to the grid [8]. Various types of mechanical and electrical control techniques employed in WECS are shown in Figure 1. The WECS works in four regions of operation. In the first region (R_1), the generator's wind speed is low enough to produce power. The second region (R_2) is bounded by wind speeds V_{in} and V_{rated} , where V_{rated} provides the rated power P_{rated} . The third region (R_3) is bounded by the wind speeds V_{rated} and V_{out} , and the rated power is extracted from the wind speeds in this region. The turbine is stopped for the wind speeds exceeding V_{out} and is called the fourth region (R_4). The four operating regions of WECS are illustrated in Figure 2 [9–11]. The maximum output power extraction from region R_2 is carried out through algorithms known as maximum power point tracking (MPPT) algorithms. These MPPT algorithms are only employed for variable speed wind turbines (VSWT) to extract maximum power from the wind with full or partial-order power electronics converter [8,12–14]. The maximization of extracted power is preserved by the VSWTs using the optimum tip speed ratio (OTSR). Extensive research has been carried out to formulate control techniques and maximum power point tracking (MPPT) in WECS.

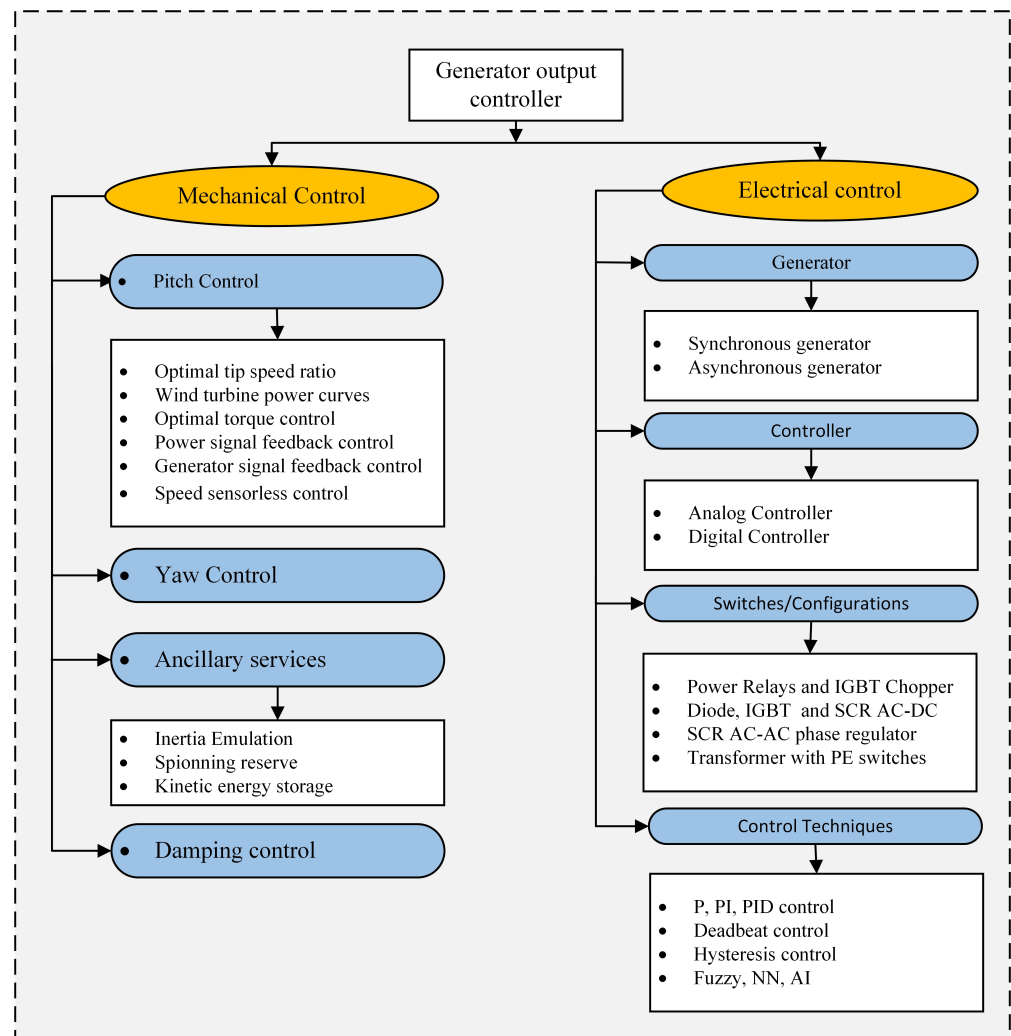


Figure 1. Electrical and mechanical control schemes used in WECS.

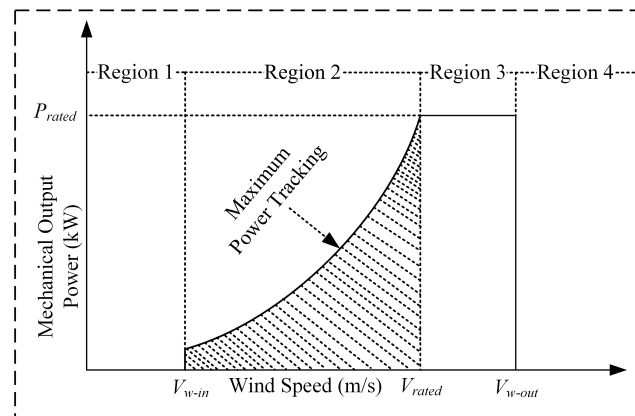


Figure 2. The four operating regions of WECS. Reprinted with permission from Ref. [8]. Copyright 2016 Elsevier.

Various typologies and configurations are developed utilizing the MPPT techniques to improve power conversion technologies and employing different generator types [15]. For instance, DC generators, synchronous generators (SGs), and induction generators (IGs) are the three major types of generators used in WECS that operate using wound rotors [16,17]. Other types of generators reported in the literature employed in WECS are wound rotor induction generators (WRIGs) [18], squirrel cage induction generators (SCIG) [19–21], DC generators [17], variable reluctance generators (VRGs) [22], switched reluctance generator (SRGs) [23], and permanent magnet synchronous generators (PMSGs) [24,25]. Two major categories of WRIGs are DFIGs and dynamic slip-controlled generators [26]. These generators are compared regarding their advantages and disadvantages in Figure 3. Electronic devices are the backbone for the control and flexible operation of grid-connected WECS in transient and steady-state operation [27,28]. Before introducing AC-DC-AC converters in the 2000s, soft starters were initially used in the 1980s for the grid connection of SCIGs [29]. In contrast, chopper circuits combined with diode bridges were utilized to control WRIGs using rotor resistance [30]. The back-to-back converters have the advantages of transferring a high and smooth electricity quality after extracting maximum power from wind [31,32]. In grid-connected operation, the DFIGs use partially scaled [33,34] back-to-back converters rated at 30% of the generator rating [35] and have the advantage of speed control using AC excitation [36]. The stator of DFIG is directly connected to the grid, whereas the rotor is connected to the grid using back-to-back converters. The partially scaled converters control the rotor speed and perform active and reactive power decoupled control with reactive power compensation [37]. The disadvantage of DFIG-based WECS is the protection problems under grid fault perturbations and the use of slip rings.

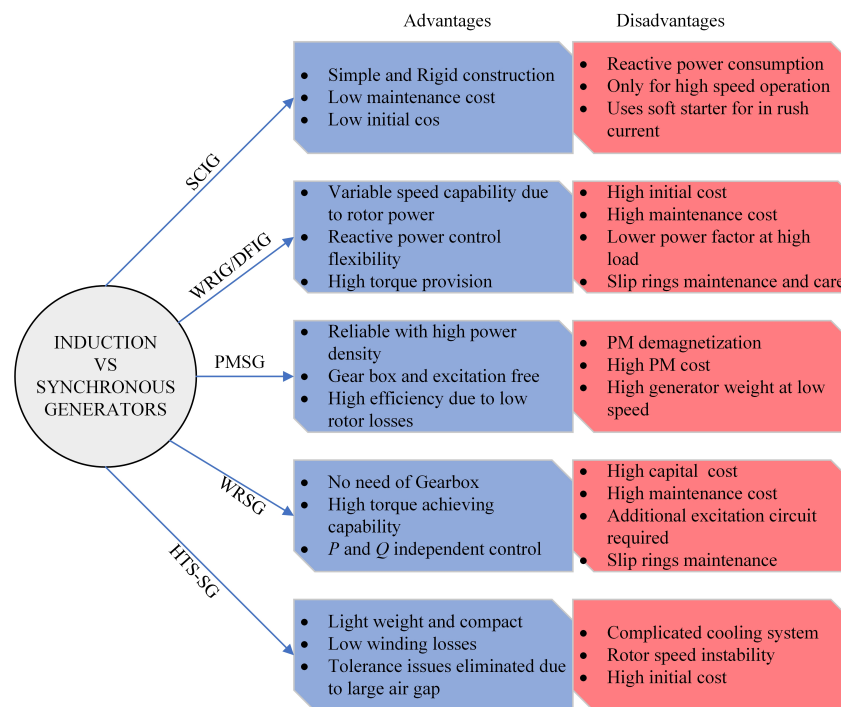


Figure 3. Induction vs. synchronous generators.

In contrast, the PMSG-WECS employs full-scale power converters and thus provides a complete decoupling from grid faults, which is much better [38,39]. Several typologies of grid-connected direct-driven PMSG-WECS are presented in [29,40–43], which include diode rectifiers [44], two-level back-to-back converters [45], Z-sources, multilevel converters, matrix converters, and nine switch ac-ac converter typologies. Multipole wound rotor synchronous generators are commonly used in low or variable speed areas due to their simple pitch control, low cost, high mechanical stress absorption, and torque ripple compensation capability [33]. SCIGs also provide reliable and straightforward applications in grid-connected WECS due to their ability to limit the output power; thus, they are used in high-power security and maintenance-requiring situations [46]. The SCIG generators are employed for offshore wind farms where the electricity is transferred using HVDC transmission lines. The connection of various SCIGs is established through a thyristor soft starter that reduces the mechanical stress and limits the inrush currents. The DC generators are rarely used generators in WECS due to their high maintenance and cost. The DC generators are usually employed with the small turbines together with battery banks [47,48].

2. Motivation of This Study

The MPPT techniques presented in the literature used to transfer the power of wind energy to the grid side are reported in [8]. The various MPPT control techniques prominent in the literature are OTSR control [49–53], WT power curves-based control [54], power signal feedback control (PSF) [8,49,55], generator signal feedback control [54], optimal torque algorithm (OTA) [50,53,56], speed sensorless control [54], and soft computing, e.g., AI and FLC-based MPPT control schemes [57–63]. The MPPT techniques are categorized into two groups based on power maximization, which are: (1) indirect power control (IPC) and (2) direct power control (DPC). In DPC, the electrical power (P_e) is maximized, whereas, in IPC, the mechanical power (P_m) is maximized. The relation between (P_m) and (P_e) depicts that the maximum power cannot be guaranteed even if the optimal (P_m) is achieved. The IPC algorithm covers various types of MPPT algorithms, which are OTSR, PSF [64], and OTA [8,64,65]. The OTSR is the turbine-rotating-speed-to-wind-speed ratio, as the VSWTs are subjected to varying rotation proportional to the instantaneous

change in wind speed [66]. The OTSR-based MPPT method uses an anemometer and is inefficient due to the wind speed variation along the blade length. The PSF and OTA-based methods operate without an anemometer, but these methods are still inefficient due to the requirement of wind-turbine-specific parameters. The conventional DPC methods are optimum-relation-based MPPT (ORM) paradigms, incremental conductance (INC), and hill-climbing-search-based MPPT (HSM) techniques.

Apart from conventional methods mentioned earlier, a wide range of MPPT techniques have been proposed in the literature; for instance: proportional integral (PI) [67], backstepping controller- [68], fuzzy logic [69], neural network [70], fuzzy-neural network [71], two fuzzy [72], input-output feedback linearization [73], model predictive control [74], adaptive support vector machine combined with firefly algorithm [75], and an adaptive dynamic programming-based MPPT technique [76]. The conventional control techniques for WECS control have traditionally been proportional-integral-derivative (PID) controllers [67]. However, due to their sensitivity to variation in operating points, the nonlinear behavior of WTs, disturbances, and the possibility of faulty scenarios, the conventional control techniques cannot be considered as reliable control techniques. Researchers have proposed various innovative advanced control strategies to improve the WECS control system performance in this regard. Robust control techniques are widely used in the literature to mitigate wind effects and improve power quality, with H_2 and H_∞ [77] methods being the most commonly used [78,79]. The MPC also provided an enhanced performance for WECS due to its reduced switching frequency, inherent optimization features, and minimized error. The MPC makes the system mathematically complex and sensitive to parameters uncertainties [80]. Soft-computing-based methods, including artificial neural networks, fuzzy logic control (FLC), and meta-heuristic algorithms-based controllers, are advanced control techniques that provide a quick and efficient response in order to handle the uncertainties in WECS [81,82]. Similarly, the authors of [83,84] created fuzzy-based FTC approaches for WT power control.

WECS is a highly nonlinear system prone to several uncertainties; thus, robust nonlinear control is preferable for smooth operation. Sliding mode control (SMC) is a robust and simple control scheme with a dynamic behavior [85] that was developed in 1977 by Utkin for parametric variations and internal and external unknown disturbance in variable structure systems [86]. SMC applications for WECS start with first-order SMC paradigms, as reported in the literature by [87–91]. First-order SMC schemes are subjected to inherent undesirable phenomena with finite amplitude and frequency called chattering [92]. Conventional SMC is discontinuous, which leads to chattering, singularity, and sensitivity to mismatched uncertainties and disturbances, which restrict its practical application because unmatched uncertainties have an impact on a wide range of practical systems. Furthermore, while asymptotic stability is guaranteed by conventional SMC, there is no assurance that it will occur in finite time, particularly in the presence of unmatched disturbances. When a system is in its sliding mode, it behaves like a predetermined reduced-order system and stops responding to changes in parameters. The researchers presented many methods to mitigate the chattering phenomena and improve the dynamic behavior, resulting in various variants of SMC. Initially, a boundary layer was used by [87] to remove the chattering problem. The many techniques presented are: appropriate finite gains [93], high-order SMC (HOSMC) [94,95], second-order SMC (SOSMC) [96–99], fuzzy SMC [100], extended state observer-based [101], fractional-order SMC (FOSMC) [102,103], fractional-order terminal SMC (FOTSMC) [104], super twisting FOTSMC (ST-FOTSMC) [105], artificial intelligence integrated FOSMC [106], and composite FOSMC [2]. The SMC variants covered in the literature proposed for WECS are given in Figure 4. Various recent control techniques presented in the literature are compared in Table 1 for various attributes, where \checkmark denotes the occurrence of the attribute and \times denotes the absence of the attribute.

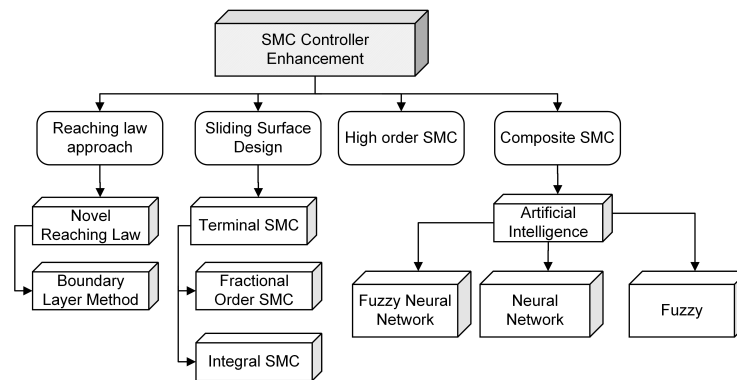


Figure 4. Enhancement techniques in sliding mode control. Reprinted with permission from Ref. [2]. Copyright 2021 Elsevier.

This paper presents comprehensive insight into the WECS, employing various typologies and SMC strategies to transfer wind power to the electric grid. This paper starts with an introduction of the MPPT techniques for WECS. The comprehensive utilization of various types of generators used in WECS is then discussed and tabularized for comparative analysis. The mathematical modeling of the wind turbine, doubly fed induction generator (DFIG), and permanent magnet synchronous generator (PMSG) is discussed. The general introduction of SMC is discussed and is categorized into (1) integer-order SMC (IOSMC) and (2) FOSMC based on sliding surface construction. In IOSMC, first-order SMC is discussed for WECS, and mathematical proof of the control laws for both the grid side converter (GSC) and rotor side converter (RSC) are presented. The various variants of first-order SMC discussed and mathematically presented are HOSMC, ISMC, BSMC, and fuzzy-SMC. Mathematical study and control law derivation for the three primary variants of FOSMC presented in the literature, including FOTSMC, ST-FOTMSC, and composite FOSMC, are presented.

Table 1. Comparative analysis of various controllers for DFIG-WECS.

Ref.	Technique Employed	SC	PU	ED	UBD	CE	R	DS	FTC
[107]	PI	✗	✗	✗	✗	✗	✗	✗	✗
[108]	Backstepping	✓	✓	✗	✗	✓	✓	✗	✗
[109]	SMC	✓	✗	✗	✗	✗	✓	✓	✗
[110]	SMC	✓	✓	✓	✗	✓	✓	✓	✗
[111]	SMC with ERL	✓	✓	✓	✗	✓	✓	✓	✗
[112]	Adaptive backstepping	✓	✓	✓	✓	✓	✓	✓	✗
[101]	ADR control using ESO	✓	✓	✓	✓	✓	✓	✓	✗
[113]	Adaptive neuro-fuzzy	✓	✓	✓	✓	✓	✓	✓	✗
[114]	SMC	✓	✓	✓	✗	✓	✓	✓	✓
[115]	Coordinated HOSMC	✓	✓	✓	✗	✓	✓	✓	✗
[116]	HOSMC	✓	✓	✓	✗	✓	✓	✓	✓
[117]	HOSMC	✓	✓	✓	✗	✓	✓	✓	✓
[118]	Adaptive STSMC	✗	✓	✓	✗	✓	✓	✓	✓

System complexity (SC), Parametric uncertainty (PU), External disturbances (ED), Upper bound (UB), Chattering elimination (CE), Robustness (R), Dynamical stability (DS), Finite time convergence (FTC).

3. Modeling of WECS and Generators for Closed Loop Control

3.1. Wind Turbine Model

The kinetic energy in wind runs the turbine in order to generate the mechanical power used to drive the generator. This mechanical power is expressed by the following equation as a function of wind speed and wind turbine geometry [105]:

$$P_\omega = \frac{1}{2} \rho \pi R^2 C_p(\lambda, \beta) v^3 \quad (1)$$

where

$$\lambda = \frac{(\Omega_t R)}{v} \quad (2)$$

C_p and λ correlate by the expression given as follows:

$$C_p = c_1 \left(\frac{c_2}{\lambda - 1} \right) e^{-\frac{c_3}{\lambda}} \quad (3)$$

A maximum value of $C_p = C_{p-max}$ is achieved when the value of λ equals the optimum value of λ , i.e., $\lambda = \lambda_{opt}$. The wind turbine torque is given as follows:

$$T_r = \frac{T_t}{G} \Omega_t = \frac{\Omega_r}{G} \quad (4)$$

Putting (4) into (1) and (2), the Ω_{r-ref} and $P_{grid-ref}$ is given as:

$$\left. \begin{aligned} \Omega_{r-ref} &= \frac{\lambda_{opt} G}{R} v \\ P_{grid-ref} &= \frac{1}{2} \eta \rho \pi^2 C_{p-max} v^3 \end{aligned} \right\} \quad (5)$$

where η is the wind turbine efficiency.

3.2. Doubly Fed Induction Generator Model

The DFIG has strongly decoupled dynamics; thus, the representation of DFIG in a three-phase system is quite a difficult task. In this section, the DFIG dynamic mode in a dq-reference frame is presented and is given below [105].

$$\left. \begin{aligned} V_{ds} &= R_s I_{ds} + \frac{d}{dt} \varphi_{ds} - \omega_s \varphi_{qs} \\ V_{qs} &= R_s I_{qs} + \frac{d}{dt} \varphi_{qs} + \omega_s \varphi_{ds} \\ V_{dr} &= R_r I_{dr} + \frac{d}{dt} \varphi_{dr} - (\omega_s - \omega_r) \varphi_{qs} \\ V_{qr} &= R_r I_{qr} + \frac{d}{dt} \varphi_{qr} - (\omega_s - \omega_r) \varphi_{ds} \end{aligned} \right\} \quad (6)$$

where

$$\left. \begin{aligned} \varphi_{ds} &= L_g I_{ds} + M I_{dr} \\ \varphi_{qs} &= L_s I_{qs} + M I_{qr} \\ \varphi_{dr} &= L_s I_{dr} + M I_{ds} \\ \varphi_{qr} &= L_s I_{qr} + M I_{qs} \end{aligned} \right\} \quad (7)$$

$$\left. \begin{aligned} T_{em} &= \frac{3}{2} P \frac{M V_s}{\omega_s L_s} (\varphi_{qs} I_{dr} - \varphi_{ds} I_{qr}) \\ J \dot{\Omega}_r &= T_{em} - T_r - f_r \Omega_r \end{aligned} \right\} \quad (8)$$

Here, $b = 1/J$, $a = f/J$, and $f = \frac{T_r}{J}$. Aligning the reference frame to the d-axis of the stator flux, we have $\varphi_{ds} = \varphi_s$ and $\varphi_{qs} = 0$, and, therefore, T_{em} in (8) can be simplified as:

$$T_{em} = -p \frac{MV_s}{\omega_s L_s} \varphi_s I_{qr} \quad (9)$$

The active power, reactive power, and rotor voltages may be achieved by assuming a constant stator flux, neglecting the per phase stator resistance, taking $V_{ds} = 0$ and $V_{qr} = V_s = V_{dr} = \omega_s \varphi_s$, and putting (9) into (6) and (7), and are given as follows:

$$\left. \begin{aligned} V_{dr} &= R_r I_{dr} + \sigma L_r \frac{d}{dt} I_{dr} - s \sigma L_r \omega_g I_{dr} \\ V_{qr} &= R_r I_{qr} + \sigma L_r \frac{d}{dt} I_{qr} - \sigma s \omega_s I_{dr} + s \frac{MV_s}{L_s} \end{aligned} \right\} \quad (10)$$

Here, $\sigma = 1 - \frac{M}{L_r L_s}$ and $s = \frac{\omega_s - \omega_r}{\omega_s}$.

$$\left. \begin{aligned} P_s &= -\frac{MV_s}{L_s} I_{qr} \\ Q_s &= \frac{V_s^2}{\omega_g L_s} I_{qr} - \frac{MV_s}{L_g} I_{dr} \end{aligned} \right\} \quad (11)$$

The $d - q$ representation of the rotor current is given as:

$$\left. \begin{aligned} \frac{d}{dt} I_{dr} &= \frac{1}{\sigma L_r} \left(V_{dr} - R_r I_{dr} + s \sigma L_r \omega_s I_{qr} - \frac{M}{L_s} \frac{d}{dt} \varphi_{ds} \right) \\ \frac{d}{dt} I_{qr} &= \frac{1}{\sigma L_r} \left(V_{qr} - R_r I_{qr} - s \sigma L_r \omega_g I_{dr} - s \omega_s \frac{M}{L_s} \frac{d}{dt} \varphi_{ds} \right) \end{aligned} \right\} \quad (12)$$

3.3. Grid Model

The dynamic model of the grid side is given using the following dynamic equations [36]:

$$\left. \begin{aligned} V_{gd} &= e_d - R_g I_{gd} - L_g \frac{d}{dt} I_{gd} + \omega_g L_g i_{gq} \\ V_{gq} &= e_q - R_g I_{gq} - L_g \frac{d}{dt} I_{gq} - \omega_g L_g i_{gd} \end{aligned} \right\} \quad (13)$$

It can be re-arranged as follows:

$$\left. \begin{aligned} \frac{d}{dt} I_{gd} &= \frac{1}{L_g} \left(e_d - R_g I_{gd} - V_{gd} + \omega_g L_g I_{gq} \right) \\ \frac{d}{dt} I_{gq} &= \frac{1}{L_g} \left(e_q - R_g I_{gq} - V_{gq} - \omega_g L_g I_{gd} \right) \end{aligned} \right\} \quad (14)$$

where the active and reactive power are given as follows:

$$\left. \begin{aligned} P_g &= \frac{3}{2} \left(V_{gd} I_{gd} + V_{gq} I_{gq} \right) = \frac{3}{2} \left(V_{gd} I_{gd} \right) \\ Q_g &= \frac{3}{2} \left(V_{gq} I_{gd} + V_{gd} I_{gq} \right) = \frac{3}{2} \left(V_{gd} I_{gq} \right) \end{aligned} \right\} \quad (15)$$

The current control strategy is derived such that the current x follows the reference current x_{ref} . The x_{ref} is given as follows:

$$x_{ref} = \left[I_{dr-ref} \quad I_{qr-ref} \right]^T \quad (16)$$

The reference q – axis current is generated using (9), given as:

$$I_{qr-ref} = \frac{\omega_s L_s}{PMV_s} T_{em-ref} \quad (17)$$

The d-axis reference current is derived by substituting $Q_{s-ref} = 0$ into reference reactive power $Q_{s-ref} = \frac{V_s^2}{\omega_s L_s} - \frac{MV_s}{\omega_s L_s} I_{dr}$, and is given as:

$$I_{dr-ref} = \frac{V_s}{\omega_s M} \quad (18)$$

The gusty and stochastic wind nature results in a dynamical and variable flow of wind through the DFIG rotor. Thus, an efficient control strategy should be employed to accomplish the non-trivial task of DC link voltage constant regulation. Thus, a vector control strategy was employed here to achieve this task. The vector control strategy aligns the reference frame orientation with stator or grid voltage. Hence, the active and reactive power after $V_s = V_D$ and $V_Q = 0$ are given as:

$$\left. \begin{aligned} P_g &= \frac{3}{2} (V_{gd} I_d + V_{gq} I_{gq}) = \frac{3}{2} (V_{gd} I_d) \\ Q_g &= \frac{3}{2} (V_{gq} I_{gd} + V_d I_{gq}) = \frac{3}{2} (V_{gd} I_{gq}) \end{aligned} \right\} \quad (19)$$

I_d and I_q directly affect the electric power flow between the grid converter and grid as depicted in (19). As the DC power is equivalent to the flow of the active power between the grid side converter and grid, the dynamics can be shown as [106]:

$$I_{os} = \frac{3}{2E} V_{gd} I_{gd} \quad (20)$$

$$C \frac{dE}{dt} = I_{os} - I_{or} \quad (21)$$

Substituting (21) in (20), we obtain:

$$\left. \begin{aligned} \dot{E} &= \frac{1}{c} \left(\frac{3}{2E} V_{gd} I_{gd} - I_{or} \right) \\ \dot{E} &= g(x) I_{gd} - \frac{1}{c} I_{or} \end{aligned} \right\} \text{where } g(x) = \frac{1}{c} \frac{3}{2E} V_{gd} \quad (22)$$

Adding uncertainty term $\Delta g(x)$ to $g(x)$ in (22), the $g(x)$ is given as follows:

$$g(x) = g_0(x) + \Delta g(x); \quad g_0(x) = \frac{1}{c} \frac{3}{2E_{ref}} V_{gd} \quad (23)$$

where E_{ref} is the reference value of E . Putting $g(x)$ from (23) into (22) gives us:

$$\dot{E} = g_0(x) I_{gd} - \frac{1}{c} I_{or} + dE; \quad dE = \Delta g(x) I_{gd} \quad (24)$$

These equations will be further used to model controllers for WECS.

4. Sliding Mode Control Theory

SMC is an accurate, simple, and robust technique used to control and regulate nonlinear systems prone to external perturbations, disturbances, and parametric uncertainties. SMC is designed to operate the system on a surface known as the sliding surface in the desired manner. The proposed SMC-based control law is responsible for keeping the system in the vicinity of the sliding surface. Thus, the basic principle of SMC can be elaborated as

a switching function, and control law can converge any point in the system state space to the proposed sliding surface to gradually stabilize the system's equilibrium point on the design surface [119]. The SMC design consists of two steps: (1) designing a sliding surface and (2) designing a control law using state-space equations. The DFIG is a nonlinear and controlled system represented by the state-space equations as follows:

$$\left. \begin{aligned} \dot{x}_1 &= x_2 \\ \dot{x}_2 &= f(x, t) + g(x, t)u \end{aligned} \right\} \quad (25)$$

Here, the system state variables are shown by x_1 and x_2 , and $f(x, t)$ and $g(x, t)$ represent the nonlinear function and control gain function; the control input is shown here by u . In sliding mode theory, the ultimate goal is the design of an appropriate sliding variable $S = S(x, t) \in \mathbf{R}$ so that, during sliding mode $S = S(x, t) = 0$, a good compensation of system dynamics is achieved. The derivative of $S(x, t)$ can be expressed as follows [119].

$$\dot{S}(x, t) = \varphi(x, t) + \psi(x, t)u \quad (26)$$

where $\varphi(x, t) = \frac{\partial S}{\partial t} + \frac{\partial S}{\partial x}f(x, t)$ and $\psi(x, t) = \frac{\partial S}{\partial x}(g(x, t))$. In order to regulate the stability of systems, it is assumed that: A.1 The function $\psi(x, t) \in \mathbf{R}$ is uncertain and can be presented as:

$$\psi(x, t) = \psi_0(x, t) + \Delta\psi(x, t) \quad (27)$$

where $\psi_0(x, t)$ is a positive known function and $\Delta\psi(x, t)$ is a bounded control perturbation so that $\left| \frac{d}{dt}(\Delta\psi(x, t)) \right| < \xi$, $\left| \frac{\Delta\psi(x, t)}{\psi_0(x, t)} \right| \leq Y < 1$, ξ and Y are unknown boundaries. A.2 The function $\varphi(x, t) \in \mathbf{R}$ is presented as follows: $\varphi(x, t) = \varphi_1(x, t) + \varphi_2(x, t)$, with the following bounded conditions: $|\varphi(x, t)| \leq \phi|S|^{1/2}$, $|\varphi_1(x, t)| \leq \delta_1|S|^{1/2}$, $|\varphi_2(x, t)| \leq \delta_2$, and the finite boundaries $\phi, \delta_1, \delta_2 > 0$ [119].

Errors Definition for SMC and Its Variants

The surfaces in SMC are proposed on the basis of the error between the state variable and its reference. Speed, current, and DC link voltages are controllable state components in DFIG-based WECS. The mathematical proofs of SMC and its variants for DFIG-based WECS utilizes three types of errors for both the GSC and RSC side. These errors are: e_Ω (the error between the reference generator speed and actual generator speed), e_1 and e_2 (the error between the reference and actual dq currents), and e_E (the error between the reference and actual DC link voltage). The mathematical proofs also utilizes the derivative of the error mentioned earlier. The error and their derivatives are given as follows:

For the RSC side, the error between the reference and actual speed is denoted by e_Ω and given as:

$$e_\Omega = \Omega_r - \Omega_{r-ref} \quad (28)$$

Taking its derivative and putting the values from (8), we have:

$$\left. \begin{aligned} \dot{e}_\Omega &= \dot{\Omega}_r - \dot{\Omega}_{r-ref} \\ \dot{e}_\Omega &= \frac{T_{em}}{J} + d_3 - \dot{\Omega}_{r-ref} \end{aligned} \right\} \quad (29)$$

The RSC control also utilizes the error between the reference and actual dq currents and is given as follows:

$$\left. \begin{aligned} e_i &= x - x_{ref} \\ e_i &= [e_1 \quad e_2]^T \\ e_i &= [I_{dr} - I_{dr-ref} \quad I_{qr} - I_{qr-ref}] \end{aligned} \right\} \quad (30)$$

The derivative of the above errors after substituting the values from (12) is given as follows:

$$\left. \begin{aligned} \dot{e}_1 &= \frac{1}{\sigma L_r} \left(V_{dr} - R_r I_{dr} + s\sigma L_r \omega_s I_{qr} - \frac{M}{L_s} \frac{d}{dt} \varphi_{ds} \right) - \dot{I}_{dr-ref} \\ \dot{e}_2 &= \frac{1}{\sigma L_r} \left(V_{qr} - R_r I_{qr} + s\sigma L_r \omega_s I_{dr} - s\omega_s \frac{M}{L_s} \frac{d}{dt} \varphi_{ds} \right) - \dot{I}_{qr-ref} \end{aligned} \right\} \quad (31)$$

Hence, (31) can be written as:

$$\left. \begin{aligned} \dot{e}_1 &= G_1 + \frac{1}{\sigma L_r} V_{dr} - \frac{1}{\sigma L_r} R_r I_{dr} \\ \dot{e}_2 &= G_2 + \frac{1}{\sigma L_r} V_{qr} - \frac{1}{\sigma L_r} R_r I_{qr} \end{aligned} \right\} \quad (32)$$

where

$$\left. \begin{aligned} G_1 &= \frac{1}{\sigma L_r} (s\sigma L_r \omega_s I_{qr} - \frac{M}{L_s} \frac{d}{dt} \varphi_{ds}) - \dot{I}_{dr-ref} \\ G_2 &= \frac{1}{\sigma L_r} (s\sigma L_r \omega_s I_{dr} - s\omega_s \frac{M}{L_s} \frac{d}{dt} \varphi_{ds}) - \dot{I}_{qr-ref} \end{aligned} \right\}$$

The voltage tracking error e_E for GSC is given as follows:

$$e_E = E - E_{ref} \quad (33)$$

The derivative of the DC link voltage error after substituting the values from (24) is given as follows:

$$\left. \begin{aligned} \dot{e}_E &= \dot{E} - \dot{E}_{ref} \\ \dot{e}_E &= g_0(x) I_{gd} - \frac{1}{C} I_{or} + dE - \dot{E}_{ref} \end{aligned} \right\} \quad (34)$$

The error defined in this section will be utilized further to derive the control law of SMC and its variants.

5. Sliding Mode Control for DFIG Based WECS

This section will describe the various techniques and variants of SMC presented in the literature. A detailed literature review portraying the error, surfaces, typology, and remarks are also provided in this section.

5.1. First-Order Sliding Mode Control Schemes

The first-order SMC is the most basic and simple control design for DFIG-based WECS. The SMC provides a suitable compromise between torque oscillations and efficiency of power conversion [119–121]. The author in [122] proposed SMC schemes using the first-order SMC, where the surface was chosen as the power tracking error. The reference power is selected as less than the maximum power to keep an energy buffer for frequency change under abrupt load conditions. A test bench developed at NREL FAST is used to validate the proposed scheme. A similar concept was introduced in [118,123] for grid-connected WECS. The first-order SMC schemes mentioned before are of a continuous nature. Utkin in [98] stated that the SMC schemes are inherently affected by an undesirable phenomenon of chattering that proves to be harmful for the system and causes a low control accuracy, high wear and tear of system parts, and high losses. This phenomenon is due to the discontinuous switching control law in the continuous control schemes. The author in [124] suggest an exponential reaching law to eliminate the chattering problem instead of the constant reaching law. The gain in the exponential-reaching-law-based SMC is scheduled

according to the magnitude of error. The gain is increased with an increase in error and decreases with a decrease in error. The enhanced reaching law proposed by [124] is given as:

$$\dot{S} = -\Lambda S - \frac{K}{D(S)} |S|^{\gamma_x} \text{sign}(S) \quad (35)$$

where $D(S) = \alpha + (1 - \alpha)e^{-\beta_x |S|}$, $0 < \alpha < 1$, and $\beta_x > 0$.

It is evident from the above equation that the controller gain is modified between $K|S|^{\gamma_x}$ and $K|S|^{\gamma_x}/\alpha$ according to the magnitude of error. The digital control scheme based on the adaptive reaching law was introduced in [94] to achieve a switch-free control law called digital sliding mode control (DSMC) for DFIG-based WECS. The sliding motions for the digital system were initially investigated by Miloslavjevic in [120]. The authors present the idea of a quasi-sliding mode (QSM) in which the trajectory of the system is along a surface that gives a sliding-like motion instead of a switching surface. The DPC strategy is deployed with a constant switching frequency to improve the power quality and eliminate the need for the synchronous reference frame to minimize the online calculations. The surfaces selected for the design of DSMC are given as follows:

$$S_P = P_{ref}(k) - P_s(k) \quad (36)$$

$$S_Q = Q_{ref}(k) - Q_s(k) \quad (37)$$

This digitalized SMC guarantees sliding at each sampling instant [121,122]. More information on digital SMC can be found in [120,125].

Keeping in view the concept provided by the above-mentioned papers, the control law for the first-order system is derived. The errors and its derivative that are given as follows are used to derive the control law. Taking the surface as the speed error given as follows:

$$S_\Omega = e_\Omega \quad (38)$$

The derivative is given as follows:

$$\dot{S}_\Omega = \dot{e}_\Omega = \frac{T_{em}}{J} + d_3 - \dot{\Omega}_{r-ref} \quad (39)$$

Now, following the SMC procedure, taking the $\dot{S}_\Omega = 0$ and solving for equivalent term, one obtains:

$$T_{em-eq} = J(\dot{\Omega}_{r-ref} - d_3) \quad (40)$$

The RSC speed equivalent control law T_{em-eq} is obtained using (40) and the switching control part $T_{em-s} = -J k_3 \text{sign}(S_\Omega)$ and is given as follows:

$$\left. \begin{aligned} T_u &= T_{em-eq} + T_{em-s} \\ T_{em-eq} &= J(\dot{\Omega}_{r-ref} - d_3) \\ T_{em-s} &= -J(k_3 \text{sign}(S_\Omega)) \end{aligned} \right\} \quad (41)$$

The current control loop of RSC is derived by taking the surface equal to the current errors given as follows:

$$S = \begin{bmatrix} S_1 \\ S_2 \end{bmatrix} = \begin{bmatrix} e_1 \\ e_2 \end{bmatrix} \quad (42)$$

The surface derivative is given as:

$$\dot{S} = \begin{bmatrix} \dot{S}_1 \\ \dot{S}_2 \end{bmatrix} = \begin{bmatrix} \dot{e}_1 \\ \dot{e}_2 \end{bmatrix} \quad (43)$$

Now, following the SMC procedure, taking the $\dot{S} = 0$ and solving for the equivalent term, one obtains the following control law for the current loop:

$$u = h^{-1} \left[\begin{array}{l} \underbrace{\left(\frac{R_r}{\sigma L_r} I_{dr} - s\omega_s I_{qr} + \dot{I}_{dr-ref} \right)}_{\text{equivalent term}} - k_1 \text{sign}(S_1) \\ \underbrace{\left(\frac{R_r}{\sigma L_r} I_{qr} + s\omega_s I_{dr} + s \frac{MV_s}{\sigma L_r L_s} + \dot{I}_{qr-ref} \right)}_{\text{equivalent term}} - k_2 \text{sign}(S_2) \end{array} \right] \quad (44)$$

A similar procedure is followed for GSC. The surface is selected as the difference in the dc link voltage and reference voltage and is given as:

$$S_E = e_E \quad (45)$$

where the error derivative is given as follows:

$$\dot{S}_E = \dot{e}_E \quad (46)$$

By using the grid side nonlinear model and the procedure followed in the manuscript, the control law can be chosen as:

$$\left. \begin{array}{l} I_d = I_{d-eq} + I_{d-s} \\ I_{d-eq} = \frac{1}{g_0(x)} \left(\dot{E}_{ref} + \frac{1}{C} I_{0r} \right) \\ I_{d-s} = \frac{1}{g_0(x)} (-k_4 \text{sign}(S_E)) \end{array} \right\} \quad (47)$$

The operational diagram of the first-order SMC is given in Figure 5. First-order SMC is simple to handle and implement. First-order SMC only requires four gains to be controlled for its operation. Various SMC techniques employed in the literature are tabulated in Table 2.

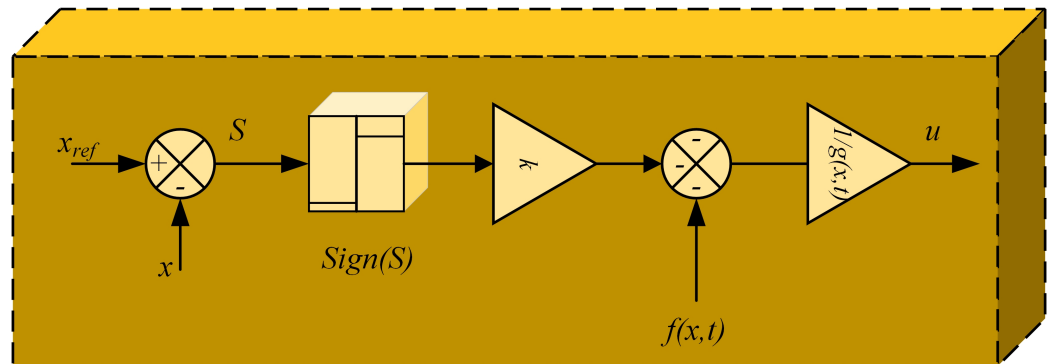


Figure 5. First-order SMC operational diagram.

Table 2. First-order SMC comparison in WECS.

Technique	Ref.	Year	Errors	Surfaces	Generator, Control, and Converter-Type Hardware	Remarks
First-order SMC	[123]	2008	$e_P = P_{ref} - P_s$	$S_P = P_{ref} - P_s$	Standalone No	–
	[88]	2013	$e_P = P_{ref}(k) - P_s(k)$ $e_Q = Q_{ref}(k) - Q_s(k)$	$S_P = P_{ref}(k) - P_s(k)$ $S_Q = Q_{ref}(k) - Q_s(k)$	DFIG BTB converter RSC control No	An SMC in discrete domain is presented to control the DFIG plant using power control. Harmonic spectra are also presented in the paper.
	[124]	2016	$e_{dc} = I_{rdc} - I_{rdc-ref}$ $\begin{bmatrix} e_{ig} \end{bmatrix} = \begin{bmatrix} e_{1g} \\ e_{2g} \end{bmatrix}$ $= \begin{bmatrix} I_{gd} - I_{gd-ref} \\ I_{gq} - I_{gq-ref} \end{bmatrix}$	$S_{dc} = e_{dc}$ $S_{ig} = e_{ig}$	PMSG Diode rectifier Boost converter NPC inverter at GSC Yes	The conventional reaching law is replaced by a new enhanced reaching law to reduce the chattering. A gain K is used to trade off between chattering and reaching. The e_{dc} is error between boost converter current and reference, whereas e_{ig} is taken as error between reference and actual grid current.
	[126]	2020	$e_P = P_{ref} - P_s$ $e_Q = Q_{ref} - Q_s$	$S_\omega = P_{ref} - P_s$ $S_Q = Q_{ref} - Q_s$	RSC side control No	Stability analysis of SMC and STSMC are presented and performance is evaluated.

5.2. Supertwisting Sliding Mode Control

Leonid Fridman et al. classify the sliding mode control into five generations [127] termed as: (1) first-order SMC, (2) second-order SMC schemes, (3) super twisting algorithms, (4) arbitrary-order SMC, and (5) continuous arbitrary SMC. The super twisting sliding mode control (STSMC) comes under the third generation and has advantages of Lipschitz disturbances with a continuous-type control signal. The authors in [96,97,128–131] proposed STSMC for WECS. The HOSMC retains the FOSMC merits, including robustness and invariance, with the capability to eliminate chattering and improve the control accuracy, eliminating the relative degree limitations [132]. Various algorithms can be applied to achieve HOSMC, and the most widely accepted is the simplified structured super twisting algorithm (STA), as it requires little target information [133,134]. The following STA structure proposed in [135] is considered here to derive the control law.

$$\left. \begin{aligned} U &= -\alpha |S|^{\frac{1}{2}} \text{sign}(S) + u_1 \\ \text{where } u_1 &= -\beta \int \text{sign}(S) \end{aligned} \right\} \quad (48)$$

where α and β are the bounded control gains determined by the uncertain disturbances of the system under investigation. Keeping in view the abovementioned advantages of STSMC, it has proven to be one of the most applied control techniques for the wind-based energy conversion control system. The various systems employing the STSMC scheme with its surfaces, errors, and system types are tabulated in Table 3. The authors in [136] proposed a voltage-mode HOSMC method where a sensorless approach is used to obtain the MPPT optimal voltage reference. The proposed voltage regulator is compared to the conventional SMC voltage controller using two different test cases that use realistic and step change wind speed profiles ranging from 5 m/s to 12 m. The performance of both controllers is presented for the entire operation period at any speed. The HOSM controllers are based on the super twisting algorithm, which requires only the measurement of the sliding variables without the use of information about the sliding constraint's time derivatives. The quadratic form Lyapunov function method is used to select controller parameters and ensure the closed-loop system's finite time stability. Simulations under wind fluctuation and load perturbation show that the proposed control strategy is well-suited for controlling the DFIG-WECS and that the control objectives are met in a variety of conditions [130]. The author in [96,131] applies STA for maximum power extraction with finite, reaching time, robustness, and chattering-free control with pre-assumed upper bounds of the externally applied disturbances. The drawback of upper bound pre-assumption was overcome by the authors in [137]. Initially, an adaptive multivariable control scheme was proposed with an adaptive gain adjustment and finite time convergence. A novel Lyapunov stability theory is proposed by [137] to prove the finite time convergence and stability of the proposed control scheme. An adaptive super twisting control scheme was presented in [118] for floating wind turbines. The authors of [131] developed a fault-tolerant SOSMC controller for a DFIG-based 1.5 MW three-blade WT MPPT control subjected to external disturbances and un-modeled dynamics. The authors of [135] designed SOSMC to solve the problem of grid frequency alterations and unbalanced voltage sags. The various systems employing the STSMC scheme with its surfaces, errors, and system types are tabulated in Table 3, whereas the operational diagram is shown in Figure 6.

Using the equivalent term derived in (41) and the STA-based control law, a new HOSMC-based control paradigm is derived as follows:

$$\left. \begin{aligned} T_u &= T_{em-eq} + T_{em-s} \\ T_{em-eq} &= J(\dot{\Omega}_{r-ref} - d_3) \\ T_{em-s} &= J\left(-\alpha_\omega |S_\Omega|^{\frac{1}{2}} \text{sign}(S_\Omega) - \beta_\omega \int \text{sign}(S_\Omega)\right) \end{aligned} \right\} \quad (49)$$

Similarly, for the RSC current control, the equivalent part in (44) is used with the STA-based control law for the derivation of the following RSC control :

$$u = h^{-1} \left[\begin{aligned} &\left(\frac{R_r}{\sigma L_r} I_{dr} - s\omega_s I_{qr} + \dot{I}_{dr-ref} \right) + \left(-\alpha_1 |S_\Omega|^{\frac{1}{2}} \text{sign}(S_\Omega) - \beta_1 \int \text{sign}(S_\Omega) \right) \\ &\left(\frac{R_r}{\sigma L_r} I_{qr} + s\omega_s I_{dr} + s \frac{M V_s}{\sigma L_r L_s} + \dot{I}_{qr-ref} \right) + \left(-\alpha_2 |S_\Omega|^{\frac{1}{2}} \text{sign}(S_\Omega) - \beta_2 \int \text{sign}(S_\Omega) \right) \end{aligned} \right] \quad (50)$$

The GSC uses the same surface that comprises the error between the DC link voltage and its reference to transfer the power from the RSC to the grid. Using the STA algorithm proposed in (48) for the switching control part and equivalent law from (47), the new HOSMC law for GSC is given as follows:

$$I_d = \frac{1}{g_0(x)} \left(\dot{E}_{ref} + \frac{1}{C} I_{0r} - \lambda_E |S_E|^{\frac{1}{2}} \text{sign}(S_E) - \beta_E \int \text{sign}(S_E) \right) \quad (51)$$

The operational diagram of STSMC is given in Figure 6. Keeping in view the above equations, the super twisting SMC increases the complexity of the system. The gains are also increased as the RSC now requires six gains, whereas GSC requires two gains to be tuned. The STSMC-based control schemes improve the system performance in terms of chattering elimination but can reduce the robustness of the system due to the continuous term in the control law.

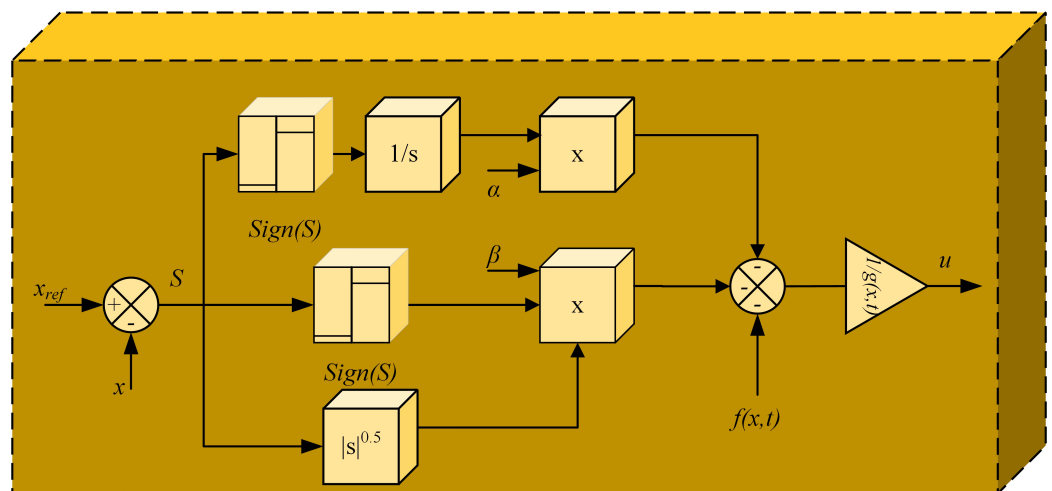


Figure 6. Super-twisting-based SMC operational diagram.

Table 3. High-order SMC schemes comparison for WECS.

Technique	Ref	Year	Errors	Surfaces	Generator, Control , and Converter-Type Hardware	Remarks
High-order SMC	[138]	2008		$S_1 = K_{opt}\Omega_e^2 - \frac{3}{2}\frac{P}{\omega_e}\phi_{sr}i_q$ $S_2 = P_{ref}(t) - \frac{3}{2}\phi_{sr}i_q\omega_e$	PMSG Rectifier and inverter No	Rectifier is controlled using STSMC with two different surfaces for two operation modes, which are optimum power conversion and power regulation.
	[116]	2012	$e_\Omega = \Omega_{ref} - \Omega_r$ $e_i = I_{rd} - I_{rd-ref}$	$S_\omega = \Omega_{ref} - \Omega_r$ $S_i = I_{rd} - I_{rd-ref}$	DFIG BTB converters Yes	STSMC-based high-order control scheme is proposed. The simulation is carried out in FAST wind turbine simulator. A chattering-free and robust behavior with less mechanical stress is experienced.
	[139]	2012	$e_\Omega = \Omega_{ref} - \Omega_r$	$S_\omega = \frac{1}{J}\Omega_{ref} - \Omega_r$	DFIG No	A Lyapunov-based modified STSMC is presented with variable gains. The results are validated using extensive simulations.
	[140]	2013	$e_T = T_{e,ref} - T_e$ $e_i = Q_{s,ref} - Q_s$	$S_T = T_{e,ref} - \frac{3pL_mV_s}{2\omega_sL_s}i_{qr}$ $S_i = Q_{s,ref} + \frac{3L_mV_s}{2L_s}\left(i_{dr} - \frac{V_s}{\omega_sL_m}\right)$	DFIG BTB converters RSC control No	STSMC with variable gains is presented in this paper and convergence analysis is provided for DFIG-based WECS.
	[135]	2014	$e_T = T_{e,ref} - T_e$ $e_i = I_{rd} - I_{rd-ref}$	$S_T = T_{e,ref} - T_e$ $S_i = I_{rd} - I_{rd-ref}$	DFIG BTB converter No	An STSMC-based second-order SMC is presented using FAST code
	[141]	2016	$e_\Omega = \Omega_{ref} - \Omega_r$ $e_E = E^* - E$	$S_\omega = \Omega_{ref} - \Omega_r$ $S_E = E^* - E$	PMSG IGBT 8837 BTB Yes	
	[142]	2017	$e_i = I_{rdq} - I_{rdq-ref}$ $e_E = I_{gdq} - I_{gdq-ref}$	$S_i = I_{rdq} - I_{rdq-ref}$ $S_E = I_{gdq} - I_{gdq-ref}$	DFIG BTB converters RSC and GSC control No	A fault ride through technique using fuzzy integral terminal STSMC is presented in this paper.
	[143]		-	$S_T = T_{ref} + T_g$ $S_E = Q_{g,ref} - Q_g$	DFIG BTB converters No	A second-order SMC is proposed and made adaptive using time-varying receding horizon. The conservative bounds are calculated and then adaptation strategy is proposed.

Table 3. Cont.

Technique	Ref	Year	Errors	Surfaces	Generator, Control , and Converter-Type Hardware	Remarks
	[144]	2019	$e_\varphi = \varphi_{r-ref} - \varphi_r$ $e_T = T_{e,ref} - T_e$	$S_\varphi = \varphi_{r-ref} - \varphi_r$ $e_T = T_{e,ref} - T_e$	DFIG RSC control No	An STSMC is proposed where the gains of the STSMC are optimally selected using new rooted tree optimization.
	[145]	2020	$e_\Omega = \Omega_{ref}\Omega_r$	$S_\omega = \dot{e}_\omega + k e_\omega$	RSC outer loop control No	A new structure of SMC based on switching sector is presented to minimize the chattering phenomenon.
	[146]	2019	$e_\Omega = \Omega_{ref} - \Omega_r$	$S_\omega = \dot{e}_\omega + k e_\omega ^{\frac{2}{3}} \text{sign}(e_\omega)$	RSC control Yes	A new inertial perturb-and-observe MPPT technique is presented. A third-order STSMC is proposed for speed tracking.
	[136]	2020	$e_{E1} = (E - E^*)$ $e_{E2} = -\int (E - E^*)dt$	$S_E = \lambda e_{E1} + e_{E2}$	PMSG Rectifier + Boost converter + Inverter No	An SOSMC is presented for the boost converter in PMSG -based WECS to control the DC link voltage.
	[147]	2020	$e_P(t) = P_s^* - P_s$ $e_Q(t) = Q_s^* - Q_s$	$S_1 = e_P(t) + K_P \int e_P(\tau)d\tau$ $S_2 = e_Q(t) + K_Q \int e_Q(\tau)d\tau$	DFIG RSC control Yes	Am HOSMC is presented with enhancing power quality using six power compensation techniques.
	[126]	2020	$e_p = P_{ref} - P_s$ $e_Q = Q_{ref} - Q_s$	$S_\omega = P_{ref} - P_s$ $S_Q = Q_{ref} - Q_s$	RSC side control NO	Stability analysis of SMC and STSMC is presented, and performance is evaluated.
	[137]	2021	$e_p = P_s - P_{ref}$ $e_Q = Q_s - Q_{ref}$	$S_1 = e_P(t) + K_P \int e_P(\tau)d\tau$ $S_2 = e_Q(t) + K_Q \int e_Q(\tau)d\tau$	DFIG RSC control No	Adaptive STSMC is proposed for DFIG-based WECS. The adaptive gains are given as follows: $w = -k1 \frac{s}{\ S\ ^{\frac{1}{2}}} + r$ $r = -k2 \frac{s}{\ S\ }$, where $[w = w_p, w_Q]^T, [r = r_p, r_Q]^T$

5.3. Adaptive High-Order Sliding Mode Control

The two controller gains α and β are fixed and chosen to control the performance in STA algorithm-based control laws. In each control law above, these gains are usually determined by the uncertainties boundary, which depends on various factors. The boundary of uncertainty is usually estimated adequately in the control law design process, resulting in unnecessary gains. The issues of unnecessary constant gains are resolved by using adaptive sliding mode control schemes (ASMC). ASMC-based schemes combine SMC theory and adaptive algorithm attributes to adjust the gain to be small enough to maintain the sliding motion. [137] Hao Chen et al. in [119] recently proposed an adaptive STA-based SMC scheme for a PMSG-based tidal stream turbine. The HOSMC scheme mentioned above can be made adaptive using the gains given as follows:

$$\left. \begin{aligned} \dot{\alpha} &= \begin{cases} \sigma\sqrt{\gamma_1/2}, & \text{if } S \neq 0 \\ 0, & \text{if } S = 0 \end{cases} \\ \beta &= \varepsilon\alpha \end{aligned} \right\} \tag{52}$$

The stability proof for the adaptive STSMC can be found in [119] with the Lyapunov function given by [148], and the operational diagram is shown in Figure 7.

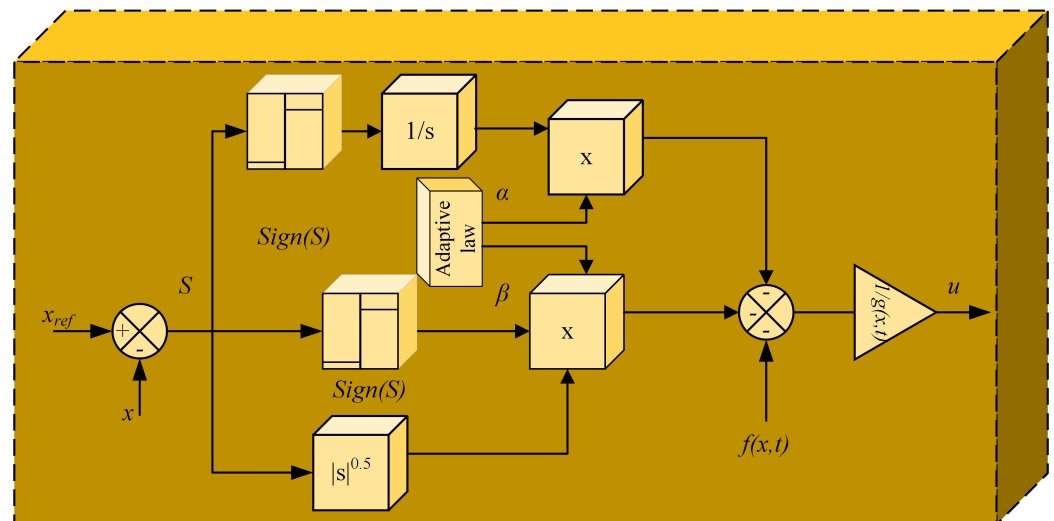


Figure 7. Adaptive super twisting SMC operational diagram.

A similar adaptive HOSMC was presented in [137]. A multivariable adaptive multivariable super twisting control scheme for DFIG-WECS MPPT was proposed with unknown upper bounds of disturbances. The proposed scheme has finite-time convergence, chatter-free behavior, and excellent robustness properties against external disturbances and parameter uncertainties. The surfaces are selected as follows:

$$\left. \begin{aligned} S_1 &= e_P(t) + K_P \int e_P(\tau) d\tau \\ S_2 &= e_Q(t) + K_Q \int e_Q(\tau) d\tau \end{aligned} \right\} \tag{53}$$

A new discontinuous control law represented by w was proposed and is given as follows:

$$\left. \begin{aligned} w &= -k_1 \frac{S}{\|S\|^{\frac{1}{2}}} + r \\ \dot{r} &= -k_2 \frac{S}{\|S\|} \end{aligned} \right\} \tag{54}$$

where $[w = w_P, w_Q]^T$ and $[r = r_P, r_Q]^T$

5.4. Integral Type Sliding Mode Control

Utkin et al. proposed the ISMC to address the robustness in the reaching phase of conventional SMC [149]. The sliding phase is enforced in the overall system response, whereas the system's order is maintained in ISMC [106]. Several ISMC-based strategies have been proposed in the literature for WECS to improve the conventional SMC performance tabulated in Table 4. For instance, the author in [150] presented ISMC with a disturbance observer for WECS. The proposed observers estimate the value of the aerodynamic torque as well as the d- and q-axis disturbances. The designed aerodynamic torque observer can estimate the wind speed with fast-changing behavior. The proposed observers' and controller's stability is examined using Lyapunov stability theory. The authors in [151] validated ISMC to control the three-blade wind-turbine-based WECS optimally. The analysis of the results reveals that the potential gain in power capture can be achieved by improving the performance of tracking, which always comes at the cost of an increased variation in input torque, which ultimately increases the stress in the system. The main advantage of ISMC is the continuity in the control law in the region 2.5, which is derived for region 2, whereas, for existing baseline controllers, a separate control law is required in region 2.5 for satisfactory operation. A direct power control strategy for WECS based on intelligent ISMC with a sliding mode module is presented in [152] to compensate for the disturbance in the system and circumvent the error in disturbance estimation. The ISMC-based control law comprises both continuous and discontinuous control components to increase the robustness of the system. This controller is made up of two nested controllers: an intelligent proportional integral controller that is supplemented by a sliding mode compensated controller. To derive a typical ISMC scheme for DFIG-WECS, the surface S and its derivative \dot{S} presented based on ISMC theory are given as:

$$\left. \begin{aligned} S_{\Omega} &= c_5 e_{\Omega} + c_6 \int e_{\Omega} dt \\ \dot{S}_{\Omega} &= c_5 \dot{e}_{\Omega} + c_6 e_{\Omega} \end{aligned} \right\} \quad (55)$$

Following the SMC theory and surface given in (55), the control law comprising an equivalent and discontinuous term is given as:

$$T_u = J \left(\dot{\Omega}_{r-ref} - d_3 - \left(\frac{c_6}{c_5} e_{\Omega} \right) - \frac{k_3}{c_5} \text{sign}(S_{\Omega}) \right) \quad (56)$$

The surface S_1 and S_2 and their derivatives \dot{S}_1 and \dot{S}_2 for the current control loop, presented on the basis of ISMC theory, are given as:

$$\left. \begin{aligned} \begin{bmatrix} S_1 \\ S_2 \end{bmatrix} &= \begin{bmatrix} c_1 e_1 + c_2 \int e_1 dt \\ c_3 e_2 + c_4 \int e_2 dt \end{bmatrix} \\ \begin{bmatrix} \dot{S}_1 \\ \dot{S}_2 \end{bmatrix} &= \begin{bmatrix} c_1 \dot{e}_1 + c_2 e_1 \\ c_3 \dot{e}_2 + c_4 e_2 \end{bmatrix} \end{aligned} \right\} \quad (57)$$

The resulting control law for the current loop control is now given as:

$$u = h^{-1} \begin{bmatrix} \frac{R_r}{\sigma L_r} I_{dr} - s \omega_s I_{qr} + \dot{I}_{dr-ref} - \frac{c_2}{c_1} e_1 - \frac{k_1}{c_1} \text{sign}(S_1) \\ \frac{R_r}{\sigma L_r} I_{qr} + s \omega_s I_{dr} + s \frac{M V_s}{\sigma L_r L_s} + \dot{I}_{qr-ref} - \frac{c_4}{c_3} e_2 - \frac{k_2}{c_3} \text{sign}(S_2) \end{bmatrix} \quad (58)$$

For GSC control, the surface is chosen as follows:

$$\left. \begin{aligned} S_E &= c_7 e_E + c_8 \int e_E dt \\ \dot{S}_E &= c_7 \dot{e}_E + c_8 e_E \end{aligned} \right\} \quad (59)$$

By using the grid side nonlinear model and the procedure for SMC law derivations, the control law can be given as:

$$I_d = \frac{1}{g_0(x)} \left(\dot{E}_{ref} + \frac{1}{C} I_{0r} - \frac{c_8}{c_7} (e_E) - \frac{k_4}{c_7} \text{sign}(S_E) \right) \quad (60)$$

Based on the above derivations, the overall control scheme for RSC needs nine gains to be tuned, whereas three gains are needed for the GSC side control. The operational diagram of ISMC is given in Figure 8.

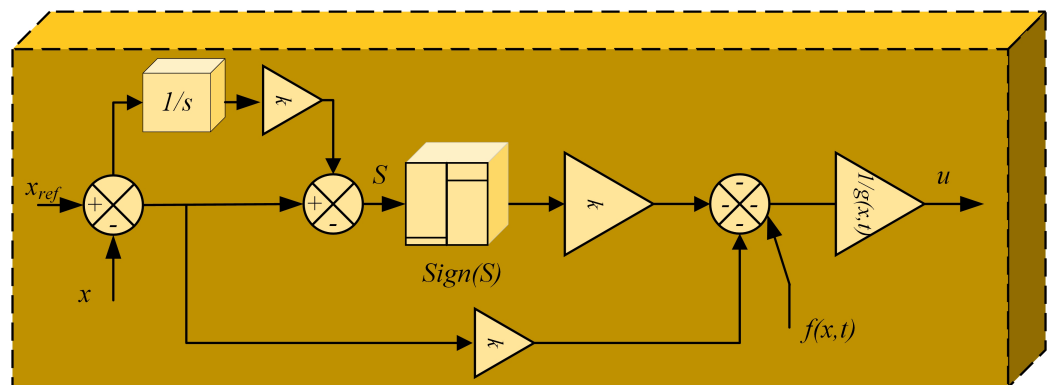


Figure 8. Integral SMC operational diagram.

Table 4. Integral SMC schemes comparison for WECS.

Technique	Ref	Year	Errors	Surfaces	Generator, Control, and Converter-Type Hardware	Remarks
Integral SMC	[153]	2009	$e_T = T_{e,ref+-} - T_{e+-}$ $e_i = Q_{ref+-} - Q_{g+-}$	$S_T = e_T + \int e_T dt$ $S_i = e_i + \int e_i dt$	DFIG BTB converters RSC control Yes	Integral SMC is proposed to remove the pulsations on torque and power at frequency twice the grid frequency. Concept of positive and negative SRF is used.
	[110]	2010	$e_P(t) = P_s^* - P_s$ $e_Q(t) = Q_s^* - Q_s$	$S_1 = e_P(t) + K_P \int e_P(\tau) d\tau$ $S_2 = e_Q(t) + K_Q \int e_Q(\tau) d\tau$	DFIG BTB converters RSC control No	DPC of DFIG-based WECS is presented and compared with conventional vector control and look-up-table-based DPC.
	[154]	2011	$e_i = I_{rdq-ref}^{+-} - I_{rdq}^{+-}$	$S_i = e_i + \int_0^t e_i dt$	DFIG BTB converters RSC control No	Concept of positive and negative SRF is used to remove the pulsations on torque and reactive power using ISMC.
	[155]		$e_T = T_{e,ref} - T_e$ $e_Q(t) = Q_s^* - Q_s$	$S_1 = e_i(t) + K_P \int e_i(\tau) d\tau$ $S_2 = e_Q(t) + K_Q \int e_Q(\tau) d\tau$ surface derivative is: $\dot{S} = -\frac{k S ^\alpha}{N(S)} \text{sign}(S)$	RSC control No	RSC control is presented with a new exponential reaching law introduced in the derivative of surface, where the surface is taken as integral type surface.
	[156]	2018	$e_i = I_{rdq} - I_{rdq-ref}$	$S_1 = -e_i(t) + K \int_0^t e_P(\tau) d\tau + e_i(t_0) + y_r(t) - y_r(t_0)$	PMSG BTB converters Yes	An integral SMC with integral and novel proportional integral-based surfaces is proposed.
	[157]	2020	$e_\Omega = \Omega_{ref} - \Omega_r$ $e_T = T_{e,ref} - T_e$ $e_i = I_{sd} - I_{sd-ref}^*$	$S(x) = G(x(t) - x(0)) - G \int_0^t (Ax(t) + Bu_{SDRE}(t)) dt$ where $x = \Omega_r, T_e, I_{sd}$	PMSG	Integral SMC is designed using state dependent Ricatti equation (SDRE) with the nonlinear control law based on Ricatti and Lyapunov equation.
	[158]	2020	$e_\Omega = \Omega_{ref} - \Omega_r$ $e_i = I_{rdq} - I_{rdq-ref}$	$S_\omega = A e_\omega - \frac{pL_m\phi_s}{L_s} i_{qr}$ $S_{i_{rd}} = e_i + \frac{R_r}{ \sigma L_r} \int_0^t e_i d\tau$	DFIG RSC control No	Comparative analysis of SMC and H_∞ control is presented. SMC provided good transient performance whereas H_∞ provided less tracking error.

Table 4. Cont.

Technique	Ref	Year	Errors	Surfaces	Generator, Control, and Converter-Type Hardware	Remarks
	[159]	2020	$e_{\Omega} = \Omega_{ref} - \Omega_r$	$S(t) = \Omega_r + k_1 \cdot \Omega_r + k_2 \int_0^t (\Omega_r - \Omega_{ropt}) d\tau$	PMSG RSC control No	The uncertain wind turbine dynamics are controlled and estimated using recurrent neural network. Adaptive ISMC is proposed to track optimum rotation speed.
	[160]	2021	$e_{E1} = - \int (E - E^*) dt$ $e_{E2} = (E - E^*)$ $e_{E2} = (I_L - I_L^*)$	$S(e_1, e_2, e_3) = [e_1, \lambda + e_2, \gamma e_3]$ with $\gamma = LC$	PMSG Rectifier + Buck converter + Inverter Yes	An SMC technique with new MPPT algorithm is proposed to control the DC link voltage.
	[161]	2021	$e_P(t) = P_s^* - P_s$ $e_Q(t) = Q_s^* - Q_s$	$S = Ce$	PMSG RSC control Yes	An event-triggered integral SMC is presented with extended state observer. The event triggering is used to minimize the communication between execution units and controller.

5.5. Terminal Sliding Mode Control

Well-documented research works highlights the SMC theory and application, such as [125,162,163]. The asymptotic stability of SMC structures is based on Lyapunov theory underpinned by the Lipschitz condition for ordinary differential equations (ODEs). The asymptotic stability nature shows a slow state convergence rate of the system dynamics near the equilibrium [164]. This depicts that the finite-time convergence to the equilibrium point is not possible in finite time. The author in [165] achieved finite-time convergence and utilized a terminal attractor as a first-order dynamics with fractional power to add some non-smoothness in the neural learning rule. The authors in [166] extended the terminal attractor idea to SMC schemes and proposed a terminal SMC (TSMC) scheme for the second-order system. Similarly, the authors in [167] proposed TSMC for a single-input–single-output (SISO) of higher order and the same applies for authors in [168,169] for multi-input–multi-output systems. The singularity problems in TSMC schemes were solved in the early 2000s [170], followed by fast TSMC [171] and continuous TSMC [172]. In the previous 5 years, the TSMC enjoyed an over 20% annual growth in the theoretical and application contributions [164]. The authors in [166] used the following form of terminal attractors to control the second-order system:

$$S = \dot{x} + \beta|x|^\lambda \text{sign}(x) \quad (61)$$

where x is a variable and, $\beta > 0$ and $0 < \lambda < 1$. Initially, the value of λ was taken as q/p , where q and p are positive integers. The time for x to reach 0 when $x(0) \neq 0$ and $s = 0$ is given as:

$$t_s = \beta^{-1}(1 - \lambda)^{-1}|x(0)|^{1-\lambda} \quad (62)$$

The author in [171] proposed a fast TSMC (FTSMC) and increased the convergence rate by modifying (61) as follows:

$$S = \dot{x} + \alpha x + \beta|x|^\lambda \text{sign}(x) \quad (63)$$

where the convergence time is given as:

$$t_s = \alpha^{-1}(1 - \lambda)^{-1} \left(\ln \left(\alpha|x(0)|^{(1-\lambda)} + \beta \right) - \ln(\beta) \right) \quad (64)$$

During the sliding phase, when $S = 0$, the Equation (64) becomes as follows:

$$\dot{x} = -\alpha x - \beta|x|^\lambda \text{sign}(x) \quad (65)$$

Equations (64) and (65) shows that, for FTSMC, the system will reach $x = 0$ faster than (61). The SMC design process used derivatives of the sliding surface, which can cause the problem of singularity due to the presence of $\lambda - 1$ in the time derivative of $\beta|x|^\lambda \text{sign}(x)$, i.e., $\beta\lambda|x|^{\lambda-1} \text{sign}(x)\dot{x}$, leading to infinite control. A nonsingular TSMC proposed by [170] overcame the problem of singularity given as follows:

$$S = \beta x + |\dot{x}|^\lambda \text{sign}(\dot{x}) \quad (66)$$

Here, $1 < \lambda < 2$. For the system having a relative degree > 1 , the singularity problem is overcome by a modified version of TSMC known as integral TSMC (ITSMC) and is given as follows:

$$S(t) = x(t) + \beta \int_0^t |x(\tau)|^\lambda \text{sign}(x(\tau)) d\tau \quad (67)$$

Keeping in view the above theoretical considerations of TSMC, a major contribution has been added in the literature for the application of TSMC in DFIG-based WECS. A thorough literature review of TSMC for DFIG-based WECS is tabulated in Table 5. For instance, the author in [173] proposed adaptive FTSMC for DFIG-based WECS to mitigate the chat-

tering in the system dynamics. The author in [174] proposed ITSMC for the direct power control of DFIG-based WECS. A discrete time TSMC is proposed in [175] for PMSG-based WECS, where the authors achieved an efficiency of 94%. The authors in [173] applied a non-linear FTSMC to obtain faster convergence. The authors developed a higher-order SMC to address the control problem of DFIG-based WECS in a variety of challenging situations. To reduce chattering, they used a fast adaptive TSMC with a nonlinear sliding surface. The proposed controller demonstrated a greater robustness to wind speed variations and external disturbances than the feedback linearization and conventional PI methods. The surface utilized is given as follows:

$$S_i = \beta_{i1}e_i + \beta_{i2}|\dot{e}_i|^{\lambda_1}\text{sign}(\dot{e}_i) + \beta_{i3}|\dot{e}_i|^{\lambda_2}\text{sign}(\dot{e}_i) \quad (68)$$

Authors in [174] proposed a strategy that used the abc frame of reference, and its gain parameters were dynamically defined based on the absolute value of the respective sliding surfaces. The analysis of the results showed that the proposed controller for the DFIG is very effective in reducing inter-area oscillations in the multimachine network at both low and high wind speeds. The robustness and stability of the proposed control strategy for both the RSC and the GSC are validated by a time-domain mathematical simulation in the MATLAB/EDITOR environment, and a practical simulation in the MATLAB/ SIMULINK environment. The test cases selected included “sub” and “super” synchronous mode of operation of the DFIG and “lower” and “higher” wind speed operations for the stator reactive power reference and random wind speed variation. In order to reduce chattering, the authors proposed a nonlinear terminal sliding surface, which is given as follows:

$$S(t) = e(t) + \beta \int_0^t |x(\tau)|^\lambda d\tau \quad (69)$$

The authors in [176] investigated the three-phase GSC control problem of variable speed PMSG-based WECS. To control the active and reactive powers exchanged between the converter and the grid, the authors proposed two integral-type TSMC controllers with attenuated chattering. They used integrators to soften the switching signals and generate continuous control signals to reduce chattering. The controller’s time-varying gain is designed to reduce extra control effort and avoid overestimation of system uncertainties. Virtual control is used to regulate the GSC’s input currents by forcing the voltages in the GSC’s three capacitors to track the virtual signals. The controller design takes into account both matched and unmatched parametric uncertainties to ensure the system’s robustness.

Table 5. Terminal-based SMC comparison in WECS.

Technique	Ref.	Year	Errors	Surfaces	Generator, Control, and Converter-Type Hardware	Remarks
Terminal SMC	[173]	2015	$e_P(t) = P_s^* - P_s$ $e_Q(t) = Q_s^* - Q_s$	$S_P = \beta_{d1}\tau_1 + \beta_{d2} \tau_2 ^{\varphi_{d1}} \text{sign}(\tau_2) + \beta_{d3} \tau_2 ^{\varphi_{d2}} \text{sign}(\tau_2)$ $S_Q = \beta_{q1}\tau_3 + \beta_{q2} \tau_4 ^{\varphi_{q1}} \text{sign}(\tau_4) + \beta_{q3} \tau_4 ^{\varphi_{q2}} \text{sign}(\tau_4)$ <p>where $\beta > 0$, and $\tau_1 = e_P, \tau_2 = \dot{e}_P, \tau_3 = e_Q, \tau_4 = \dot{e}_Q$</p>	DFIG BTB converters RSC / GSC control No	An adaptive fast TSMC is presented in this paper. The GSC is controlled using PI control scheme to mitigate the chattering and remove the control input saturation.
	[174]	2018	$e_P(t) = P_s^* - P_s$ $e_Q(t) = Q_s^* - Q_s$	$S_1 = e_P + \beta \int_0^t e_P^{q/p} d\tau$ $S_2 = e_Q + \beta \int_0^t e_Q^{q/p} d\tau$	DFIG BTB converters RSC No	The transient response of DFIG-WECS is improved using adaptive TSMC. The analysis is conducted for both sub-synchronous and synchronous modes of operation.
	[176]	2018	$e_E = I_{E\alpha\beta} - I_{E\alpha\beta}^*$	$S_E = \dot{e}_E + \beta_{g\alpha\beta} e_E$	PMSG Yes	An integral type of terminal SMC is proposed in the paper for the power conversion between grid and GSC. Time-varying gains are adopted for the reduction in control energy waste.
	[175]	2019	$e(k) = E(k) - E(k - 1)$	$S_E(k) = e(k) + \beta \sum_{i=0}^k e(i)^\lambda$	PMSG Rectifier + Boost converter Yes	This paper proposed a discrete time terminal SMC for PMSG WECS. The author achieved 94% efficiency at 9 m/s wind speed.
	[177]	2020	$e_i = I_{rdq} - I_{rdq-ref}$ $e_E = I_{gdq} - I_{gdq}^*$	$S_1(t) = \dot{e}_{rd} + \beta_{rd}e_{rd} + \alpha_{de}e_{rd}^{q/p}$ $S_2(t) = \dot{e}_{rq} + \beta_{rq}e_{rq} + \alpha_{qe}e_{rq}^{q/p}$ $S_{E1}(t) = \dot{e}_{gd} + \beta_{gd}e_{gd} + \alpha_{dg}e_{rd}^{q/p}$ $S_{E1}(t) = \dot{e}_{gq} + \beta_{gq}e_{gq} + \alpha_{qg}e_{gq}^{q/p}$	DFIG BTB converters RSC/GSC control No	A chattering-free ITSMC is proposed where the fuzzy control theory is used to tune the gains.

5.6. Fuzzy logic Sliding Mode Control

Fuzzy logic control (FLC) has added many features to express human thinking ambiguities by supplanting conventional techniques. FLC has a good feature of dealing with an unknown method [178]. The estimation of system parameter uncertainties increases the adjustability of SMC's switching gain, resulting in chattering attenuation and controller robustness [179]. FLC theory has been employed to SMC in several ways. Certain problems including chattering in the sliding phase, state estimation, discontinuous part estimation, signum function approximation, and complex have tuning in SMC and its variants have been mitigated using FLC theory. For instance, ref. [180] proposed a FLC scheme for a PMSG based WECS. The authors used a boost converter to control the dc link voltage. The input power and dc link current is used to approximate the dc link voltage. This FLC's basic operational principle is to perturb the DC-side voltage V_{dc} and observe the corresponding variation in the DC-side power P_{dc} . If the power increases with the most recent voltage increase, the search will continue in the same direction. If, on the other hand, the voltage increase reduces the DC-side power, the searching process will be reversed. The proposed FLC-based system is shown in Figure 9. The same scheme is proposed by the authors in [181], but, here, the input power and voltage were used to calculate the dc link current using FLC theory. The authors in [182] utilized the FLC theory and approximated the discontinuous part of the SMC scheme and improved the SMC performance by replacing the chattering source by FLC. The drawbacks of robust controllers were avoided by using this design, where, to eliminate chattering, the fuzzy-based variable switching gain technique was introduced. The same approach is used by [183] and the signum function is replaced by FLC to mitigate the chattering phenomenon. Moreover, the membership function is adjusted using the PSO-GSA optimization algorithm. Using the scheme presented in [183], an FLC theory applied to SMC is explained here.

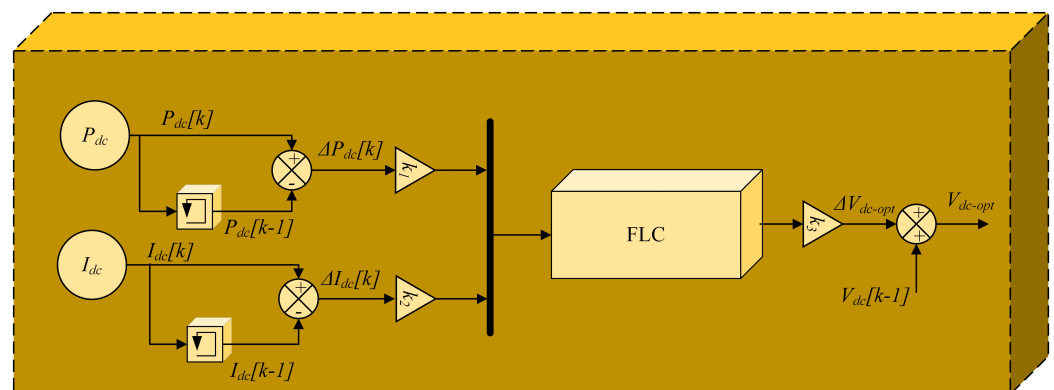


Figure 9. FLC-based system presented by [180]. Reprinted with permission from Ref. [180]. Copyright 2015 Elsevier.

The authors selected the tracking error e_j as an input to the fuzzy system $v_{j,h} = \rho_j \text{sign}(e_j)$ as its output. In the next step, the fuzzy rules are decided and are given as follows:

Rule 1 : If S_j is P , then $u_{j,h}$ is PE ;

Rule 2 : If S_j is Z , then $u_{j,h}$ is ZE ;

Rule 3 : If S_j is N , then $u_{j,h}$ is NE ;

where the output variable $v_{j,h}$ fuzzy labels are Z : Zero, N : Negative, P : Positive and the fuzzy labels for the input variables S_j are ZE : Zero effort, NE : Negative effort, and PE : Positive effort.

The Max-Min method is used to perform the inference and thus the control law can be expressed as follows:

$$v_{j,h} = \frac{\sum_{i=1}^3 \mu_{j,i} \rho_{j,i}}{\sum_{i=1}^3 \mu_{j,i}} = \mu_{j,1} \rho_{j,1} + \mu_{j,2} \rho_{j,2} + \mu_{j,3} \rho_{j,3} \quad (70)$$

where $0 \leq \mu_{i,1} \leq 1$ for $i = 1, 2, 3$ are the firing strengths of the three fuzzy rules; and $\rho_{j,1} = \rho_j$, $\rho_{j,2} = 0$ and $\rho_{j,3} = -\rho_j$ are the center of the output membership functions ZE, NE, and PE, respectively. Various cases will be triggered depending on the input to the fuzzy system. Thus, the fuzzy-based control law can be expressed as follows:

$$\left. \begin{aligned} T_u &= T_{em-eq} + T_{em-s} \\ T_{em-eq} &= J(\dot{\Omega}_{r-ref} - d_3) \\ T_{em-s} &= -Jv_{j,h} \end{aligned} \right\} \quad (71)$$

For the RSC current control, the control law will take the following form:

$$u = h^{-1} \left[\begin{aligned} &\left(\frac{R_r}{\sigma L_r} I_{dr} - s\omega_s I_{qr} + \dot{I}_{dr-ref} \right) - v_{j,h} \\ &\left(\frac{R_r}{\sigma L_r} I_{qr} + s\omega_s I_{dr} + s \frac{MV_s}{\sigma L_r L_s} + \dot{I}_{qr-ref} \right) - v_{j,h} \end{aligned} \right] \quad (72)$$

By using the grid side nonlinear model and the procedure followed in Section 5.1, the control law under a fuzzy control structure is given as:

$$\left. \begin{aligned} I_d &= I_{d-eq} + I_{d-s} \\ I_{d-eq} &= \frac{1}{g_0(x)} \left(\dot{E}_{ref} + \frac{1}{C} I_{0r} \right) \\ I_{d-s} &= \frac{1}{g_0(x)} \left(-v_{j,h} \right) \end{aligned} \right\} \quad (73)$$

Without requiring a detailed mathematical model, a fuzzy logic controller can track the maximum power point more efficiently, especially in the presence of frequently changing wind conditions. This heuristic-reasoning-based automatic control approach has the added benefits of adaptability, simplicity, extending operating ranges, and being insensitive to parametric uncertainties [180]. The various fuzzy-based control schemes are tabulated in Table 6.

Table 6. Fuzzy-logic-based SMC comparison in WECS.

Technique	Ref	Year	Errors	Surfaces	Generator, Control, and Converter-Type Hardware	Remarks
Fuzzy Logic SMC	[180]	2015	$P_{dc}, I_{dc} \rightarrow FL \rightarrow E^*$ $e_{E1} = (E - E^*)$ $e_{E2} = \dot{e}_{E1}$ $e_{E3} = -\int (E - E^*) dt$	$S = k_1 e_{E1} + k_2 e_{E2} + k_3 e_{E3}$	PMSG Diode rectifier +Boost converter Yes	The authors proposed fuzzy-logic-based ISMC to track the derived voltage. FL is used to calculate the E^* . An integral-based SMC is adopted using the FL output.
	[181]	2015	$P_{dc}, V_{dc} \rightarrow FL \rightarrow I_{dc,opt}$ $e_E = I_{dc,opt} - I_{dc}$	$S_E = I_{dc,opt} - I_{dc}$	PMSG Diode rectifier + Boost converter Yes	The authors proposed fuzzy-logic-based SMC to reduce the harmonics in GSC current. FL is used to calculate the $I_{dc,opt}$. A double-integral-based SMC is adopted using the FL output.
	[182]	2016	$e_\omega = \Omega_{ref} - \Omega_r$ $e_q = q - \Omega_{ref}$ where $q = -\frac{T_{qm}}{J} - \frac{B}{J} + d$	$S_\Omega = e_q + \hat{d} + ce_\omega$ $S_q = i_d$	PMSG RSC control No	A fuzzy-based SMC is presented with disturbance observer. The discontinuous part is estimated using fuzzy control theory.
	[183]	2019	$e_i = I_{rdq} - I_{rdq-ref}$	$S_i = I_{rdq} - I_{rdq-ref}$	DFIG BTB converters RSC control No	The authors proposed fuzzy-logic-based SMC to reduce the chattering by replacing the sign function with FL control theory. PSO-GSA optimization is used to adjust the membership functions.

6. Passivity and AI Based Sliding Mode Control

The passivity-based controllers gained attention due to the energy-based approach used to guarantee stability. It reshapes the natural energy of the system by considering the energy properties and injecting the damping terms. An SMC strategy based on the integral control theory and considering the energy properties of brush-less DFIG was proposed in [173] to regulate the power factor and active power. A Hamiltonian model of DFIG was developed on the basis of a seventh-order model and then used to propose a robust SMC-based control scheme. The surface selected

$$s(e_x) = H_v(e_x) + \sigma(e_x) \quad (74)$$

$\sigma(e_x)$ is the integral variables vector.

H_v is proposed on the basis of the Hamiltonian function given as:

$$\left. \begin{aligned} H &= H_m + H_e \\ H_m &= \frac{1}{2J_m} [J_m(\Omega_m - \Omega_m^*)]^2 \\ H_e &= \frac{1}{2} (\varphi_s - \varphi_s^*)^T A_{\varphi_s} (\varphi_s - \varphi_s^*) \end{aligned} \right\} \quad (75)$$

The performance of the proposed control scheme was validated by comparing with PI and the passive controller and by using four types of perturbations, which include parameter, mechanical torque, interconnection voltage, and short circuit variations. The power factor stabilizes after 2 s of perturbation with no overshoot. The passivity approach was also implemented in [174] for PMSG-based WECS. The authors construct the storage function to achieve MPPT, which is the combination of the resistance produced by the resistor heat produced by the d-axis current, shaft system kinetic energy, and torque energy. The energy function constructed is given as follows:

$$H(i_d, \Omega_m, T_e, T_m) = \underbrace{\frac{1}{2} (i_d - i_d^*)^2}_{\text{resistor heat}} + \underbrace{\frac{1}{2} (\Omega_m - \Omega_m^*)^2}_{\text{kinetic energy}} + \underbrace{\frac{1}{2} \left(\frac{T_m - T_e}{J_{\text{tot}}} - \Omega_m^* \right)^2}_{\text{accelerating torque energy}} \quad (76)$$

The derivative of this function is taken and, considering SMC theory, the passivity-based SMC is designed.

To further increase the robustness of the system, the authors in [184] propose an artificial neural network (ANN)-based SMC in which a torque compensation term is fed forward. The input to the ANN network is chosen to be the error between the actual and optimum speed. The SMC with ANN has a lower speed error of 0.67 rad/s and lower maximum power tracking error of 120 W compared to the PI controller with a speed error of 1.2 rad/s and max power tracking error of 145 W. The passivity and AI-based SMC schemes reviewed in the literature are given in Table 7. The overall SMC-based passive control system improves the system robustness and stability under stochastic wind speed variations, varying pitch angles, and generator parametric uncertainties.

7. Fractional-Order Sliding Mode Control Schemes

Fractional-order control theory has vast emerging applications in engineering, biosciences, and medical sciences [185,186], with a greater degree of freedom for integer-order systems [187]. SMC has excellent performance characteristics, such as a fast response, high robustness against external disturbances, and computational simplicity, making it a viable solution for a wide range of linear and nonlinear systems [77,188–191]. Because conventional design methodologies consider linear sliding surfaces, finite-time convergence of system states to equilibrium may fail [189]. As a result, the reaching gains should be chosen to be large enough when the SMC surface is close to equilibrium. In order to fill this void, TSMC approaches have been developed [192,193]. To ensure the system

dynamics' finite-time convergence, TSMCs incorporate nonlinear functions into the SMC surface. Although TSMC has a faster finite-time convergence and higher control precision than conventional SMC, it has two major drawbacks [194]: (a) the singularity problem, which causes unbounded large control inputs and has been well addressed by nonsingular TSMC (NTSMC) modifications [195,196], and (b) the chattering phenomenon, which is caused by high-frequency control switching. Fractional-order (FO) calculus has recently demonstrated a promising performance in improving conventional control approaches and has been widely applied in many research areas [197–200]. To address the second disadvantage, various combinations of SMC methods and FO calculus have been proposed in the literature [201–203]. When compared to traditional SMC and TSMC approaches, the integration of FO calculus with SMC provides more degrees of freedom by introducing more design parameters into the system. The FO calculus adds a memory to the controller [198], allowing it to consider the entire history of input signals, effectively reducing chattering and tracking errors in conventional SMC [203,204]. The authors in [186,205] give insight into the fractional-order integrals and differentiation. A stability analysis was performed in [206], whereas the fractional-order Lyapunov theorem was derived for fractional-order controllers in [207–214]. The primary fractional calculus operator is defined as follows:

$${}_a D_t^\alpha \cong \begin{cases} \frac{d^\alpha}{dt^\alpha}, & R(\alpha) > 0 \\ 1, & R(\alpha) = 0 \\ \int_\alpha^t (d\tau)^{-\alpha}, & R(\alpha) < 0 \end{cases} \quad (77)$$

A primary fractional operator has three definitions, namely, α th-order Riemann–Liouville fractional, α th-order Caputo fractional derivative, and α th-order Grunwald–Letnikov, and are given as follows:

$${}_a D_t^\alpha f(t) = \left. \begin{aligned} &= \frac{d^\alpha}{dt^\alpha} f(t) \\ &= \frac{1d^m}{\Gamma(m-\alpha)dt^m} \int_\alpha^t \frac{f(\tau)}{(t-\tau)^{1-\alpha}} d\tau {}_a D_t^{-\alpha} f(t) \\ &= I^\alpha f(t) \\ &= \frac{1}{\Gamma(\alpha)} \int_\alpha^t \frac{f(\tau)}{(t-\tau)^{1-\alpha}} d\tau \end{aligned} \right\} \quad (78)$$

$${}_a D_t^\alpha \cong D^\alpha = \begin{cases} \frac{1d^m}{\Gamma(n-\alpha)} \int_\alpha^t \frac{f^n(\tau)}{(t-\tau)^{\alpha-n+1}} d\tau \\ (n-1 \leq \alpha < n) \\ \frac{d^m}{dt^m} f(t) (\alpha = n) \end{cases} \quad (79)$$

$$\left. \begin{aligned} {}_a^{GL} D_t^\alpha f(t) &= \lim_{h \rightarrow 0} \frac{1}{h^\alpha} \sum_{j=0}^{[(t-\alpha)/h]} (-1)^j \binom{\alpha}{j} f(t-jh) \\ \binom{\alpha}{j} &= \frac{\Gamma(\alpha+1)}{\Gamma(j+1)\Gamma(\alpha-j+1)} \end{aligned} \right\} \quad (80)$$

where m is the smallest integer number and its value is greater than α . The given subsections will provide mathematical insight into the various FOSMC schemes presented in the literature. The main schemes evident in the literature and presented here are FOSMC schemes, FOTSMC, FO-STSMC, and fuzzy-FOSMC schemes.

Table 7. Passivity-based SMC comparison in WECS.

Technique	Ref.	Year	Errors	Surfaces	Generator, Control, and Converter-Type Hardware	Remarks
Passivity-based SMC	[215]	2021	$e_x = x - x_{ss}$ where $x = [J \ \Omega_r \ \phi_s]$, x_{ss} = stationary value of x	$s(e_x) = H_v(e_x) + \sigma(e_x)$, where $s(e_x) = [s_1(e_x) s_2(e_x)]^T$, $H_v(e_x) = [H(e_x)H(e_x)]^T$ and $\sigma(e_x) = [\sigma_1(e_x) \ \sigma_2(e_x)]^T$, the $H_v(e_x)$ is the energy function obtained using energy-based model of DFIG.	Brushless DFIG RSC control No	An energy or passivity-based SMC is presented in this paper. Energy-based model of brushless DFIG is also presented, and practical implementation issues are also depicted in the article.
	[216]	2018	$e_x = x - x_{ss}$ where $x = [i_d, \omega_m, T_e, T_m]$	$S(i_d, \omega_m, T_e, T_m) = \underbrace{\frac{1}{2}(i_d - i_d^*)^2}_{\text{resistor heat}} + \underbrace{\frac{1}{2}(\omega_m - \omega_m^*)^2}_{\text{kinetic energy}} + \underbrace{\frac{1}{2}\left(\frac{T_m - T_e}{J_{\text{tot}}} - \dot{\omega}_m^*\right)}_{\text{accelerating torque energy}}$	Multipole SG Yes	A passivity-based SMC is presented in this paper. Extensive analysis was conducted in this paper to evaluate the passivity-based SMC performance.
AI-based SMC	[184]	2014	$e_\Omega = \Omega_{ref} - \Omega_r$	$S_\Omega = \Omega_{ref} - \Omega_r$	IG RSC control No	Feed forward ANN is used to estimate the sigmoid function in the discontinuous control part of SMC.
	[217]	2018	$e_i = X_{rdq} - I_{rdq-ref}$	$S_i = X_{rdq} - I_{rdq-ref}$ where X_{rdq} are the states estimated using high-order neural network trained by extended Kalman filter	DFIG RSC control No	A neural network of high order is used and trained online using extended Kalman filter. The estimated states are then used to proposed a SMC scheme.

7.1. Fractional-Order Sliding Mode Control Design

In this control scheme, the reference signals have been generated using the control law driven by fractional-order surfaces. The authors in [102] utilize the error between the reference speed and actual speed to generate the reference torque. The electromagnetic torque in the outer loop generated by FOSMC is compared with the PI control scheme and shows a superior performance in terms of tracking under uncertainties. Similarly, the dq current error is used to propose a sliding surface. The sliding surface proposed by [107] is given as:

$$S = e + cD^{-\alpha}e; \quad (81)$$

The proposed control system is made adaptive by estimating the lumped uncertainty using a low pass filter with unity steady state gain. The control law consists of an equivalent part with non-linear known terms, $D^{1-\alpha}e$, and a robust term. Similarly, the authors in [218] use the same fractional-order control theory but use direct power control for speed and power tracking. The authors use varying parameters to choose the fractional-order for the precise tracking and chattering level. The disturbance comprising 10% of fifth-order and 8 % of seventh-order harmonics is efficiently tackled with less chattering compared to integer-order SMC. The active and reactive power errors are used to propose the surface given as $S = cD^{-\alpha}e$, which generates the required voltage signals for the PWM block.

The same idea has been extended in order to solve the sub-synchronous oscillation phenomenon caused by the DFIG system in multi terminal DC systems in [219]. The switching surface is selected on the basis of the dq current error. The sub-synchronous damping controller is also employed with the FOSMC current controller, which comprises a filter, amplitude gain segment, phase compensation, and proportion link. Thus, the overall control scheme provides a faster convergence rate of 0.4 s at 7.5 m/s under sub-synchronous oscillation variation compared to a conventional damper. Extending the idea of FOSMC, the authors in [103] proposed a FOSMC scheme for enhancing the output power quality. A surface is selected as:

$$S = e + \lambda D^{\alpha-1} \text{sign}(e)^\gamma \quad (82)$$

The controller coefficient selection problem is solved here by using the Luapunov theorem, where the optimization is used to select optimum parameters. The direct current control typology is employed, where the reference current is generated using an MPPT strategy. The FOSMC shows a superior performance compared to SMC and PI control schemes using simulation and experimental results. Moreover, the FOSMC shows fewer harmonics and a faster steady state convergence with chattering elimination and parameter tuning in [218]. The generic operational diagram of FOSMC controller is given in Figure 10, and the techniques reviewed are presented in Table 8, whereas the mathematical derivation of the FOSMC-based current control scheme is given below.

A surface is proposed using the fractional-order calculus presented as:

$$\left. \begin{aligned} S_\Omega &= e_\Omega + c_3 D^{-\alpha} e_\Omega \\ \dot{S}_\Omega &= \dot{e}_\Omega + c_3 D^{1-\alpha} e_\Omega \end{aligned} \right\} \quad (83)$$

Equation (83) can be further simplified by using the $D^{-\alpha}$ operator on both sides and then putting the value of \dot{e}_Ω as follows:

$$\dot{S}_\Omega = \frac{T_{em}}{J} + d_3 - \dot{\Omega}_{r-ref} + c_3 D^{1-\alpha} e_\Omega \quad (84)$$

Equation (84) is used to derive the equivalent control law T_{em-eq} , and the T_{em-s} (switching control part) is designed using the SM theory given below as:

$$T_u = J \left(d_3 - \dot{\Omega}_{r-ref} + c_5 D^{1-\alpha} - k_3 \text{sign}(S_\Omega) \right) \quad (85)$$

A new sliding surface presented using the fractional-order calculus is presented as:

$$\left. \begin{aligned} S_1 &= e_1 + c_1 D^{-\alpha} e_1 \implies \dot{S}_1 = \dot{e}_1 + c_1 D^{1-\alpha} e_1 \\ S_2 &= e_2 + c_2 D^{-\alpha} e_2 \implies \dot{S}_2 = \dot{e}_2 + c_2 D^{1-\alpha} e_2 \end{aligned} \right\} \quad (86)$$

Using the surface derivative given in (86) and following the SMC control law methodology, the RSC current control is obtained as follows:

$$u = h^{-1} \left[\begin{aligned} &\frac{R_r}{\sigma L_r} I_{dr} - s\omega_s I_{qr} + \dot{I}_{dr-ref} - c_1 D^{1-\alpha} e_1 - k_1 \text{sign}(S_1) \\ &\frac{R_r}{\sigma L_r} I_{qr} + s\omega_s I_{dr} + s \frac{MV_s}{\sigma L_r L_s} + \dot{I}_{qr-ref} - c_3 D^{1-\alpha} e_2 - k_2 \text{sign}(S_2) \end{aligned} \right] \quad (87)$$

By defining a fractional-order surface S_E and its derivative \dot{S}_E , we have:

$$S_E = c_7 D^{-\alpha} e_E + c_8 D^\alpha |e_E|^\gamma \text{sign}(e_E) \quad (88)$$

$$\dot{S}_E = c_7 D^{1-\alpha} e_E + c_8 \gamma D^\alpha |e_E|^{\gamma-1} \dot{e}_E \quad (89)$$

Applying fractional operator $D^{-\alpha}$ to (89), we have:

$$D^{1-\alpha} S_E = c_7 D^{1-2\alpha} e_E + c_8 \gamma |e_E|^{\gamma-1} \dot{e}_E \quad (90)$$

Putting the value of \dot{e}_E from (34) in (90), we obtain:

$$\left. \begin{aligned} D^{\bar{\alpha}} S_E &= c_7 D^{1-2\alpha} e_E + c_8 \gamma (|e_E|^{\gamma-1} g_0(x) I_d - \frac{|e_E|^{\gamma-1}}{C} I_{or} + |e_E|^{\gamma-1} dE - |e_E|^{\gamma-1} \dot{E}_{ref}) \\ \text{where } D^{1-\alpha} &= D^{\bar{\alpha}} \end{aligned} \right\} \quad (91)$$

Equation (91) is used to derive the equivalent control law I_{d-eq} , while the discontinuous control component I_{d-s} is designed based on fuzzy control theory and is given as follows:

$$\left. \begin{aligned} I_{d-eq} &= \frac{1}{g_0(x)} |e_E|^{1-\gamma} \left[\frac{|e_E|^{\gamma-1}}{C} I_{or} - |e_E|^{\gamma-1} \dot{E}_{ref} - \frac{c_7}{c_8 \gamma} D^{1-2\alpha} e_E \right] \\ I_{d-s} &= -\frac{\lambda_E |e_E|^{1-\gamma}}{g_0(x) c_8 \gamma} k_4 \text{sign}(S_2) \end{aligned} \right\} \quad (92)$$

Thus, the complete control law, $I_d = I_{d-eq} + I_{d-s}$, is derived using (92). The FOSMC basic operational diagram is shown in Figure 10.

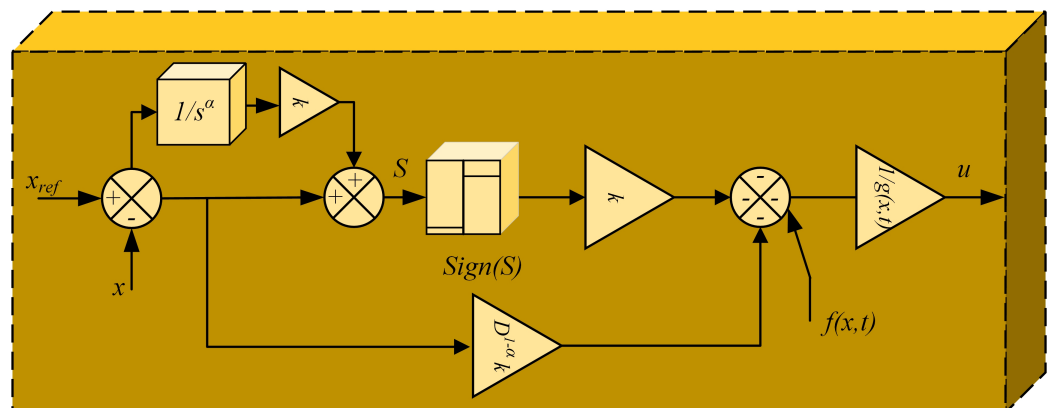


Figure 10. Fractional-order SMC operational diagram.

Table 8. Fractional-order control schemes and their variants comparison in WECS.

Technique	Ref	Year	Errors	Surfaces	Generator, Control, and Converter-Type Hardware	Remarks
Fractional SMC	[102]	2016	$e_{\Omega} = \Omega_{ref} - \Omega_r$ $e_i = I_{rdq} - I_{rdq-ref}$	$S_{e_{\omega}} = e_{e_{\omega}} + cD^{-\alpha}e_{e_{\omega}}$ $S_i = e_i + cD^{-\alpha}e_i$	DFIG RSC control No	An FOSMC is proposed to mitigate the inherent chattering in SMC without the knowledge of uncertainties boundaries.
	[218]	2017	$[e] = \begin{bmatrix} e_1 \\ e_2 \end{bmatrix} = \begin{bmatrix} P_{ref} - P_s \\ Q_{ref} - Q_s \end{bmatrix}$	$[S] = \begin{bmatrix} cD^{\alpha}sign(e_1) \\ cD^{\alpha}sign(e_2) \end{bmatrix}$	DFIG BTB converter RSC DPC Yes	An FOSMC with an enhanced exponential reaching law is proposed. The FOSMC is used to mitigate the inherent chattering in SMC.
	[219]	2020	$e_i = I_{rdq} - I_{rdq-ref}$	$S_i = e_i + c_5D^{\alpha}e_i$	DFIG RSC control connected to voltage-source-converter-based multi-terminal DC system No	A feedback linearization-based system is used to control the DFIG using FOSMC. The considered wind system is connected to a multi-terminal DC system.
	[103]	2020	$e_i = I_{sdq} - I_{sdq-ref}$ $e_i = I_{Edq} - I_{Edq-ref}$	$S_{sd} = e_{sd} + \lambda_{sd}D^{\alpha-1}(\text{sig}(e_{sd})^{\gamma_1})$ $S_{sq} = e_{sq} + \lambda_{sq}D^{\alpha-1}(\text{sig}(e_{sq})^{\gamma_2})$ $S_{Ed} = e_{Ed} + \lambda_{Ed}D^{\alpha-1}(\text{sig}(e_{Ed})^{\gamma_1})$ $S_{Eq} = e_{Eq} + \lambda_{Eq}D^{\alpha-1}(\text{sig}(e_{Eq})^{\gamma_2})$	PMSG BTB converters RSC and GSC Yes	FOSMC-based control is presented. A sign function is replace by saturation function.

7.2. Fractional-Order Terminal Sliding Mode Control Schemes

The advantages of FOSMC have been presented in the previous section. The finite time convergence capabilities of TSMC have been combined with FOSCM to achieve a fast, finite time convergence, and an enhanced performance with minimized chattering. The authors in [104] proposed an adaptive FOTSMC scheme for DFIG-based WECS. The new surface adapted is given below as:

$$S = c_5 D^{-\alpha} e + c_6 D^\alpha |e|^\gamma \text{sign}(e). \tag{93}$$

The new surface now follows the characteristics of FOSMC and TSMC schemes. The controller has also been made adaptive in order to estimate the disturbance and external perturbations, and the parameters have been selected using the optimization toolbox and integral absolute error as the performance index. The comparison of the results with SMC and PI showed that the FOTSMC showed a robust performance under normal and perturbed situations, with less chattering. Following the same pattern, the authors in [106] integrated the AI with an FOTSMC control scheme to propose a new controller for a more robust performance. The discontinuous parts of the controllers in [109] may increase the chattering due to the presence of $D^{1-\alpha}$; thus, it has been estimated and tuned by FLC theory and the performance has been validated by using PIL results. The reactive power oscillations were $\pm 0.01 \text{ kVAR}$ for SMC, whereas AI-based FOTSMC gives almost zero oscillations. The FOTSMC operational diagram is shown in Figure 11, whereas the techniques have been reviewed in Table 9. The further section will now present the mathematical formulation of FOTSMC proposed by [104]. Following the surface in (93), the derivative is given as:

$$\left. \begin{aligned} \dot{S}_\Omega &= c_5 D^{1-\alpha} e_\Omega + c_6 D^\alpha \underbrace{D^1 |e_\Omega|^\gamma \text{sgn}(e_\Omega)} \\ \dot{S}_\Omega &= c_5 D^{1-\alpha} e_\Omega + c_6 \gamma D^\alpha |e_\Omega|^{\gamma-1} e_\Omega \end{aligned} \right\} \tag{94}$$

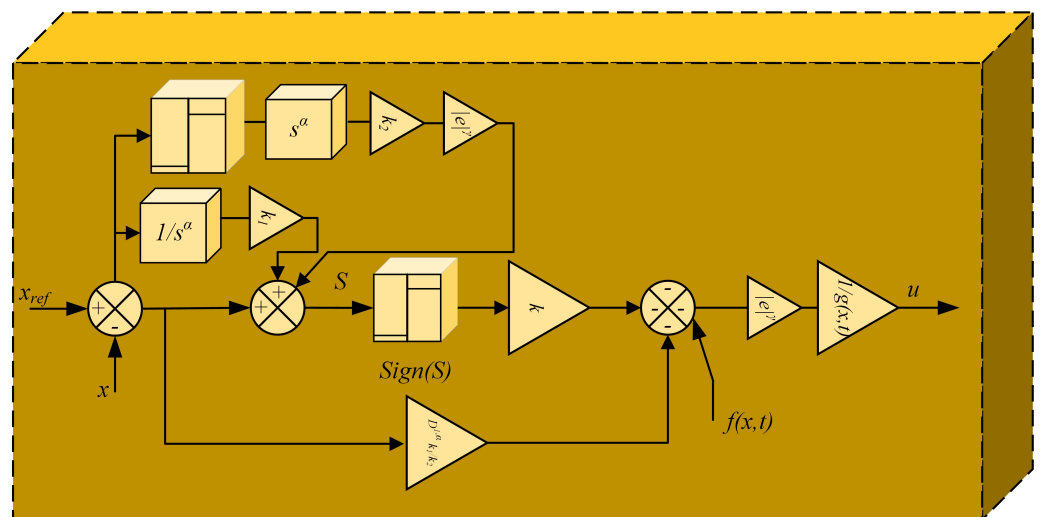


Figure 11. Fractional-order terminal SMC operational diagram.

Equation (94) can be further simplified by using the $D^{-\alpha}$ operator on both sides, and then putting the value of \dot{e}_Ω as follows:

$$D^{\bar{\alpha}}S_{\Omega} = c_5 D^{2-2\alpha} e_{\Omega} + c_6 \gamma \left(\frac{|e_{\Omega}|^{\gamma-1} T_{em}}{J} + |e_{\omega}|^{\gamma-1} d_3 - |e_{\Omega}|^{\gamma-1} \dot{\Omega}_{r-ref} \right) \quad (95)$$

where $D^{\bar{\alpha}} = D^{1-\alpha}$

The equivalent control law T_{em-eq} is derived from (95), whereas the T_{em-s} (switching control part) is given below as:

$$\left. \begin{aligned} T_u &= T_{em-eq} + T_{em-sw} \\ T_{em-eq} &= J|e_{\Omega}|^{1-\gamma} \left[\frac{|e_{\Omega}|^{\gamma-1} \dot{\Omega}_{r-ref}}{c_6 \gamma} - \frac{c_5}{c_6 \gamma} D^{1-2\alpha} e_{\Omega} \right] \\ T_{em-s} &= J|e_{\Omega}|^{1-\gamma} \left(-\frac{\lambda_{\omega}}{c_6 \gamma} \text{sign}(S_{\Omega}) \right) \end{aligned} \right\} \quad (96)$$

The sliding surface for the current control loop using the fractional-order calculus is presented as:

$$\left. \begin{aligned} S_1 &= c_1 D^{-\alpha} e_1 + c_2 D^{\alpha} |e_1|^{\gamma} \text{sign}(e_1) \\ S_2 &= c_3 D^{-\alpha} e_2 + c_4 D^{\alpha} |e_2|^{\gamma} \text{sign}(e_2) \end{aligned} \right\} \quad (97)$$

The equivalent control laws $[V_{d-eq} \quad V_{q-eq}]$ are derived using the same process for the speed control, and the switching control components $[V_{d-s} \quad V_{q-s}]$ are designed based on a SMC theory and are given below as:

$$\left. \begin{aligned} V_{d-eq} &= \sigma L_r \left[-G_1 + \frac{1}{\sigma L_r} R_r I_{dr} - \frac{c_1 |e_1|^{1-\gamma} D^{1-2\alpha}}{c_2 \gamma} e_1 \right] \\ V_{d-s} &= -\frac{\lambda_d |e_1|^{1-\gamma}}{c_2 \gamma} \text{sign}(S_1) \\ V_{q-eq} &= \sigma L_r \left[-G_2 + \frac{1}{\sigma L_r} R_r I_{qr} - \frac{c_3 |e_2|^{1-\gamma} D^{1-2\alpha}}{c_4 \gamma} e_2 \right] \\ V_{d-s} &= -\frac{\lambda_q |e_2|^{1-\gamma}}{c_4 \gamma} \text{sign}(S_2) \end{aligned} \right\} \quad (98)$$

The equivalent terms $[V_{d-eq} \quad V_{q-eq}]$ and switching terms $[V_{d-s} \quad V_{q-s}]$ combine to formulate the complete current control law u . By defining a fractional-order surface S_E and its derivative \dot{S}_E , we have:

$$S_E = c_7 D^{-\alpha} e_E + c_8 D^{\alpha} |e_E|^{\gamma} \text{sign}(e_E) \quad (99)$$

Similarly, the control law for grid side is given below as:

$$\left. \begin{aligned} I_{d-eq} &= \frac{1}{g_0(x)} |e_E|^{1-\gamma} \left[\frac{|e_E|^{\gamma-1}}{C} I_{or} - |e_E|^{\gamma-1} \dot{E}_{ref} - \frac{c_7}{c_8 \gamma} D^{1-2\alpha} e_E \right] \\ I_{d-f} &= -\frac{\lambda_E |e_E|^{1-\gamma}}{g_0(x) c_8 \gamma} \text{sign}(S_E) \end{aligned} \right\} \quad (100)$$

Thus, the complete control law $I_d = I_{d-eq} + I_{d-f}$ is derived using (100). The operating diagram of FOTSMC is shown in Figure 11.

7.3. Fractional-Order Super Twisting Sliding Mode Control Schemes

The FOSMC eliminates the chattering by minimizing the decaying time during the sliding motion. This enhanced performance is achieved by implementing fractional-order calculus applications during the sliding motion. However, it has been mentioned in [105] that the chattering in FOSMC can be further minimized by using the HOSMC scheme in the

discontinuous control part. The authors in [105] combine the attributes of the super twisting control structure and fractional-order control theory. The author improves the FTSMC performance by using the equivalent terms in (89), (93), (91), and the super-twisting-based switching control law given in Section 5.2. The operational diagram of FOTSMC is shown in Figure 12 and the reviewed techniques are presented in Table 9. The speed control is given as follows:

$$\left. \begin{aligned} T_u &= T_{em-eq} + T_{em-sw} \\ T_{em-eq} &= J|e_\Omega|^{1-\gamma} \left[\frac{|e_\Omega|^{\gamma-1} \hat{\Omega}_{r-ref}}{c_6\gamma} - \frac{c_5}{c_6\gamma} D^{1-2a} e_\Omega \right] \\ T_{em-sw} &= J|e_\Omega|^{1-\gamma} \left[-\frac{\lambda\omega_3}{c_6\gamma} |S_\Omega|^{\frac{1}{2}} \text{sign}(S_\Omega) - \frac{\beta\omega_3|e_\Omega|^{1-\gamma}}{c_4\gamma} \int \text{sign}(S_2) \right] \end{aligned} \right\} \quad (101)$$

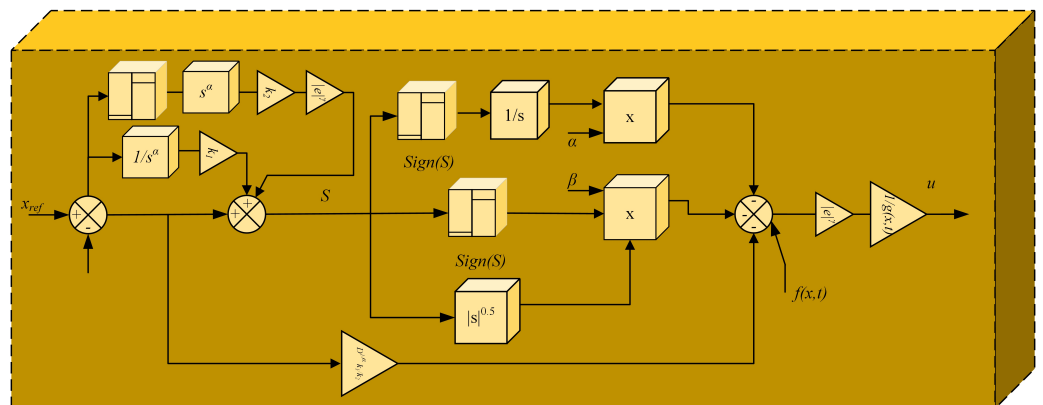


Figure 12. Fractional-order super twisting SMC operational diagram.

The current control law for ST-FTSMC is given as follows:

$$\left. \begin{aligned} V_{dr-eq} &= \sigma L_r \left[-G_1 + \frac{1}{\sigma L_r} R_r I_{dr} - \frac{c_1 |e_1|^{1-\gamma} D^{1-2a} e_1}{c_2\gamma} \right] \\ V_{dr-sw} &= -\frac{\lambda\omega_1 |e_1|^{1-\gamma}}{c_2\gamma} |S_1|^{\frac{1}{2}} \text{sign}(S_1) - \frac{\beta\omega_1 |e_1|^{1-\gamma}}{c_2\gamma} \int \text{sign}(S_1) \\ V_{qr-eq} &= \sigma L_r \left[-G_2 + \frac{1}{\sigma L_r} R_r I_{qr} - \frac{c_3 |e_2|^{1-\gamma} D^{1-2a} e_2}{c_4\gamma} \right] \\ V_{dr-sw} &= -\frac{\lambda\omega_2 |e_2|^{1-\gamma}}{c_4\gamma} |S_2|^{\frac{1}{2}} \text{sign}(S_2) - \frac{\beta\omega_2 |e_2|^{1-\gamma}}{c_4\gamma} \int \text{sign}(S_2) \end{aligned} \right\} \quad (102)$$

For GSC control, the ST-FTSMC-based control law takes the following structure:

$$\left. \begin{aligned} I_{d-eq} &= \frac{1}{g_0(x)} |e_E|^{1-\gamma} \left[\frac{|e_E|^{\gamma-1}}{C} I_{or} - |e_E|^{\gamma-1} \dot{E}_{ref} - \frac{c_7}{c_8\gamma} D^{1-2a} e_E \right] \\ I_{d-sw} &= -\frac{\lambda\omega_4 |e_E|^{1-\gamma}}{g_0(x)c_8\gamma} |S_E|^{\frac{1}{2}} \text{sign}(S_E) - \frac{B\omega_4 |e_E|^{1-\gamma}}{g_0(x)c_8\gamma} \int \text{sign}(S_E) \end{aligned} \right\} \quad (103)$$

Thus, the complete control law $I_d = I_{d-eq} + I_{d-f}$ is derived using (103). The operating diagram of FOTSMC is shown in Figure 12.

7.4. Fractional-Order Fuzzy Sliding Mode Control

The signum function in (96), (98), and (100) is the main cause of the chattering in the FOTSMC paradigm. The authors in [2] replace the $\text{sign}(S_\omega)$ by the saturation function to minimize the chattering; this is given as:

$$\text{sat}\left(\frac{S_\Omega}{\psi}\right) = \begin{cases} \frac{S_\Omega}{\psi}, & \text{if } |S_\Omega| \leq |\psi| \\ \text{sign}(S_\Omega), & \text{otherwise} \end{cases} \quad (104)$$

where ψ is defined as the thickness of the boundary layer. The utilization of the above function in place of $\text{sign}(S)$ can eliminate the chattering, but the performance may be degraded and not suitable under uncertain scenarios. Therefore, the function sat is replaced by a fuzzy system, which performs like a sat function with a nonlinear slope inside the thin boundary layer. The inputs to the fuzzy system are selected as the fractional-order surfaces $S = (S_\Omega, S_1, S_2, S_E)$ and alteration in the surface $\dot{S} = (\dot{S}_\Omega, \dot{S}_d, \dot{S}_q, \dot{S}_E)$ adopted in this paper for the DFIG control. The fuzzy system for the speed control loop can be represented as follows:

$$u_{f\Omega} = \text{Fuzzy} - \text{FOSMC}(S_\Omega, \dot{S}_\Omega) \quad (105)$$

where fuzzy–FOSMC is the system developed on the basis of fuzzy control theory using the membership function given in Figure 13. Hence, a new fuzzy-based reaching law can be presented as:

$$T_{em-f} = J|e_\Omega|^{1-\gamma} \left(-\frac{\lambda_\omega}{c_6\gamma} u_{f\Omega} \right) \quad (106)$$

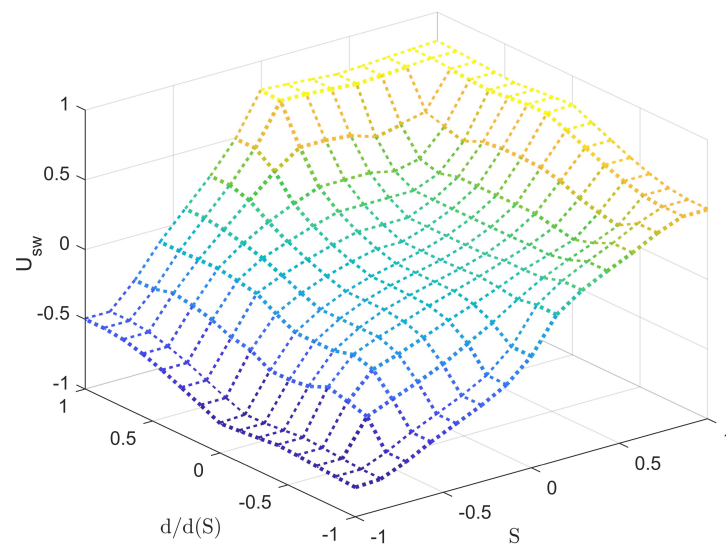
The u_{fq} and u_{fd} are the approximated signum functions using fuzzy theory. The rules map is shown in Figure 13a. Membership functions presented in Figure 13b,c are used to calculate u_{fq} and u_{fd} and are given as follows:

$$\left. \begin{aligned} u_{fd} &= \text{Fuzzy} - \text{FOSMC}(S_1, \dot{S}_1) \\ u_{fq} &= \text{Fuzzy} - \text{FOSMC}(S_2, \dot{S}_2) \end{aligned} \right\} \quad (107)$$

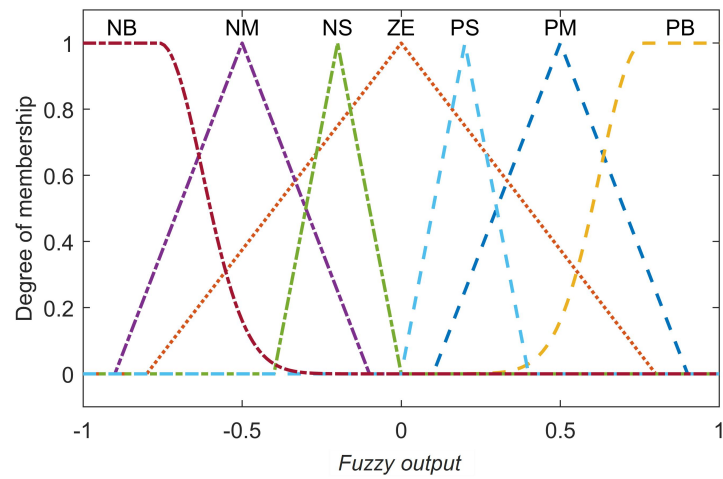
The u_{fE} is the approximated signum functions using fuzzy theory. Membership functions presented in Figure 13 are used to calculate u_{fE} and are given as follows:

$$u_{fE} = \text{Fuzzy} - \text{FOSMC}(S_E, \dot{S}_E) \quad (108)$$

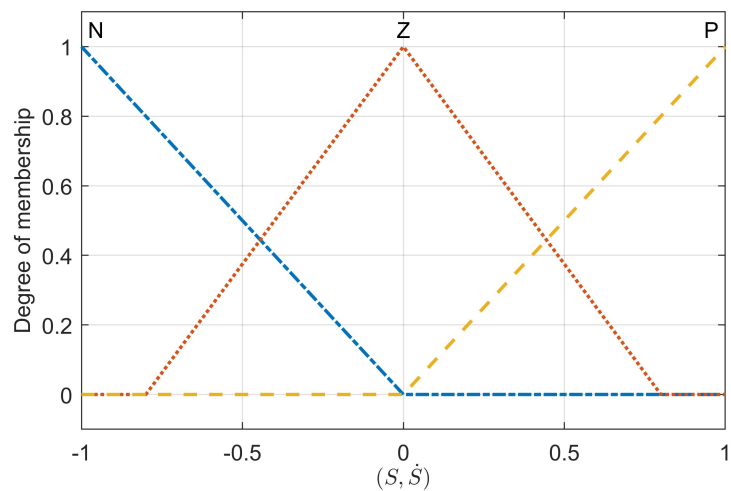
Hence, using the above given structures, the control law given in Section 7.2 receives the attributes of fuzzy control theory to remove the chattering in the sliding phase. The same concept can also be applied for other variants of SMC to improve the performance.



(a)



(b)



(c)

Figure 13. Membership function of fuzzy logic control–based FOSMC scheme. Reprinted with permission from Ref. [2]. Copyright 2021 Elsevier.

Table 9. Fractional-order terminal and Fractional-order supertwisting SMC control schemes.

Technique	Ref	Year	Errors	Surfaces	Generator, Control, and Converter-Type Hardware	Remarks
Fractional-order terminal SMC	[104]	2017	$e_{\Omega} = \Omega_{ref} - \Omega_r$ $e_i = I_{rdq} - I_{rdq-ref}$ $e_E = E^* - E$	$S_{\Omega} = e_{\Omega} + c_5 D^{-\alpha} e_{\Omega}$ $S_i = e_i + c_5 D^{-\alpha} e_i$ $S_E = e_E + c_5 D^{-\alpha} e_E$	DFIG BTB converters Yes	An artificial intelligence and fractional-order system are integrated to improve the system efficiency. The discontinuous terms of controllers are proposed using FL theory. The experiments are validated using PIL-based workbench.
	[106]	2020	$e_{\Omega} = \Omega_{ref} - \Omega_r$ $e_i = I_{rdq} - I_{rdq-ref}$ $e_E = E^* - E$	$S_{\Omega} = c_1 D^{-\alpha} e_{\Omega} + c_2 \int e_{\Omega}$ $S_i = c_{3,5} D^{-\alpha} e_i + c_{4,6} \int e_i$ $S_E = c_7 D^{-\alpha} e_E + c_8 \int e_E$	DFIG BTB converters Yes	
Fractional-order super twisting	[105]	2017	$e_{\Omega} = \Omega_{ref} - \Omega_r$ $e_i = I_{rdq} - I_{rdq-ref}$ $e_E = E^* - E$	$S_{\omega} = e_{\Omega} + c_5 D^{-\alpha} e_{\Omega}$ $S_i = e_i + c_5 D^{-\alpha} e_i$ $S_E = e_E + c_5 D^{-\alpha} e_E$	DFIG BTB converters Yes	A fractional-order terminal control is combined with the attributes of super twisting control. The chattering in fractional-order terminal SMC is improved by using super twisting algorithm
Fractional-order composite SMC	[2]	2020	$e_{\Omega} = \Omega_{ref} - \Omega_r$ $e_i = I_{rdq} - I_{rdq-ref}$ $e_E = E^* - E$	$S_{\Omega} = e_{\Omega} + c_5 D^{-\alpha} e_{\Omega}$ $S_i = e_i + c_5 D^{-\alpha} e_i$ $S_E = e_E + c_5 D^{-\alpha} e_E$	DFIG BTB converters Yes	A sensorless FOTSMC is presented in this paper. The speed is estimated using Gaussian process regression. The sign function is replaced by fuzzy control theory to reduce chattering.

8. Comparative Analysis of Integer and Fractional-Order SMC Schemes

The various typologies are made operational using various control levels. The optimal operation of grid-connected typologies is performed in four levels of centralized control, which are: (1) power converter control, (2) generator and grid control, (3) grid integration and MPPT control, and (4) wind turbine centralized control. Level 4 consists of both electrical and mechanical control. The mechanical control includes damping control, whereas the electrical control includes the reactive power generation (RPG) and fault ride-through (FRT). The tower mechanical resonance in the drive train, electrical resonance in the grid, and torsional vibrations in the drive train are minimized by the electrically and mechanically managed damping control part. Ancillary services, such as spinning reserve, kinetic energy storage, and inertia emulation, are also provided in control level 4 using electrical and mechanical control. The MPPT and grid synchronization is performed in control loop 3. The phase-locked loop (PLL), zero-crossing detection, and grid voltage filtering are used to synchronize the WECS with the grid. The outputs and inputs to the control level 3 are given in Figure 14, where the reference dc-link voltage or grid voltage magnitude is kept constant. The SMC and its enhanced techniques are implemented in level 2 and level 1 using the various mathematical control laws derived in this paper. The FOSMC and IOSMC schemes are compared in the literature using mathematical and numerical analysis. This section will initially provide a mathematical comparison of IOSMC and FOSMC schemes and SMC variants proposed in the literature. This section will also compare the FOSMC and IOSMC schemes for DFIG speed, power, DC link voltage, errors, and sliding surfaces.

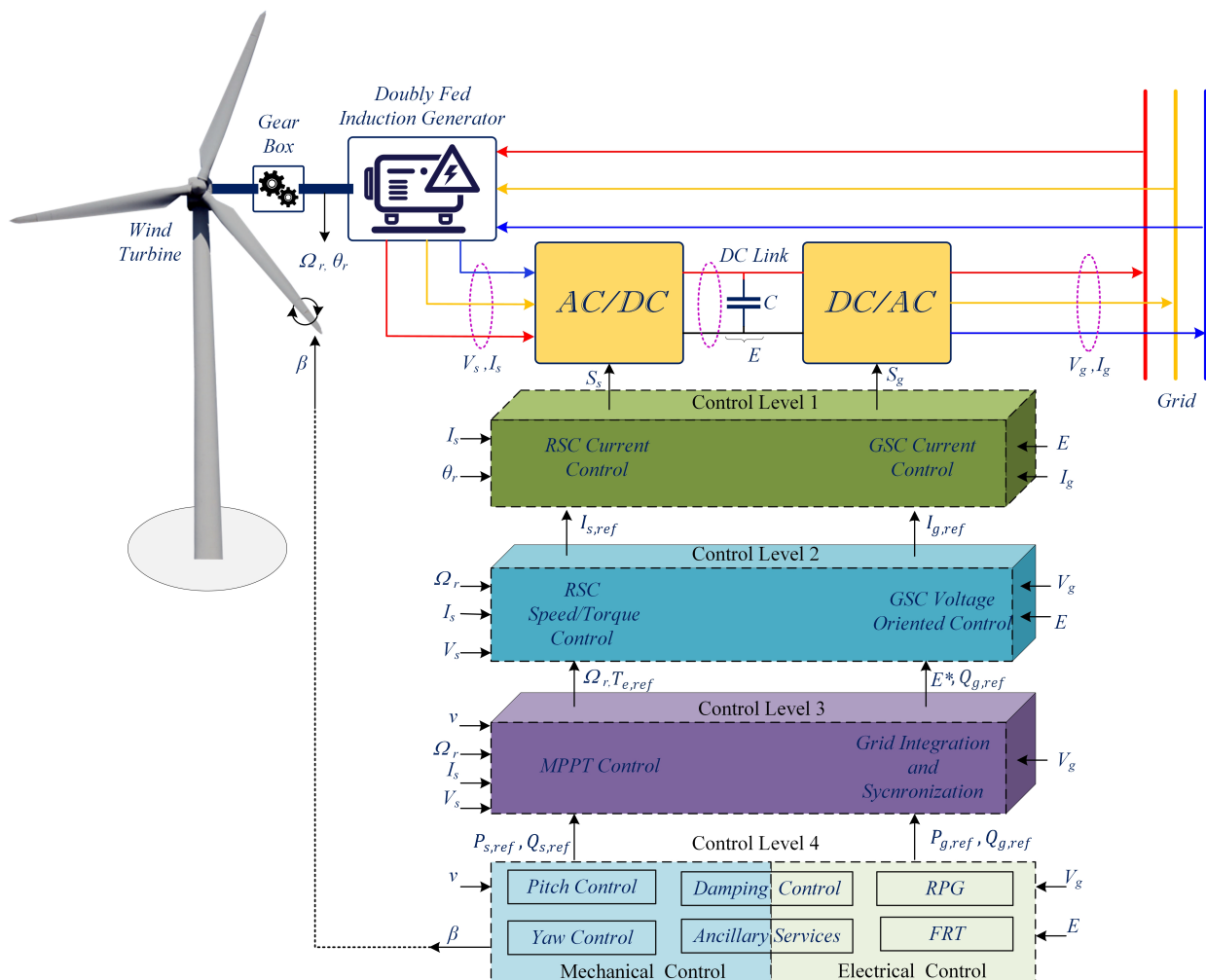


Figure 14. Schematic of DFIG-based WECS operating under different levels.

8.1. Mathematical Comparison

This section presents the FOTSMC scheme advantages over integer-order SMC (IOSMC) schemes in terms of stability. The IOSMC and FOTSMC system satisfies the following conditions at the occurrence of sliding motion [220]:

$$D_t^\alpha f(t) = Gx(t) \quad \forall (0 < \alpha \leq 1), G \in R^- \tag{109}$$

The above equation solution can be given as follows:

$$f(t) = X_{\alpha,1}(t)f_0 \tag{110}$$

where $X_{\alpha,\beta}(t) = \sum_{k=0}^{\infty} (G^k t^{\alpha k} / \Gamma(\alpha k + \beta))$ ($0 < \alpha \leq 1$) is the states transfer function, and $\Gamma(z)$ is the gamma function. For an integer-order system with $r = 1$, the state transfer function is given as follows:

$$E_{\alpha,\beta}(t) = X_{1,1}(t) = \sum_{k=0}^{\infty} \frac{G^k t^k}{\Gamma(k+1)} = \sum_{k=0}^{\infty} \frac{G^k t^k}{k!} = \exp(Gt) \tag{111}$$

The above result shows that the decay type of integer-order system towards 0 is exponential. For a fractional-order system, the state transfer function from Matignon is given as [220]:

$$X_{\alpha,1}(t) = \sum_{k=0}^{\infty} \frac{G^k t^{\alpha k}}{\Gamma(rk+1)} \approx \frac{1}{\Gamma(1-\alpha)} (G)^{-1} t^{-\alpha} \quad \forall (0 < \alpha < 1) \tag{112}$$

The fractional-order system decays like $t^{-\alpha}$ towards 0, depicting the slow energy transfer with FOTSMC surfaces. The delay time Δ defined as the time taken for control output to vary from $+u(x, y)$ to $-u(x, y)$ is the major reason for chattering. A system reaching from initial state (x_0, y_0) to sliding surface $S(x, y) = 0$ is shown in Figure 15. According to the decaying time proof in Equation (111), the Figure 15 shows the behavior of the integer-order system decaying with e^{-t} taking a total time of t_i , as shown by the red line. On the other side, the fractional-order system decaying time is $t^{-\alpha}$, as proven in (112), and takes a total time of t_f , as shown through the blue line. Thus, for the same plant, $e^{-t_i} > t_f^{-\alpha}$ [220].

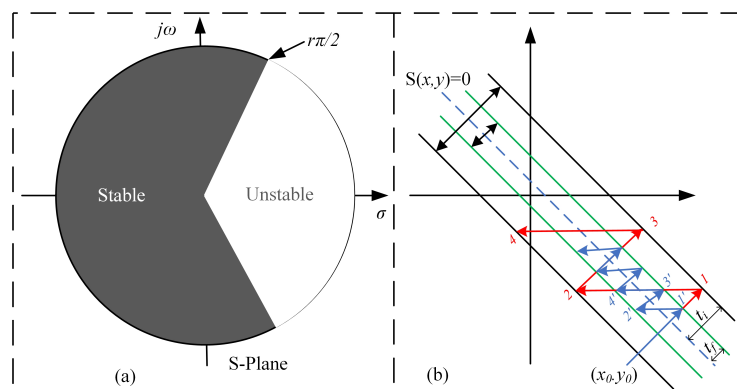


Figure 15. (a,b) Stable domain of fractional-order system. Reprinted with permission from Ref. [220]. Copyright 2012 Elsevier.

8.2. Case Study: Implementation and Numerical Comparison

This section presents a comparative analysis of the IOSMC, FOTSMC, and composite FOSMC control schemes presented in the literature. The detailed operational diagram of FOTSMC presented in Section 7.2 is shown in Figure 16. The authors in [2,105] provided

several SMC schemes and their variants. The resulting speed waveform and active and reactive power for SMC, FOTSMC, and fuzzy FOSMC are compared in Figure 17. Figure 17a shows that the controllers provided an accurate speed tracking, with SMC providing severe chattering. An FOTSMC-based controller was developed to minimize the chattering in the conventional SMC. The results depict that the FOTSMC minimized the chattering in the SMC scheme to a certain extent. To further improve the SMC and FOTSMC performance, the author in [2] proposed a fuzzy-FOSMC scheme. The results in Figure 17 show that the proposed fuzzy-FOSMC further improved the performance of DFIG-WECS by minimizing the chattering effect in SMC and FOTSMC. The error and surfaces waveforms in Figure 18 also show that the fuzzy-FOSMC provided an improved performance compared to the SMC and FOTSMC. A computational comparison was evaluated in this paper using PIL-based simulation, which consists of a dual core processor TMS320F379D programmed using a rapid prototyping method from a Simulink environment. The Simulink files are compiled in the discrete domain and the hex file is programmed into the random access memory (RAM) of the processor. It can be seen from Figure 19 that the fractional SMC has more CPU utilization compared to the integer-order SMC. The average CPU utilization for fraction SMC is 29.13%, whereas, for SMC, the average CPU utilization is 18.81%. Similarly, the average execution time of fractional SMC is also higher than the integer-order SMC as shown in Figure 19.

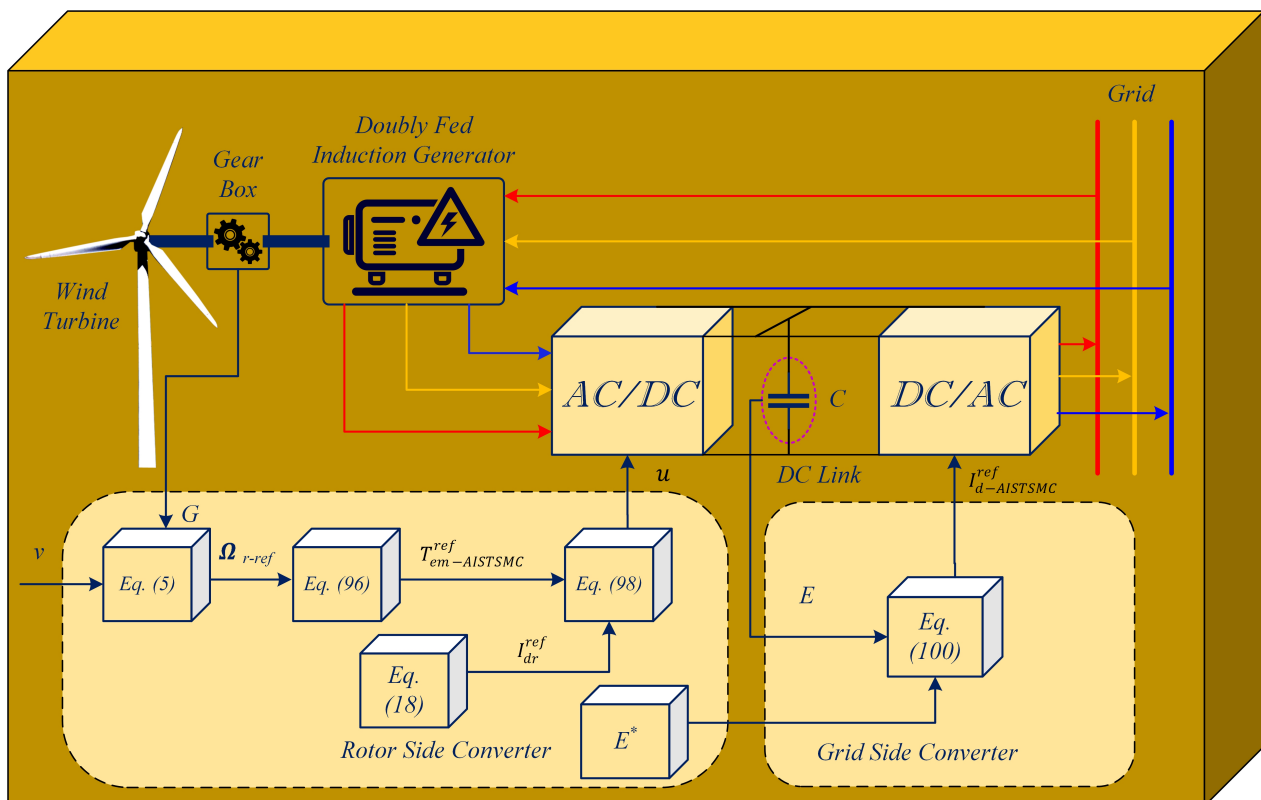
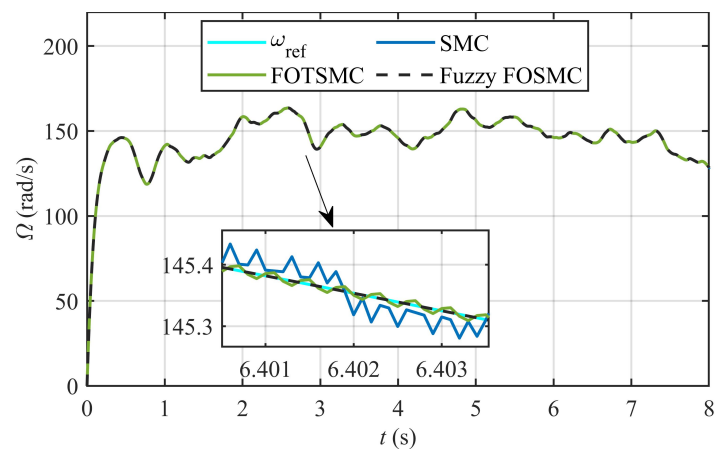
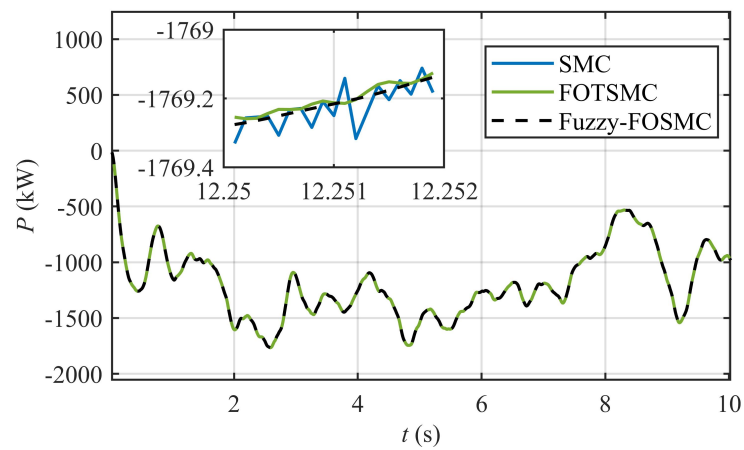


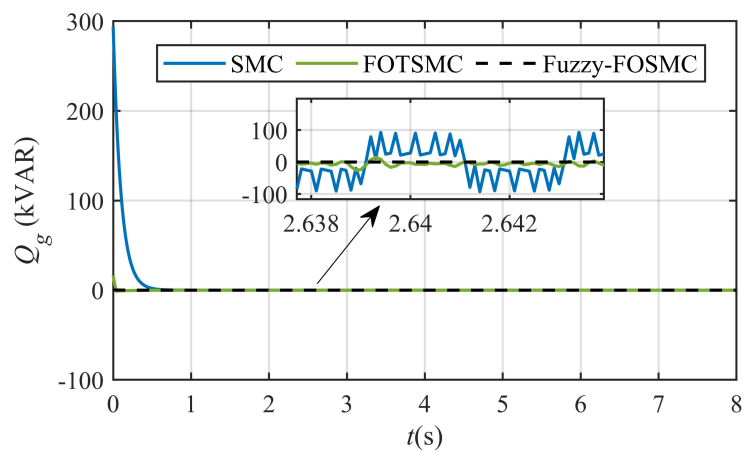
Figure 16. Schematic of DFIG-based WECS operating under FOTSMC. Reprinted with permission from Ref. [2]. Copyright 2021 Elsevier.



(a) Generator speed

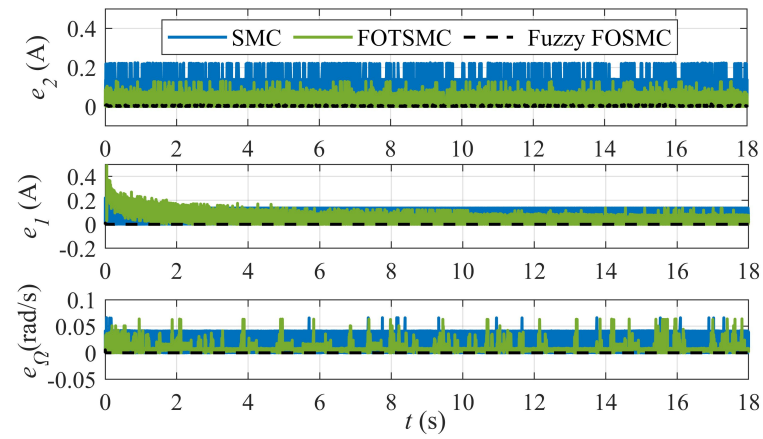


(b) Active power

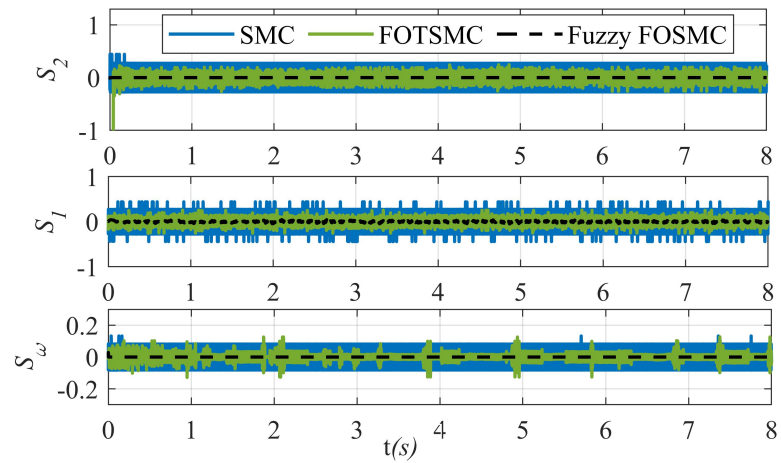


(c) Reactive power

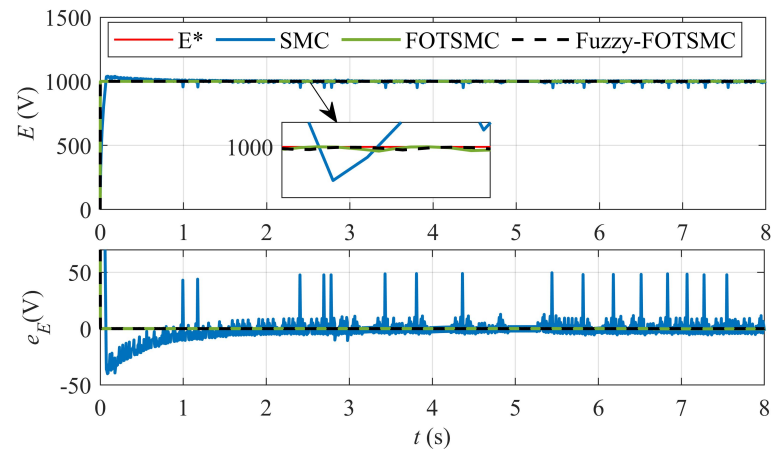
Figure 17. Generator speed, active, reactive power tracking. Reprinted with permission from Ref. [2]. Copyright 2021 Elsevier.



(a) Speed and current errors

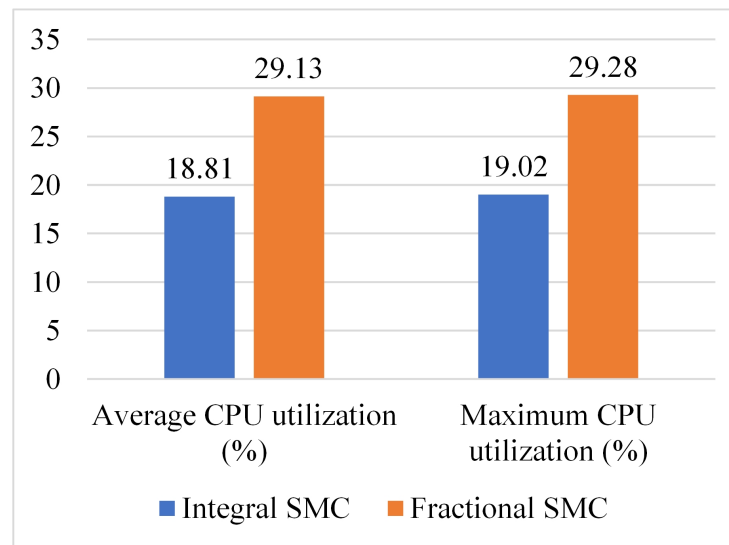


(b) Surfaces

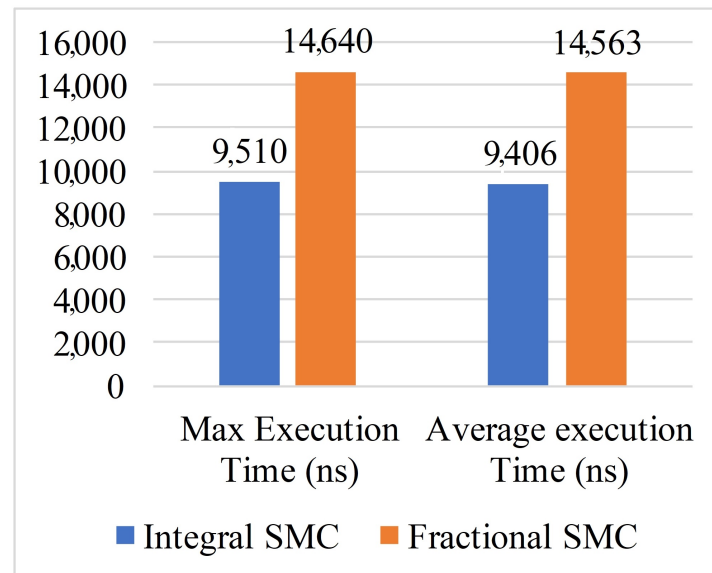


(c) DC link voltage and tracking error

Figure 18. Errors , surfaces, and DC-link voltage tracking. Reprinted with permission from Ref. [2]. Copyright 2021 Elsevier.



(a) Average and maximum CPU utilization



(b) Average and maximum execution time

Figure 19. CPU and execution times for IOSMC and FOSMC.

9. Conclusions

A comprehensive review of sliding mode control and its variants presented in the literature is presented in this paper. The main focus of this paper is to cover the various SMC techniques proposed and mathematically presented in the literature. The important factor in a wind energy conversion system is the mathematical modeling of various components. The mathematical model of the wind turbine, doubly fed induction generators, permanent magnet synchronous generators, and grid is presented. This study starts with the WECS overview and the control levels in a wind-energy-based grid system. The rotor side control (RSC) and grid side control (GSC) concept is used to assess the mathematical and operational aspects of grid-connected WECS. The SMC techniques are broadly classified into integer-order SMC (IOSMC) and fractional-order SMC (FOSMC). The IOSMC is then classified based on the order and combination with other techniques, which include terminal SMC, high-order SMC, and composite SMC. The same classification is then applied to FOSMC variants. The mathematical proof, including the proposed errors, surfaces, control law, and compositions for all of the variants, is thoroughly provided. This

study concludes that the SMC and its improved variants can perform satisfactorily under parametric and uncertain scenarios. The simple SMC suffers from an inherent chattering problem, which can be mitigated by the high-order and fractional-order control schemes discussed in this study. A tabulated investigation presents the techniques proposed in the literature with the error, surfaces, WECS type, inverter type, and their findings. This will help the researcher in finding appropriate surfaces and control types according to their problem. Finally, a numerical and mathematical comparison of IOSMC and FOSMC techniques was carried out to validate the effectiveness of FOSMC techniques in WECS. The results and discussion declare that the inherent problem of chattering in SMC can be overcome by using fractional-order techniques. Moreover, the results also declare that the composite SMC improved the performance of the IOSMC and FOSMC scheme. The future directions and challenges in the field of SMC for WECS can be summarized as follows:

The main problem in sliding mode control is the chattering phenomenon. The WECS is a highly complex system that can be adversely affected by the compromise between the steady state error and level of chattering. HOSMC, adaptive systems, and continuous SMC can be further enhanced to cope with this problem. The discretization of SMC schemes for digital implementation is also a challenging problem, as the active features of SMC, which includes robustness, ideal motion, and stability, are valid in the continuous domain. The fractional-order control schemes show a good performance but the high computational complexity as validated in Figure 18 is a highlighted problem. The exact approximation of fractional-order operators needs investigation in order to further minimize the IOSMC problems. The introduction of fuzzy control theory and neural networks to the SMC schemes can improve the performance of SMC in terms of chattering reduction and robustness. The lack of robustness in high-order SMC can also be improved using artificial neural networks [221] and fuzzy logic control theory.

Author Contributions: Conceptualization, I.S.; methodology, I.S.; software, I.S.; validation, S.U.; resources, funding, supervision, J.-S.R.; review, A.A.D.; writing, review, L.K.; Writing—original draft preparation, I.S. All authors have read and agreed to the published version of the manuscript.

Funding: This work was supported by the National Research Foundation of Korea (NRF) grant funded by the Korea government (MSIT) (No. NRF-2022R1A2C2004874). This work was supported by the Human Resources Development (No.20204030200090) of the Korea Institute of Energy Technology Evaluation and Planning (KETEP) grant funded by the Korea government Ministry of Trade, Industry and Energy. This work was supported by the Korea Institute of Energy Technology Evaluation and Planning (KETEP) and the Ministry of Trade, Industry & Energy (MOTIE) of the Republic of Korea (No. 20214000000280).

Institutional Review Board Statement: Not applicable.

Informed Consent Statement: Not applicable.

Data Availability Statement: Not applicable.

Conflicts of Interest: The authors declare no conflict of interest.

References

1. IEA. *World Energy Balances*; OECD Publishing: Paris, France, 2018. Available online: https://www.oecd-ilibrary.org/energy/world-energy-balances-2018_world_energy_bal-2018-en (accessed on 15 January 2022).
2. Sami, I.; Ullah, S.; Ullah, N.; Ro, J.-S.J. Sensorless fractional order composite sliding mode control design for wind generation system. *Isa Trans.* **2021**, *111*, 275–289. [[CrossRef](#)] [[PubMed](#)]
3. Nazir, M.S.; Ali, N.; Bilal, M.; Iqbal, H.M.J. Potential environmental impacts of wind energy development: A global perspective. *Curr. Opin. Environ. Sci. Health* **2020**, *13*, 85–90. [[CrossRef](#)]
4. Sonderegger, R.C.; Henderson, D.; Bubb, S.; Steury, J.J. Distributed asset insight. *IEEE Power Energy Mag.* **2004**, *2*, 32–39. [[CrossRef](#)]
5. Puttgen, H.B.; Macgregor, P.R.; Lambert, F.C.J. Distributed generation: Semantic hype or the dawn of a new era? *IEEE Power Energy Mag.* **2003**, *1*, 22–29. [[CrossRef](#)]
6. Rahman, S.J. Green power: What is it and where can we find it?. *IEEE Power Energy Mag.* **2003**, *1*, 30–37. [[CrossRef](#)]
7. Martin, G.J. Renewable energy gets the “green” light in Chicago. *IEEE Power Energy Mag.* **2003**, *1*, 34–39. [[CrossRef](#)]

8. Kumar, D.; Chatterjee, K.J. A review of conventional and advanced MPPT algorithms for wind energy systems. *Renew. Sustain. Energy Rev.* **2016**, *55*, 957–970. [[CrossRef](#)]
9. Fernando, D.B.; Hernán, d.B.; Ricardo, J.M. *Wind Turbine Control Systems: Principles, Modelling and Gain Scheduling Design*; advances in industrial control; Springer: London, UK, 2006.
10. Xu, F.; Zhang, J.; Cheng, M. Analysis of double objectives control for wind power generation system with frequency separation. In Proceedings of the 2011 4th International Conference on Electric Utility Deregulation and Restructuring and Power Technologies (DRPT), Weihai, China, 6–9 July 2011; pp. 1366–1371.
11. Abad, G.; Lopez, J.; Rodriguez, M.; Marroyo, L.; Iwanski, G.; *Doubly Fed Induction Machine: Modeling and Control for Wind Energy Generation*; John Wiley & Sons: New York, NY, USA, 2011.
12. Baroudi, J.A.; Dinavahi, V.; Knight, A.M. A review of power converter topologies for wind generators. *Renew. Energy* **2007**, *32*, 2369–2385. [[CrossRef](#)]
13. Iglesias, R.L.; Arantegui, R.L.; Alonso, M.A.J. Power electronics evolution in wind turbines—A market-based analysis. *Renew. Sustain. Energy Rev.* **2011**, *15*, 4982–4993. [[CrossRef](#)]
14. Chakraborty, A. Advancements in power electronics and drives in interface with growing renewable energy resources. *Renew. Sustain. Energy Rev.* **2011**, *15*, 1816–1827. [[CrossRef](#)]
15. Boldea, I. *Wound Rotor Induction Generators (Wrigs). Variable Speed Generators*. Politehnica University of Timisoara; CRC Press: Boca Raton, FL, USA, 2015; pp. 1–36.
16. Li, H.; Chen, Z.J. Overview of different wind generator systems and their comparisons. *IET Renew. Power Gener.* **2008**, *2*, 123–138. [[CrossRef](#)]
17. Bellarmine, G.T.; Urquhart, J. Wind energy for the 1990s and beyond. *Energy Convers. Manag.* **1996**, *37*, 1741–1752. [[CrossRef](#)]
18. Sule, A.H.; Mokhtar, A.S.B.; Jamian, J.J.B. Optimal PI Pitch Control of SCIG Wind Turbine Using Grey Wolf Optimizer for Dynamic Stability. *Nov. Perspect. Eng. Res.* **2022**, *7*, 45–68.
19. Zribi, M.; Alrifai, M.; Rayan, M.J. Sliding mode control of a variable-speed wind energy conversion system using a squirrel cage induction generator. *Energies* **2017**, *10*, 604. [[CrossRef](#)]
20. Naik, K.; Gupta, C. Fuzzy logic based pitch angle controller/or SCIG based wind energy system. In Proceedings of the 2017 Recent Developments in Control, Automation & Power Engineering (RDCAPE), Noida, India, 26–27 October 2017; pp. 60–65.
21. Parida, A.; Chatterjee, D.J. Integrated DFIG–SCIG-based wind energy conversion system equipped with improved power generation capability. *IET Gener. Transm. Distrib.* **2017**, *11*, 3791–3800. [[CrossRef](#)]
22. Torrey, D.A. Variable-reluctance generators in wind-energy systems. In Proceedings of IEEE Power Electronics Specialist Conference-PESC’93, Seattle, WA, USA, 20–24 June 1993; pp. 561–567.
23. Arifin, A.; Al-Bahadly, I. Switched reluctance generator for variable speed wind energy applications. *Smart Grid Renew. Energy* **2011**, *2*, 27. [[CrossRef](#)]
24. Xia, Y.; Ahmed, K.H.; Williams, B.W.J. A new maximum power point tracking technique for permanent magnet synchronous generator based wind energy conversion system. *IEEE Trans. Power Electron.* **2011**, *26*, 3609–3620. [[CrossRef](#)]
25. Rolan, A.; Luna, A.; Vazquez, G.; Aguilar, D.; Azevedo, G. Modeling of a variable speed wind turbine with a permanent magnet synchronous generator. In Proceedings of the 2009 IEEE International Symposium on Industrial Electronics, Seoul, Korea, 5–8 July 2009; pp. 734–739.
26. Levy, D.J. Stand alone induction generators. *Electr. Power Syst. Res.* **1997**, *41*, 191–201. [[CrossRef](#)]
27. Blaabjerg, F.; Ma, K. Future on power electronics for wind turbine systems. *IEEE J. Emerg. Sel. Top. Power Electron.* **2013**, *1*, 139–152. [[CrossRef](#)]
28. Hatziadoniu, C.; Nikolov, E.; Pourboghrat, F.J. Power conditioner control and protection for distributed generators and storage. *IEEE Trans. Power Syst.* **2003**, *18*, 83–90. [[CrossRef](#)]
29. Santelo, T.N.; de Oliveira, C.M.R.; Maciel, C.D.; de A Monteiro, J.R.B. Wind Turbine Failures Review and Trends. *J. Control. Autom. Electr. Syst.* **2022**, *33*, 505–521. [[CrossRef](#)]
30. Hansen, A.D.; Iov, F.; Blaabjerg, F.; Hansen, L.H.J. Review of contemporary wind turbine concepts and their market penetration. *Wind. Eng.* **2004**, *28*, 247–263. [[CrossRef](#)]
31. Chinchilla, M.; Arnaltes, S.; Burgos, J.C. Control of permanent-magnet generators applied to variable-speed wind-energy systems connected to the grid. *IEEE Trans. Energy Convers.* **2006**, *21*, 130–135. [[CrossRef](#)]
32. Yamamura, N.; Ishida, M.; Hori, T. A simple wind power generating system with permanent magnet type synchronous generator. In Proceedings of the IEEE 1999 International Conference on Power Electronics and Drive Systems. PEDS’99 (Cat. No. 99TH8475), Hong Kong, China, 27–29 July 1999; Volume 2, pp. 849–854.
33. Muller, S.; Deicke, M.; Doncker, R.W.J.D. Doubly fed induction generator systems for wind turbines. *IEEE Ind. Appl. Mag.* **2002**, *8*, 26–33. [[CrossRef](#)]
34. Santos-Martin, D.; Rodriguez-Amenedo, J.L.; Arnaltes, S.J. Providing ride-through capability to a doubly fed induction generator under unbalanced voltage dips. *IEEE Trans. Power Electron.* **2009**, *24*, 1747–1757. [[CrossRef](#)]
35. Blaabjerg, F.; Chen, Z.; Kjaer, S.B. Power electronics as efficient interface in dispersed power generation systems. *IEEE Trans. Power Electron.* **2004**, *19*, no. 5, pp. 1184–1194. [[CrossRef](#)]

36. Sami, I.; Ullah, N.; Muyeen, S.; Techato, K.; Chowdhury, M.S.; Ro, J.-S.J. Control methods for standalone and grid connected micro-hydro power plants with synthetic inertia frequency support: A comprehensive review. *IEEE Access* **2020**, *8*, 176313–176329. [[CrossRef](#)]
37. Islam, M.R.; Guo, Y.; Zhu, J.J. A review of offshore wind turbine nacelle: Technical challenges, and research and developmental trends. *Renew. Sustain. Energy Rev.* **2014**, *33*, 161–176. [[CrossRef](#)]
38. Zhu, Z.; Hu, J.J. Electrical machines and power-electronic systems for high-power wind energy generation applications: Part II—power electronics and control systems. *Comput. Int. J. Comput. Math. Electr. Electron. Eng.* **2013**, *32*. [[CrossRef](#)]
39. Melício, R.; Mendes, V.; Catalão, J.P.d.S.J. Fractional-order control and simulation of wind energy systems with PMSG/full-power converter topology. *Energy Convers. Manag.* **2010**, *51*, 1250–1258. [[CrossRef](#)]
40. Sloomweg, J.; Haan, S.D.; Polinder, H.; Kling, W.J. General model for representing variable speed wind turbines in power system dynamics simulations. *IEEE Trans. Power Syst.* **2010**, *18*, 144–151. [[CrossRef](#)]
41. Chen, Z.; Spooner, E. Grid power quality with variable speed wind turbines. *IEEE Trans. Energy Convers.* **2001**, *16*, 148–154. [[CrossRef](#)]
42. Yazdani, A.; Iravani, R.J. A neutral-point clamped converter system for direct-drive variable-speed wind power unit. *IEEE Trans. Energy Convers.* **2006**, *21*, 596–607. [[CrossRef](#)]
43. Carrasco, J.M.; Franquelo, L.G.; Bialasiewicz, J.T.; Galván, E.; PortilloGuisado, R.C.; Prats, M.M.; Moreno-Alfonso, N. Power-electronic systems for the grid integration of renewable energy sources: A survey. *IEEE Trans. Ind. Electron.* **2006**, *53*, 1002–1016. [[CrossRef](#)]
44. Chen, Z.; Guerrero, J.M.; Blaabjerg, F. A review of the state of the art of power electronics for wind turbines. *IEEE Trans. Power Electron.* **2009**, *24*, 1859–1875. [[CrossRef](#)]
45. Amei, K.; Takayasu, Y.; Ohji, T.; Sakui, M. A maximum power control of wind generator system using a permanent magnet synchronous generator and a boost chopper circuit. In Proceedings of the Power Conversion Conference-Osaka 2002 (Cat. No. 02TH8579), Osaka, Japan, 2–5 April 2002; Volume 3, pp. 1447–1452.
46. Datta, R.; Ranganathan, V. Variable-speed wind power generation using doubly fed wound rotor induction machine—a comparison with alternative schemes. *IEEE Trans. Energy Convers.* **2002**, *17*, 414–421. [[CrossRef](#)]
47. Suzuki, T.; Okitsu, H.; Kawahito, T. Characteristics of a small wind-power system with DC generator. *IEE Proc. -Electr. Power Appl.*, **1982**, *129*, 217–220. [[CrossRef](#)]
48. Yang, G.; Li, H. Design and analysis of a newly brushless DC wind generator. In Proceedings of the 2008 World Automation Congress, Waikoloa, HI, USA, 28 September–2 October 2008; pp. 1–5.
49. Buehring, I.; Freris, L. Control policies for wind-energy conversion systems. *IET J.* **1981**, *128*, 253–261. [[CrossRef](#)]
50. Abdullah, M.A.; Yatim, A.; Tan, C.W.; Saidur, R.J. A review of maximum power point tracking algorithms for wind energy systems. *Renew. Sustain. Energy Rev.* **2012**, *16*, 3220–3227. [[CrossRef](#)]
51. Kooning, J.D.D.; Gevaert, L.; de Vyver, J.V.; Vandoorn, T.L.; Vandeveld, L. Online estimation of the power coefficient versus tip-speed ratio curve of wind turbines. In Proceedings of the IECON 2013-39th Annual Conference of the IEEE Industrial Electronics Society, Vienna, Austria, 10–13 November 2013; pp. 1792–1797.
52. Knight, A.M.; Peters, G.E.J. Simple wind energy controller for an expanded operating range. *IEEE Trans. Energy Convers.* **2005**, *20*, 459–466. [[CrossRef](#)]
53. Nasiri, M.; Milimonfared, J.; Fathi, S.J. Modeling, analysis and comparison of TSR and OTC methods for MPPT and power smoothing in permanent magnet synchronous generator-based wind turbines. *Energy Convers. Manag.* **2014**, *86*, 892–900. [[CrossRef](#)]
54. Yaramasu, V.; Wu, B. *Basics of Wind Energy Conversion Systems (Wecs)*; Wiley-IEEE Press: New York, NY, USA, 2017.
55. Tan, K.; Islam, S.J. Optimum control strategies in energy conversion of PMSG wind turbine system without mechanical sensors. *IEEE Trans. Energy Convers.* **2004**, *19*, 392–399. [[CrossRef](#)]
56. Ganjefar, S.; Ghassemi, A.A.; Ahmadi, M.M.J. Improving efficiency of two-type maximum power point tracking methods of tip-speed ratio and optimum torque in wind turbine system using a quantum neural network. *Energy Convers. Manag.* **2014**, *67*, 444–453. [[CrossRef](#)]
57. Agarwal, V.; Aggarwal, R.K.; Patidar, P.; Patki, C.J. A novel scheme for rapid tracking of maximum power point in wind energy generation systems. *IEEE Trans. Energy Convers.* **2009**, *25*, 228–236. [[CrossRef](#)]
58. Yan, R.; Saha, T.K.J. A new tool to estimate maximum wind power penetration level: In perspective of frequency response adequacy. *Appl. Energy* **2015**, *154*, 209–220.
59. Wei, C.; Zhang, Z.; Qiao, W.; Qu, L.J. Reinforcement-learning-based intelligent maximum power point tracking control for wind energy conversion systems. *IEEE Trans. Ind. Electron.* **2015**, *62*, 6360–6370. [[CrossRef](#)]
60. Simoes, M.G.; Bose, B.K.; Spiegel, R.J.J. Fuzzy logic based intelligent control of a variable speed cage machine wind generation system. *IEEE Trans. Power Electron.* **1997**, *12*, 87–95. [[CrossRef](#)]
61. Hilloowala, R.M.; Sharaf, A.M. A rule-based fuzzy logic controller for a PWM inverter in a stand alone wind energy conversion scheme. In Proceedings of the Conference Record of the 1993 IEEE Industry Applications Conference Twenty-Eighth IAS Annual Meeting, Toronto, ON, Canada, 2–8 October 1993; pp. 2066–2073.

62. Chen, Z.; Gomez, S.A.; McCormick, M. A fuzzy logic controlled power electronic system for variable speed wind energy conversion systems. In Proceedings of the 8th International Conference on Power Electronics and Variable Speed Drives, London, UK, 18–19 September 2000.
63. Mohamed, A.Z.; Eskander, M.N.; Ghali, F.A.J. Fuzzy logic control based maximum power tracking of a wind energy system. *Renew. Energy* **2001**, *23*, 235–245. [[CrossRef](#)]
64. Kumar, G.B. Optimal power point tracking of solar and wind energy in a hybrid wind solar energy system. *Int. J. Energy Environ. Eng.* **2022**, *13*, 77–103. [[CrossRef](#)]
65. Morimoto, S.; Nakayama, H.; Sanada, M.; Takeda, Y.J. Sensorless output maximization control for variable-speed wind generation system using IPMSG. *IEEE Trans. Ind. Appl.* **2005**, *41*, 60–67. [[CrossRef](#)]
66. Hui, J.; Bakhshai, A.; Jain, P.K. An adaptive approximation method for maximum power point tracking (MPPT) in wind energy systems. In Proceedings of the 2011 IEEE Energy Conversion Congress and Exposition, Phoenix, AZ, USA, 17–22 September 2011; pp. 2664–2669.
67. Yessef, M.; Bossoufi, B.; Taoussi, M.; Lagrioui, A.; Chojaa, H. Overview of control strategies for wind turbines: ANNC, FLC, SMC, BSC, and PI controllers. *Wind Energy* **2022**. [[CrossRef](#)]
68. Noussi, K.; Abouloifa, A.; Katir, H.; Lachkar, I.; Aouadi, C.; Aourir, M.; Otmani, F.E. Integral Backstepping Control Based on High Gain Observer for DFIG-Based Wind Energy Conversion System. *IFAC-PapersOnLine* **2022**, *55*, 653–658. [[CrossRef](#)]
69. Civelek, Z.; Lüty, M.; Çam, E.; Mamur, H. A new fuzzy logic proportional controller approach applied to individual pitch angle for wind turbine load mitigation. *Renew. Energy* **2017**, *111*, 708–717. [[CrossRef](#)]
70. Medjber, A.; Guessoum, A.; Belmili, H.; Mellit, A.J. New neural network and fuzzy logic controllers to monitor maximum power for wind energy conversion system. *Energy* **2016**, *106*, 137–146. [[CrossRef](#)]
71. Lin, W.-M.; Hong, C.-M.; Cheng, F.-S.J. Fuzzy neural network output maximization control for sensorless wind energy conversion system. *Energy* **2010**, *35*, 592–601. [[CrossRef](#)]
72. Pichan, M.; Rastegar, H.; Monfared, M.J. Two fuzzy-based direct power control strategies for doubly-fed induction generators in wind energy conversion systems. *Energy* **2013**, *51*, 154–162. [[CrossRef](#)]
73. Yang, B.; Jiang, L.; Wang, L.; Yao, W.; Wu, Q.J. Nonlinear maximum power point tracking control and modal analysis of DFIG based wind turbine. *Int. J. Electr. Power Energy Syst.* **2016**, *74*, 429–436. [[CrossRef](#)]
74. Liu, X.; Kong, X.J. Nonlinear model predictive control for DFIG-based wind power generation. *IEEE Trans. Autom. Sci. Eng.* **2013**, *11*, 1046–1055. [[CrossRef](#)]
75. Gani, A.; Mohammadi, K.; Shamshirband, S.; Altameem, T.A.; Petković, D.J. A combined method to estimate wind speed distribution based on integrating the support vector machine with firefly algorithm. *Environ. Prog. Sustain. Energy* **2016**, *35*, 867–875. [[CrossRef](#)]
76. Chen, P.; Han, D.; Li, K.-C. Robust Adaptive Control of Maximum Power Point Tracking for Wind Power System. *IEEE Access* **2020**, *8*, 214538–214550. [[CrossRef](#)]
77. Cao, Z.; Niu, Y.; Karimi, H.R.J.I.S. Sliding mode control of automotive electronic valve system under weighted try-once-discard protocol. *Inf. Sci.* **2020**, *515*, 324–340. [[CrossRef](#)]
78. Surinkaew, T.; Ngamroo, I.J. Robust power oscillation damper design for DFIG-based wind turbine based on specified structure mixed H₂/H_∞ control. *Renew. Energy* **2014**, *66*, 15–24. [[CrossRef](#)]
79. Das, S.; Subudhi, B.J. A robust active and reactive power control scheme with multiloop disturbance rejection for a wind energy conversion system. *IEEE Trans. Sustain. Energy* **2018**, *10*, 1664–1671. [[CrossRef](#)]
80. Ghanbarpour, K.; Bayat, F.; Jalilvand, A.J. Dependable power extraction in wind turbines using model predictive fault tolerant control. *Int. J. Electr. Power Energy Syst.* **2020**, *118*, 105802. [[CrossRef](#)]
81. Kühne, P.; Pöschke, F.; Schulte, H.J. Fault estimation and fault-tolerant control of the FAST NREL 5-MW reference wind turbine using a proportional multi-integral observer. *Int. J. Adapt. Control. Process.* **2018**, *32*, 568–585. [[CrossRef](#)]
82. Aguilar, M.E.B.; Coury, D.V.; Reginatto, R.; Monaro, R.M.J. Multi-objective PSO applied to PI control of DFIG wind turbine under electrical fault conditions. *Electr. Power Syst. Res.* **2020**, *180*, 106081. [[CrossRef](#)]
83. Shaker, M.S.; Patton, R.J.J. Active sensor fault tolerant output feedback tracking control for wind turbine systems via T-S model. *Eng. Appl. Artif. Intell.* **2014**, *34*, 1–12. [[CrossRef](#)]
84. Kamal, E.; Aitouche, A.; Oueidat, M.J. Fuzzy fault-tolerant control of wind-diesel hybrid systems subject to sensor faults. *IEEE Trans. Sustain. Energy* **2013**, *4*, 857–866. [[CrossRef](#)]
85. Alqahtani, A.H.; Utkin, V.I. Self-optimization of photovoltaic system power generation based on sliding mode control. In Proceedings of the IECON 2012-38th Annual Conference on IEEE Industrial Electronics Society, Montreal, QC, Canada, 25–28 October 2012; pp. 3468–3474.
86. Levron, Y.; Shmilovitz, D.J. Maximum power point tracking employing sliding mode control. *IEEE Trans. Circuits Syst. Regul. Pap.* **2013**, *60*, 724–732. [[CrossRef](#)]
87. Costa, J.P.D.; Pinheiro, H.; Degner, T.; Arnold, G. Robust controller for DFIGs of grid-connected wind turbines. *IEEE Trans. Ind. Electron.* **2010**, *58*, 4023–4038. [[CrossRef](#)]
88. Pande, V.; Mate, U.; Kurode, S.J. Discrete sliding mode control strategy for direct real and reactive power regulation of wind driven DFIG. *Electr. Power Syst. Res.* **2013**, *100*, 73–81. [[CrossRef](#)]

89. Majout, B.; Bossoufi, B.; Bouderbala, M.; Masud, M.; Al-Amri, J.F.; Taoussi, M.; El Mahfoud, M.; Motahhir, S.; Karim, M. Improvement of PMSG-Based Wind Energy Conversion System Using Developed Sliding Mode Control. *Energies* **2022**, *15*, 1625. [[CrossRef](#)]
90. Ardjoun, S.A.E.M.; Abid, M. Fuzzy sliding mode control applied to a doubly fed induction generator for wind turbines. *Turk. J. Electr. Eng. Comput. Sci.* **2015**, *23*, 1673–1686. [[CrossRef](#)]
91. Djoudi, A.; Chekireb, H.; Bacha, S.J. Low-cost sliding mode control of WECS based on DFIG with stability analysis. *Turk. J. Electr. Eng. Comput. Sci.* **2015**, *23*, 1698–1714. [[CrossRef](#)]
92. Utkin, V.; Lee, H. Chattering problem in sliding mode control systems. In Proceedings of the VSS'06: International Workshop on Variable Structure Systems, Alghero, Italy, 5–7 June 2006, pp. 346–350.
93. Kassem, A.M.; Hasaneen, K.M.; Yousef, A.M.J. Dynamic modeling and robust power control of DFIG driven by wind turbine at infinite grid. *Int. J. Electr. Power Energy Syst.* **2013**, *44*, 375–382. [[CrossRef](#)]
94. Laghrouche, S.; Plestan, F.; Glumineau, A.J. Higher order sliding mode control based on integral sliding mode. *Automatica* **2007**, *43*, 531–537. [[CrossRef](#)]
95. ; Zholtayev, D.; Rubagotti, M.; Do, T.D. Adaptive super-twisting sliding mode control for maximum power point tracking of PMSG-based wind energy conversion systems. *Renew. Energy* **2022**, *183*, 877–889. [[CrossRef](#)]
96. Mazouz, F.; Belkacem, S.; Boukhalifa, G. Second Order Sliding Mode Control Based DPC of DFIG Using SVM. In Proceedings of the International Conference on Artificial Intelligence in Renewable Energetic Systems, Tipasa, Algeriapp, 24–26 November 2021; Springer: Cham, Switzerland, 2021; pp. 743–750.
97. Dekali, Z.; Baghli, L.; Boumediene, A. Improved Super Twisting Based High Order Direct Power Sliding Mode Control of a Connected DFIG Variable Speed Wind Turbine. *Period. Polytech. Electr. Eng. Comput. Sci.* **2021**. [[CrossRef](#)]
98. Abdeddaim, S.; Betka, A. Optimal tracking and robust power control of the DFIG wind turbine. *Int. J. Electr. Power Energy Syst.* **2013**, *49*, 234–242. [[CrossRef](#)]
99. Du, C.; Han, Y.; Li, S. A Barrier Function-Based Variable-Gain SOSM Power Control Scheme for DFIG Wind Turbine. In Proceedings of 2021 Chinese Intelligent Automation Conference, Zhanjiang, China, 5–7 November 2021; Springer: Singapore, 2022; pp. 116–123.
100. Hwang, S.; Park, J.B.; Joo, Y.H.J. Disturbance observer-based integral fuzzy sliding-mode control and its application to wind turbine system. *IET Control. Theory Appl.* **2019**, *13*, 1891–1900. [[CrossRef](#)]
101. Song, Z.; Shi, T.; Xia, C.; Chen, W.J. A novel adaptive control scheme for dynamic performance improvement of DFIG-Based wind turbines. *Energy* **2012**, *38*, 104–117. [[CrossRef](#)]
102. Ebrahimkhani, S.J. Robust fractional order sliding mode control of doubly-fed induction generator (DFIG)-based wind turbines. *ISA Trans.* **2016**, *63*, 343–354. [[CrossRef](#)] [[PubMed](#)]
103. Xiong, L.; Li, P.; Ma, M.; Wang, Z.; Wang, J.J. Output power quality enhancement of PMSG with fractional order sliding mode control. *Int. J. Electr. Power Energy Syst.* **2020**, *115*, 105402. [[CrossRef](#)]
104. Ullah, N.; Ali, M.A.; Ibeas, A.; Herrera, J.J. Adaptive fractional order terminal sliding mode control of a doubly fed induction generator-based wind energy system. *IEEE Access* **2017**, *5*, 21368–21381. [[CrossRef](#)]
105. Sami, I.; Ullah, S.; Ali, Z.; Ullah, N.; Ro, J.-S.J. A Super Twisting Fractional Order Terminal Sliding Mode Control for DFIG-Based Wind Energy Conversion System. *Energies* **2020**, *13*, 2158. [[CrossRef](#)]
106. Ullah, N.; Sami, I.; Chowdhury, M.S.; Techato, K.; Alkhamash, H.J. Artificial Intelligence Integrated Fractional Order Control of Doubly Fed Induction Generator Based Wind Energy System. *IEEE Access* **2020**, *9*, 5734–5748. [[CrossRef](#)]
107. Tamaarat, A.; Benakcha, A.J. Performance of PI controller for control of active and reactive power in DFIG operating in a grid-connected variable speed wind energy conversion system. *Front. Energy* **2014**, *8*, 371–378. [[CrossRef](#)]
108. Bossoufi, B.; Karim, M.; Lagrioui, A.; Taoussi, M.; Derouich, A.J. Observer backstepping control of DFIG-Generators for wind turbines variable-speed: FPGA-based implementation. *Renew. Energy* **2015**, *81*, 903–917. [[CrossRef](#)]
109. Taraft, S.; Rekioua, D.; Aouzellag, D.; Bacha, S.J. A proposed strategy for power optimization of a wind energy conversion system connected to the grid. *Energy Convers. Manag.* **2015**, *101*, 489–502. [[CrossRef](#)]
110. Hu, J.; Nian, H.; Hu, B.; He, Y.; Zhu, Z.J. Direct active and reactive power regulation of DFIG using sliding-mode control approach. *IEEE Trans. Energy Convers.* **2010**, *25*, 1028–1039. [[CrossRef](#)]
111. Fallaha, C.J.; Saad, M.; Kanaan, H.Y.; Al-Haddad, K.J. Sliding-mode robot control with exponential reaching law. *IEEE Trans. Ind. Electron.* **2010**, *58*, 600–610. [[CrossRef](#)]
112. Wang, J.; Bo, D.; Ma, X.; Zhang, Y.; Li, Z.; Miao, Q.J. Adaptive back-stepping control for a permanent magnet synchronous generator wind energy conversion system. *Int. J. Hydrogen Energy* **2019**, *44*, 3240–3249. [[CrossRef](#)]
113. Shihabudheen, K.; Raju, S.K.; Pillai, G.N.J. Control for grid-connected DFIG-based wind energy system using adaptive neuro-fuzzy technique. *Int. Trans. Electr. Energy Syst.* **2018**, *28*, e2526. [[CrossRef](#)]
114. Mérida, J.; Aguilar, L.T.; Dávila, J.J. Analysis and synthesis of sliding mode control for large scale variable speed wind turbine for power optimization. *Renew. Energy* **2014**, *71*, 715–728. [[CrossRef](#)]
115. Xiong, L.; Li, P.; Wu, F.; Ma, M.; Khan, M.W.; Wang, J.J. A coordinated high-order sliding mode control of DFIG wind turbine for power optimization and grid synchronization. *Int. J. Electr. Power Energy Syst.* **2019**, *105*, 679–689. [[CrossRef](#)]
116. Beltran, B.; Benbouzid, M.E.H.; Ahmed-Ali, T.J. Second-order sliding mode control of a doubly fed induction generator driven wind turbine. *IEEE Trans. Energy Convers.* **2012**, *27*, 261–269. [[CrossRef](#)]

117. Beltran, B.; Ahmed-Ali, T.; Benbouzid, M.E.H.J. High-order sliding-mode control of variable-speed wind turbines. *IEEE Trans. Ind. Electron.* **2008**, *56*, 3314–3321. [[CrossRef](#)]
118. Zhang, C.; Gutierrez, S.; Plestan, F.; de León-Morales, J.J. Adaptive super-twisting control of floating wind turbines with collective blade pitch control. *IFAC-PapersOnLine* **2019**, *52*, 117–122. [[CrossRef](#)]
119. Chen, H.; Li, Q.; Tang, S.; Nadia, A.A.; Han, J.; Wang, T.; Benbouzid, M. Adaptive super-twisting control of doubly salient permanent magnet generator for tidal stream turbine. *Int. J. Electr. Power Energy Syst.* **2021**, *128*, 106772. [[CrossRef](#)]
120. Milosavljevic, D. General conditions for existence of a quasi-sliding mode on the switching hyperplane in discrete variable structure systems. *Autom. Remote Control* **1985**, *46*, 307–314.
121. Bartoszewicz, A. Discrete-time quasi-sliding-mode control strategies. *IEEE Trans. Ind. Electron.* **1998**, *45*, 633–637. [[CrossRef](#)]
122. Ngadungon, R.B.N.; Sam, Y.B.M. Discrete time sliding mode control using multirate output feedback to reduce chattering. In Proceedings of the 2010 IEEE Student Conference on Research and Development (SCoReD), Kuala Lumpur, Malaysia, 13–14 December 2010; pp. 236–239.
123. Beltran, B.; Ahmed-Ali, T.; Benbouzid, M.E.H. Sliding mode power control of variable-speed wind energy conversion systems. *IEEE Trans. Energy Convers.* **2008**, *23*, 551–558. [[CrossRef](#)]
124. Mozayan, S.M.; Saad, M.; Vahedi, H.; Fortin-Blanchette, H.; Soltani, M.J. Sliding mode control of PMSG wind turbine based on enhanced exponential reaching law. *IEEE Trans. Ind. Electron.* **2016**, *63*, 6148–6159. [[CrossRef](#)]
125. Hung, J.Y.; Gao, W.; Hung, J.C. Variable structure control: A survey. *IEEE Trans. Ind. Electron.* **1993**, *40*, 2–22. [[CrossRef](#)]
126. Kelkoul, B.; Boumediene, A.J. Stability analysis and study between classical sliding mode control (SMC) and super twisting algorithm (STA) for doubly fed induction generator (DFIG) under wind turbine. *Energy Convers. Manag.* **2020**, *214*, 118871. [[CrossRef](#)]
127. Fridman, L.; Moreno, J.A.; Bandyopadhyay, B.; Kamal, S.; Chalanga, A. Continuous nested algorithms: The fifth generation of sliding mode controllers. In *Recent Advances in Sliding Modes: From Control to Intelligent Mechatronics*; Springer: Cham, Switzerland, 2015; pp. 5–35.
128. Bekakra, Y.; Attous, D.B. Sliding mode controls of active and reactive power of a DFIG with MPPT for variable speed wind energy conversion. *Aust. J. Basic Appl. Sci.* **2011**, *5*, 2274–2286.
129. Machmoum, M.; Poitiers, F. Sliding mode control of a variable speed wind energy conversion system with DFIG. In Proceedings of the International Conference and Exhibition on Ecologic Vehicles and Renewable Energies, Monte-Carlo, Monaco, 8–10 May 2019; pp. 26–29.
130. Liu, X.; Han, Y.; Wang, C.J. Second-order sliding mode control for power optimisation of DFIG-based variable speed wind turbine. *IET Renew. Power Gener.* **2016**, *11*, 408–418. [[CrossRef](#)]
131. Beltran, B.; Benbouzid, M.; Ahmed-Ali, T. High-order sliding mode control of a DFIG-based wind turbine for power maximization and grid fault tolerance. In Proceedings of the 2009 IEEE International Electric Machines and Drives Conference, Miami, FL, USA, 3–6 May 2009; pp. 183–189.
132. Levant, A.J. Higher-order sliding modes, differentiation and output-feedback control. *Int. J. Control* **2003**, *76*, 924–941. [[CrossRef](#)]
133. Benelghali, S.; Benbouzid, M.; Charpentier, J.; Ahmed-Ali, T.; Munteanu, I. Experimental validation of a marine current turbine simulator: Application to a PMSG-based system second-order sliding mode control. *IEEE Trans. Ind. Electron.* **2011**, *58*, 118–126. [[CrossRef](#)]
134. Elghali, S.E.B.; Benbouzid, M.E.H.; Ahmed-Ali, T.; Charpentier, J.F.J. High-order sliding mode control of a marine current turbine driven doubly-fed induction generator. *IEEE J. Ocean. Eng.* **2010**, *35*, 402–411. [[CrossRef](#)]
135. Benbouzid, M.; Beltran, B.; Amirat, Y.; Yao, G.; Han, J.; Mangel, H. Second-order sliding mode control for DFIG-based wind turbines fault ride-through capability enhancement. *ISA Trans.* **2014**, *53*, 827–833. [[CrossRef](#)] [[PubMed](#)]
136. Dursun, E.H.; Kulaksiz, A.A.J. Second-order sliding mode voltage-regulator for improving MPPT efficiency of PMSG-based WECS. *Int. J. Electr. Power Energy Syst.* **2020**, *121*, 106149. [[CrossRef](#)]
137. Wang, J.; Bo, D.; Miao, Q.; Li, Z.; Wu, X.; Lv, D.J. Maximum power point tracking control for a doubly fed induction generator wind energy conversion system based on multivariable adaptive super-twisting approach. *Int. J. Electr. Power Energy Syst.* **2021**, *124*, 106347. [[CrossRef](#)]
138. Valenciaga, F.; Puleston, P.J. High-order sliding control for a wind energy conversion system based on a permanent magnet synchronous generator. *IEEE Trans. Energy Convers.* **2008**, *23*, 860–867. [[CrossRef](#)]
139. Evangelista, C.; Puleston, P.; Valenciaga, F.; Fridman, L.M.J. Lyapunov-designed super-twisting sliding mode control for wind energy conversion optimization. *IEEE Trans. Ind. Electron.* **2012**, *60*, 538–545. [[CrossRef](#)]
140. Evangelista, C.; Valenciaga, F.; Puleston, P.J. Active and reactive power control for wind turbine based on a MIMO 2-sliding mode algorithm with variable gains. *IEEE Trans. Energy Convers.* **2013**, *28*, 682–689. [[CrossRef](#)]
141. Merabet, A.; Ahmed, K.T.; Ibrahim, H.; Beguenane, R.J. Implementation of sliding mode control system for generator and grid sides control of wind energy conversion system. *IEEE Trans. Sustain. Energy* **2016**, *7*, 1327–1335. [[CrossRef](#)]
142. Morshed, M.J.; Fekih, A.J. A new fault ride-through control for DFIG-based wind energy systems. *Electr. Power Syst. Res.* **2017**, *146*, 258–269. [[CrossRef](#)]
143. Evangelista, C.A.; Pisano, A.; Puleston, P.; Usai, E.J. Receding horizon adaptive second-order sliding mode control for doubly-fed induction generator based wind turbine. *IEEE Trans. Control. Syst. Technol.* **2016**, *25*, 73–84. [[CrossRef](#)]

144. Benamor, A.; Benchouia, M.; Srairi, K.; Benbouzid, M. A novel rooted tree optimization apply in the high order sliding mode control using super-twisting algorithm based on DTC scheme for DFIG. *Int. J. Electr. Power Energy Syst.* **2019**, *108*, 293–302. [[CrossRef](#)]
145. Berrada, Y.; Boumhidi, I. New structure of sliding mode control for variable speed wind turbine. *IFAC J. Syst. Control* **2020**, *14*, 100113. [[CrossRef](#)]
146. Karabacak, M.J. A new perturb and observe based higher order sliding mode MPPT control of wind turbines eliminating the rotor inertial effect. *Renew. Energy* **2019**, *133*, 807–827. [[CrossRef](#)]
147. Xiong, L.; Li, P.; Wang, J.J. High-order sliding mode control of DFIG under unbalanced grid voltage conditions. *Int. J. Electr. Power Energy Syst.* **2020**, *117*, 105608. [[CrossRef](#)]
148. Shtessel, Y.; Taleb, M.; Plestan, F.J. A novel adaptive-gain supertwisting sliding mode controller: Methodology and application. *Automatica* **2012**, *48*, 759–769. [[CrossRef](#)]
149. Utkin, V.; Shi, J. Integral sliding mode in systems operating under uncertainty conditions. In Proceedings of the 35th IEEE Conference on Decision and Control, Kobe, Japan, 13 December 1996; Volume 4, pp. 4591–4596.
150. Suleimenov, K.; Sarsembayev, B.; Phuc, B.D.H.; Do, T.D.J. Disturbance observer-based integral sliding mode control for wind energy conversion systems. *Wind. Energy* **2020**, *23*, 1026–1047. [[CrossRef](#)]
151. Saravanakumar, R.; Jena, D.J. Validation of an integral sliding mode control for optimal control of a three blade variable speed variable pitch wind turbine. *Int. J. Electr. Power Energy Syst.* **2015**, *69*, 421–429. [[CrossRef](#)]
152. Li, S.; Wang, H.; Tian, Y.; Aitouch, A.; Klein, J.J. Direct power control of DFIG wind turbine systems based on an intelligent proportional-integral sliding mode control. *ISA Trans.* **2016**, *64*, 431–439. [[CrossRef](#)]
153. Chen, S.Z.; Cheung, N.C.; Wong, K.C.; Wu, J. Integral sliding-mode direct torque control of doubly-fed induction generators under unbalanced grid voltage. *IEEE Trans. Energy Convers.* **2009**, *25*, 356–368. [[CrossRef](#)]
154. Martinez, M.I.; Susperregui, A.; Tapia, G.; Camblong, H.J. Sliding-Mode Control for a DFIG-based Wind Turbine under Unbalanced Voltage. *Ifac Proc. Vol.* **2011**, *44*, 538–543. [[CrossRef](#)]
155. Liu, Y.; Wang, Z.; Xiong, L.; Wang, J.; Jiang, X.; Bai, G.; Liu, S. DFIG wind turbine sliding mode control with exponential reaching law under variable wind speed. *Int. J. Electr. Power Energy Syst.* **2018**, *96*, 253–260. [[CrossRef](#)]
156. Errouissi, R.; Al-Durra, A.J. A novel PI-type sliding surface for PMSG-based wind turbine with improved transient performance. *IEEE Trans. Energy Convers.* **2017**, *33*, 834–844. [[CrossRef](#)]
157. Sarsembayev, B.; Suleimenov, K.; Mirzagalikova, B.; Do, T.D.J. SDRE-based integral sliding mode control for wind energy conversion systems. *IEEE Access* **2020**, *8*, 51100–51113. [[CrossRef](#)]
158. Nayeh, R.F.; Moradi, H.; Vossoughi, G.J. Multivariable robust control of a horizontal wind turbine under various operating modes and uncertainties: A comparison on sliding mode and H_∞ control. *Int. J. Electr. Power Energy Syst.* **2020**, *115*, 105474. [[CrossRef](#)]
159. Yin, X.; Jiang, Z.; Pan, L.J. Recurrent neural network based adaptive integral sliding mode power maximization control for wind power systems. *Renew. Energy* **2020**, *145*, 1149–1157. [[CrossRef](#)]
160. Dali, A.; Abdelmalek, S.; Bakdi, A.; Bettayeb, M. A new robust control scheme: Application for MPP tracking of a PMSG-based variable-speed wind turbine. *Renew. Energy* **2021**, *172*, 1021–1034. [[CrossRef](#)]
161. Xiong, L.; Li, J.; Li, P.; Huang, S.; Wang, Z.; Wang, J.J. Event triggered prescribed time convergence sliding mode control of DFIG with disturbance rejection capability. *Int. J. Electr. Power Energy Syst.* **2021**, *131*, 106970. [[CrossRef](#)]
162. Yu, X.; Kaynak, O.J. Sliding-mode control with soft computing: A survey. *IEEE Trans. Ind. Electron.* **2009**, *56*, 3275–3285.
163. Utkin, V.; Poznyak, A.; Orlov, Y.; Polyakov, A.J. Conventional and high order sliding mode control. *J. Frankl. Inst.* **2020**, *357*, 10244–10261. [[CrossRef](#)]
164. Yu, X.; Feng, Y.; Man, Z.J. Terminal Sliding Mode Control-An Overview. *IEEE Open J. Ind. Electron. Soc.* **2020**, *2*, 36–52. [[CrossRef](#)]
165. Zak, M.J. Terminal attractors for addressable memory in neural networks. *Phys. Lett. A* **1988**, *133*, 18–22. [[CrossRef](#)]
166. Venkataraman, S.; Gulati, S. Control of nonlinear systems using terminal sliding modes. *J. Dyn. Sys. Meas. Control.* **1993**, *115*, 554–560. [[CrossRef](#)]
167. Yu, X.; Man, Z.J. Model reference adaptive control systems with terminal sliding modes. *Int. J. Control* **1996**, *64*, 1165–1176. [[CrossRef](#)]
168. Zhihong, M.; Paplinski, A.P.; Wu, H.R.J. A robust MIMO terminal sliding mode control scheme for rigid robotic manipulators. *IEEE Trans. Autom. Control* **1994**, *39*, 2464–2469. [[CrossRef](#)]
169. Zhihong, M.; Yu, X.H.J. Terminal sliding mode control of MIMO linear systems. *IEEE Trans. Circuits Syst. Fundam. Theory Appl.* **1997**, *44*, 1065–1070. [[CrossRef](#)]
170. Feng, Y.; Yu, X.; Man, Z.J. Non-singular terminal sliding mode control of rigid manipulators. *Automatica* **2002**, *38*, 2159–2167. [[CrossRef](#)]
171. Yu, X.; Zhihong, M.J. Fast terminal sliding-mode control design for nonlinear dynamical systems. *IEEE Trans. Circuits Syst. Fundam. Theory Appl.* **2002**, *49*, 261–264.
172. Yu, S.; Yu, X.; Shirinzadeh, B.; Man, Z.J. Continuous finite-time control for robotic manipulators with terminal sliding mode. *Automatica* **2005**, *41*, 1957–1964. [[CrossRef](#)]
173. Patnaik, R.; Dash, P.J. Fast adaptive finite-time terminal sliding mode power control for the rotor side converter of the DFIG based wind energy conversion system. *Sustain. Energy, Grids Netw.* **2015**, *1*, 63–84. [[CrossRef](#)]

174. Patnaik, R.; Dash, P.; Mahapatra, K.J. Adaptive terminal sliding mode power control of DFIG based wind energy conversion system for stability enhancement. *Int. Trans. Electr. Energy Syst.* **2016**, *26*, 750–782. [[CrossRef](#)]
175. Yazıcı, İ.; Yaylacı, E.K.J. Discrete-time integral terminal sliding mode based maximum power point controller for the PMSG-based wind energy system. *Iet Power Electron.* **2019**, *12*, 3688–3696. [[CrossRef](#)]
176. Zheng, X.; Feng, Y.; Han, F.; Yu, X.J. Integral-type terminal sliding-mode control for grid-side converter in wind energy conversion systems. *IEEE Trans. Ind. Electron.* **2018**, *66*, 3702–3711. [[CrossRef](#)]
177. Morshed, M.J.; Fekih, A.J. Design of a chattering-free integral terminal sliding mode approach for DFIG-based wind energy systems. *Optim. Control. Appl. Methods* **2020**, *41*, 1718–1734. [[CrossRef](#)]
178. Balamurugan, S.; Venkatesh, P.; Varatharajan, M. Fuzzy sliding-mode control with low pass filter to reduce chattering effect: An experimental validation on Quanser SRIP. *Sādhanā* **2017**, *42*, 1693–1703. [[CrossRef](#)]
179. Xu, N.; Chen, Y.; Xue, A.; Zong, G.; Zhao, X.J. Event-trigger-based adaptive fuzzy hierarchical sliding mode control of uncertain under-actuated switched nonlinear systems. *ISA Trans.* **2019**, *124*, 301–310. [[CrossRef](#)]
180. Yin, X.-x.; Lin, Y.-g.; Li, W.; Gu, Y.-j.; Lei, P.-f.; Liu, H.-w.J. Sliding mode voltage control strategy for capturing maximum wind energy based on fuzzy logic control. *Int. J. Electr. Power Energy Syst.* **2015**, *70*, 45–51. [[CrossRef](#)]
181. Yin, X.-X.; Lin, Y.-G.; Li, W.; Liu, H.-W.; Gu, Y.-J.J. Fuzzy-logic sliding-mode control strategy for extracting maximum wind power. *IEEE Trans. Energy Convers.* **2015**, *30*, 1267–1278. [[CrossRef](#)]
182. Do, T.D.J. Disturbance observer-based fuzzy SMC of WECSs without wind speed measurement. *IEEE Access* **2016**, *5*, 147–155. [[CrossRef](#)]
183. Bounar, N.; Labdai, S.; Boukroune, A. PSO–GSA based fuzzy sliding mode controller for DFIG-based wind turbine. *ISA Trans.* **2019**, *85*, 177–188. [[CrossRef](#)]
184. Hong, C.-M.; Huang, C.-H.; Cheng, F.-S.J. Sliding mode control for variable-speed wind turbine generation systems using artificial neural network. *Energy Procedia* **2014**, *61*, 1626–1629. [[CrossRef](#)]
185. Miller, K.S.; Ross, B. *An Introduction to the Fractional Calculus and Fractional Differential Equations*; Wiley: Hoboken, NJ, USA, 1993.
186. Srivastava, H.J. Fractional Differential Equations. I Podlubny. *Appl. Mech. Rev.* **2000**, *53*, B51.
187. Matignon, D. Stability properties for generalized fractional differential systems. In *ESAIM: Proceedings*; EDP Sciences: Paris, France, 1998; Volume 5, pp. 145–158.
188. Zhang, Q.; Zhuang, X.; Liu, Y.; Wang, C.; Guo, H.J. A novel control strategy for mode seamless switching of PV converter in DC microgrid based on double integral sliding mode control. *ISA Trans.* **2020**, *100*, 469–480. [[CrossRef](#)] [[PubMed](#)]
189. Incremona, G.P.; Rubagotti, M.; Ferrara, A.J. Sliding mode control of constrained nonlinear systems. *IEEE Trans. Autom. Control.* **2016**, *62*, 2965–2972. [[CrossRef](#)]
190. Liu, C.; Sun, W.; Zhang, J.J. Adaptive sliding mode control for 4-wheel SBW system with Ackerman geometry. *ISA Trans.* **2020**, *96*, 103–115. [[CrossRef](#)]
191. Chen, L.; Wang, H.; Huang, Y.; Ping, Z.; Yu, M.; Zheng, X.; Hu, Y. Robust hierarchical sliding mode control of a two-wheeled self-balancing vehicle using perturbation estimation. *Mech. Syst. Process.* **2020**, *139*, 106584. [[CrossRef](#)]
192. Kang, S.; Yan, H.; Dong, L.; Li, C.J. Finite-time adaptive sliding mode force control for electro-hydraulic load simulator based on improved GMS friction model. *Mech. Syst. Process.* **2018**, *102*, 117–138. [[CrossRef](#)]
193. Pradhan, S.; Singh, B.; Panigrahi, B.K.; Murshid, S.J. A composite sliding mode controller for wind power extraction in remotely located solar PV–wind hybrid system. *IEEE Trans. Ind. Electron.* **2018**, *66*, 5321–5331. [[CrossRef](#)]
194. Yashar, M.; Bevan, G.; Kucukdemiral, I.B.; Fekih, A. Sliding mode control of wind energy conversion systems: Trends and applications. *Renew. Sustain. Energy Rev.* **2022**, *167*, 112734.
195. Wang, H.; Shi, L.; Man, Z.; Zheng, J.; Li, S.; Yu, M.; Cao, Z. Continuous fast nonsingular terminal sliding mode control of automotive electronic throttle systems using finite-time exact observer. *IEEE Trans. Ind. Electron.* **2018**, *65*, 7160–7172. [[CrossRef](#)]
196. Yao, X.; Park, J.H.; Dong, H.; Guo, L.; Lin, X.J. Robust adaptive nonsingular terminal sliding mode control for automatic train operation. *IEEE Trans. Syst. Man Cybern. Syst.* **2018**, *49*, 2406–2415. [[CrossRef](#)]
197. Farid, Y.; Majd, V.J.; Ehsani-Seresht, A.J. Fractional-order active fault-tolerant force-position controller design for the legged robots using saturated actuator with unknown bias and gain degradation. *Mech. Syst. Process.* **2018**, *104*, 465–486. [[CrossRef](#)]
198. Mousavi, Y.; Alfi, A.J. A memetic algorithm applied to trajectory control by tuning of fractional order proportional-integral-derivative controllers. *Appl. Soft Comput.* **2015**, *36*, 599–617. [[CrossRef](#)]
199. Wei, Y.-Q.; Liu, D.-Y.; Boutat, D.J. Innovative fractional derivative estimation of the pseudo-state for a class of fractional order linear systems. *Automatica* **2019**, *99*, 157–166. [[CrossRef](#)]
200. Mousavi, Y.; Alfi, A.J. Fractional calculus-based firefly algorithm applied to parameter estimation of chaotic systems. *Chaos Solitons Fractals* **2018**, *114*, 202–215. [[CrossRef](#)]
201. Sun, G.; Ma, Z.; Yu, J.J. Discrete-time fractional order terminal sliding mode tracking control for linear motor. *IEEE Trans. Ind. Electron.* **2017**, *65*, 3386–3394. [[CrossRef](#)]
202. Wang, Y.; Chen, J.; Yan, F.; Zhu, K.; Chen, B.J. Adaptive super-twisting fractional-order nonsingular terminal sliding mode control of cable-driven manipulators. *ISA Trans.* **2019**, *86*, 163–180. [[CrossRef](#)] [[PubMed](#)]
203. Sun, G.; Ma, Z.J. Practical tracking control of linear motor with adaptive fractional order terminal sliding mode control. *IEEE/ASME Trans. Mechatronics* **2017**, *22*, 2643–2653. [[CrossRef](#)]

204. Yashar, M.; Zarei, A.; Jahromi, Z.S. Robust adaptive fractional-order nonsingular terminal sliding mode stabilization of three-axis gimbal platforms. *ISA Trans.* **2022**, *123*, 98–109.
205. Delghavi, M.B.; Shoja-Majidabad, S.; Yazdani, A. Fractional-order sliding-mode control of islanded distributed energy resource systems. *IEEE Trans. Sustain. Energy* **2016**, *7*, 1482–1491. [[CrossRef](#)]
206. Aghababa, M.P. A Lyapunov-based control scheme for robust stabilization of fractional chaotic systems. *Nonlinear Dyn.* **2014**, *78*, 2129–2140. [[CrossRef](#)]
207. Li, C.; Deng, W.J. Remarks on fractional derivatives. *Appl. Math. Comput.* **2007**, *187*, 777–784. [[CrossRef](#)]
208. Zhang, F.; Li, C.J. Stability analysis of fractional differential systems with order lying in (1, 2). *Adv. Differ. Equ.* **2011**, *2011*, 1–17. [[CrossRef](#)] [[PubMed](#)]
209. Gao, Z.; Liao, X.J. Improved Oustaloup approximation of fractional-order operators using adaptive chaotic particle swarm optimization. *J. Syst. Eng. Electron.* **2012**, *23*, 145–153. [[CrossRef](#)]
210. Burton, T.; Sharpe, D.; Jenkins, N.; Bossanyi, E. *Wind Energy Handbook*; Wiley Online Library: Hoboken, NJ, USA, 2001.
211. Kiruthiga, B.J. Implementation of first order sliding mode control of active and reactive power for DFIG based wind turbine. *Int. J. Inf. Futur. Res.* **2015**, *2*, 2487–2497.
212. Lima, F.; Watanabe, E.H.; Rodriguez, P.; Luna, A. A simplified model for wind turbine based on doubly fed induction generator. In Proceedings of the 2011 International Conference on Electrical Machines and Systems, Beijing, China, 20–23 August 2011; pp. 1–6.
213. Mechter, A.; Kemih, K.; Ghanes, M.J. Sliding mode control of a wind turbine with exponential reaching law. *Acta Polytech. Hung.* **2015**, *12*, 167–183.
214. Patton, R.J.; Frank, P.M.; Clark, R.N. *Issues of Fault Diagnosis for Dynamic Systems*; Springer Science & Business Media: Berlin, Germany, 2013.
215. Huerta, H.; Loukianov, A.J. Energy based sliding mode control of Brushless Double-fed Induction Generator. *Int. J. Electr. Power Energy Syst.* **2021**, *130*, 107002. [[CrossRef](#)]
216. Yang, B.; Yu, T.; Shu, H.; Zhang, Y.; Chen, J.; Sang, Y.; Jiang, L. Passivity-based sliding-mode control design for optimal power extraction of a PMSG based variable speed wind turbine. *Renew. Energy* **2018**, *119*, 577–589. [[CrossRef](#)]
217. Djilali, L.; Caballero-Barragán, H.; Osuna-Ibarra, L.; Sanchez, E.N.; Loukianov, A.J. Neural Sliding Mode Control of a DFIG Based Wind Turbine with Measurement Delay. *IFAC-PapersOnLine* **2018**, *51*, 456–461. [[CrossRef](#)]
218. Xiong, L.; Wang, J.; Mi, X.; Khan, M.W.J. Fractional order sliding mode based direct power control of grid-connected DFIG. *IEEE Trans. Power Syst.* **2017**, *33*, 3087–3096. [[CrossRef](#)]
219. Dong, H.; Su, M.; Liu, K.; Zou, W.J. Mitigation Strategy of Subsynchronous Oscillation Based on Fractional-Order Sliding Mode Control for VSC-MTDC Systems With DFIG-Based Wind Farm Access. *IEEE Access* **2020**, *8*, 209242–209250. [[CrossRef](#)]
220. Zhang, B.; Pi, Y.; Luo, Y.J. Fractional order sliding-mode control based on parameters auto-tuning for velocity control of permanent magnet synchronous motor. *ISA Trans.* **2012**, *51*, 649–656. [[CrossRef](#)]
221. Amin, U.S.; Ullah, M.; Sajjad, M.; Cheikh, F.A.; Hijji, M.; Hijji, A.; Muhammad, K. EADN: An Efficient Deep Learning Model for Anomaly Detection in Videos. *Mathematics* **2022**, *10*, 1555. [[CrossRef](#)]